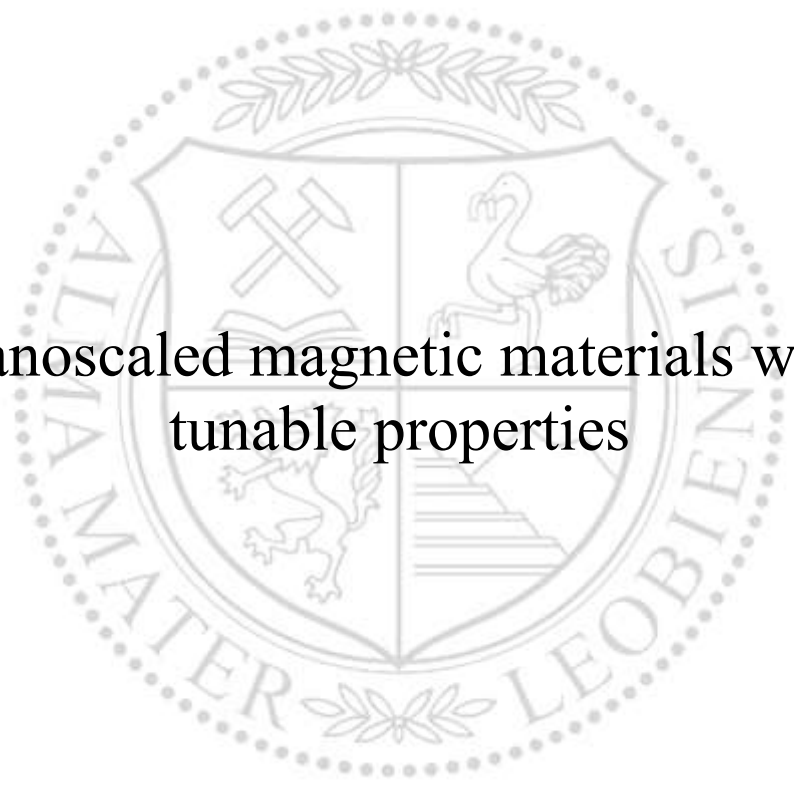




Chair of Materials Physics

Doctoral Thesis



Nanoscaled magnetic materials with
tunable properties

Dipl.-Ing. Martin Stückler, BSc

November 2020

This doctoral thesis was written at the Erich Schmid Institute for Materials Science, Austrian Academy of Sciences as part of the European Research Council (ERC) project SpdTUM and was financially supported by the ERC under the European Union's Horizon 2020 research and innovation programme (Grant No. 757333).

Copyright © 2020 by Martin Stücker. All rights reserved.

Erich Schmid Institute of Materials Science

Austrian Academy of Sciences

Jahnstraße 12

A-8700 Leoben



MONTANUNIVERSITÄT LEOBEN

www.unileoben.ac.at

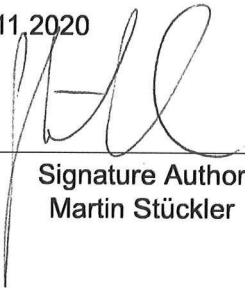
EIDESSTÄTLICHE ERKLÄRUNG

I declare on oath that I wrote this thesis independently, did not use other than the specified sources and aids, and did not otherwise use any unauthorized aids.

I declare that I have read, understood, and complied with the guidelines of the senate of the Montanuniversität Leoben for "Good Scientific Practice".

Furthermore, I declare that the electronic and printed version of the submitted thesis are identical, both, formally and with regard to content.

Datum 26.11.2020



Signature Author
Martin Stückler

Abstract

In this thesis, severe plastic deformation by high-pressure torsion is used to produce magnetic materials with tunable properties. Magnetic tunability is ensured by using combinations of materials, which exhibit large miscibility gaps in the thermodynamical equilibrium and consist therefore of one diamagnetic element and at least one ferromagnetic element. Upon processing a considerable grain refinement and intermixing is observed for certain compositions, whereas a microstructural steady state is aimed for each composition investigated. For an understanding of the structure-property relationship in severely plastically deformed materials, a large focus of this study is on the correlation of magnetic and microstructural properties.

A spin-glass state, arising in as-deformed Fe-Cu specimens, clearly demonstrates the formation of a supersaturated solid solution upon high-pressure torsion. Tiny, residual Fe-rich particles give rise to superparamagnetic behavior. The amount of the residual Fe-particles is controlled by the composition, maintaining a switching between superparamagnetism to a spin-glass state. A remarkable tunability in the magnetic properties was found by annealing treatments already at relatively low temperatures, enabling a change between superparamagnetic to single-domain and even multi-domain behavior. The replacement of Cu with Ag leads to bulk ferromagnetic properties. For the Ag-based alloys, different deformation behaviors were observed, which are traced back to differences in the mechanical properties of the alloying elements.

For the Co-Cu system single-phase solid solutions with ferromagnetic properties develop, whereat large Co-contents exhibit soft magnetic properties. The magnetic moment and the coercivity in the Co-Cu system is found to be controlled by the Co-to-Cu ratio. Furthermore the coercivity is tuned by subsequent thermal treatments, whereby these alloys have been found to exhibit a remarkable thermal stability regarding the microstructure. A further improvement in terms of soft magnetic properties was achieved by substituting small amounts of Co with Fe. For larger Fe-contents, the magnetic behavior changes and a considerable large coercivity is observed.

Kurzfassung

In der vorliegenden Arbeit wird die Herstellung von magnetischen Materialien mit einstellbaren Eigenschaften über Hochverformung mittels Hochdrucktorsion untersucht. Die magnetischen Eigenschaften können durch die Verwendung von Materialkombinationen variiert werden, welche im thermodynamischen Gleichgewicht große Mischbarkeitslücken aufweisen. Die untersuchten Materialsysteme bestehen deshalb aus einem diamagnetischen und mindestens einem ferromagnetischen Element. Bei der Herstellung wird eine Kornfeinung erreicht. Einige Zusammensetzungen weisen eine Durchmischung der Elemente auf. Für alle untersuchten Zusammensetzungen wird das Erreichen einer stabilen Mikrostruktur angestrebt. Zur Untersuchung der Struktur-Eigenschaft Beziehung in hochverformten Materialien, widmet sich diese Studie zu einem großen Teil der Korrelation zwischen magnetischen und mikrostrukturellen Eigenschaften.

Ein Spin-Glas Zustand, welcher in verformten Fe-Cu Proben auftritt, zeigt eindeutig die Bildung eines übersättigten Mischkristalls durch Hochdrucktorsion. Winzige, noch vorhandene Fe-reiche Partikel rufen superparamagnetisches Verhalten hervor. Der Anteil an Fe-reichen Partikeln wird über die Zusammensetzung gesteuert, was ein Umschalten zwischen superparamagnetischen und Spin-Glas Verhalten ermöglicht. Eine beachtliche Variation der magnetischen Eigenschaften wird bereits durch Glühbehandlungen bei vergleichsweise geringen Temperaturen erreicht. Dadurch werden Änderungen von superparamagnetischen Verhalten über Ein-Domänen bis hin zu Mehr-Domänen Konfigurationen erreicht. Wird Cu durch Ag ersetzt bilden sich ferromagnetische Eigenschaften aus. Die Ag-basierten Legierungen weisen ein anderes Verformungsverhalten auf, welches auf die stark unterschiedlichen mechanischen Eigenschaften der Legierungselemente zurückgeführt wird.

Im Co-Cu System bilden sich einphasige Mischkristalle mit ferromagnetischen Eigenschaften, wobei weichmagnetische Eigenschaften für hohe Co-Gehalte erreicht werden. Das magnetische Moment und die Koerzitivfeldstärke werden über das Verhältnis zwischen Cu und Co gesteuert. Darüber hinaus erfolgt ein weiteres Abstimmen der Koerzitivfeldstärke durch anschließende Glühbehandlungen, wobei eine hohe thermische Stabilität der Mikrostruktur festgestellt

Kurzfassung

wurde. Die Substitution von geringen Teilen von Co mit Fe führt zu einer Verbesserung der weichmagnetischen Eigenschaften. Erhöhte Anteile von Fe führen hingegen zu einer Erhöhung der Koerzitivfeldstärke.

Acknowledgment

During the last years, I had the great opportunity to work with many people from a lot of different places. At this point I want to thank them for supporting me in my research, the preparation of this thesis, or also in administrative concerns:

- **Prof. Dr. Reinhard Pippan** who supervised me throughout the thesis. He supported me with many ideas and also pointed out different points of view on the scientific issues I was working on.
- **Dr. Andrea Bachmaier** who gave me the opportunity to spend my thesis working in a fantastic research group. At this point I want to thank her for taking much time for discussions. She was also very open minded for my ideas and enriched this thesis with her great supervision.
- **Prof. Dr. Roland Würschum** (Technische Universität Graz) who guided me after my master's thesis to the Erich Schmid Institute. He supported me in my scientific carrier and I am glad that he willingly agreed to supervise this thesis as a mentor.
- **Dr. Stefan Wurster** for plenty of help during my time at the Erich Schmid Institute. He always found time to discuss current issues and supported me in my experimental work.
- **Lukas Weissitsch** who supported me enthusiastically throughout my thesis, regardless in which concern.
- **Manoel Kasalo** for his reliability and also the motivation to participate in this project as a student worker.
- **Prof. Dr. Heinz Krenn** (Karl-Franzens-Universität Graz) who spent much time discussing the analysis of SQUID data and provided many ideas regarding magnetic measurements.
- **Prof. Dr. Christian Teichert** (Montanuniversität Leoben) who was teaching me many things about scanning probe microscopy and made facilities for magnetic force microscopy investigations available.

Acknowledgment

- **Dr. Aleksandar Matković** (Montanuniversität Leoben) who spent much time training me at the magnetic force microscope.
- **Prof. Dr. Peter Felfer** (Friedrich-Alexander-Universität Erlangen-Nürnberg) who willingly carried out atom probe tomography experiments on my samples and was teaching me the basics of analyzing atom probe data.
- **Prof. Dr. Baptiste Gault** (Max-Planck-Institut für Eisenforschung GmbH) who showed me the pitfalls of modern atom probe tomography and **Dr. Philipp Kürsteiner** who enthusiastically provided huge atom probe data sets.
- **Dr. Christoph Gammer** and **Dr. Jakub Zálešák** who enriched this research project with detailed TEM investigations.
- **Dr. Timo Müller** (DESY Hamburg) who patiently supervised our synchrotron-XRD experiments and was immediately available in case that problems occurred.
- **Dr. Lorenz Romaner** and **Dr. Oleg Peil** (Materials Center Leoben) for having several attempts in simulating magnetic properties of the samples investigated in this study, although the issue was found to be more complex than expected in the beginning.
- **Daniela Brunner** for courteously supporting me in any administrative concern
- I furthermore want to thank our metallographers **Silke Modritsch**, **Karoline Freitag** and **Vanessa Toppler** for carefully polishing samples for SEM investigations as well as the workshop staff **Franz Hubner**, **Robin Neubauer** and **Marco Reiter** who carried out every work with lots of precision. I also want to thank **Peter Kutleša** for rapidly helping in any issue concerning the HPT.
- Moreover, I want to thank the whole staff of the Erich Schmid Institute of Materials Science for the pleasant working atmosphere.

List of abbreviations

AFM atomic force microscopy

APT atom probe tomography

BSE backscattered electrons

DIAM distribution of isolated atoms for the determination of matrix composition

EBS electron backscatter diffraction

EDS energy dispersive X-ray spectroscopy

FC field cooling

HAADF high-angle annular dark-field

HPT high-pressure torsion

MFM magnetic force microscopy

RT room temperature

RKKY Ruderman-Kittel-Kasuya-Yosida

SEM scanning electron microscopy

SPD severe plastic deformation

SQUID superconducting quantum interference device

TEM transmission electron microscopy

TKD transmission Kikuchi diffraction

UFG ultrafine-grained

XRD X-ray diffraction

ZFC zero field cooling

Contents

Abstract	iii
Kurzfassung	v
Acknowledgment	vii
List of abbreviations	ix
1. Introduction	1
1.1. Structure-property relationships in ferromagnetic materials	1
1.2. Motivation and aim of the work	3
1.3. High-pressure torsion	4
1.4. Methodologies for resolving structure-property relationships	5
1.4.1. Atom probe tomography data analysis	5
1.4.2. Magnetic force microscopy	8
1.4.3. Magnetometry	9
1.4.4. AC-hysteresis measurement	10
2. Results and discussion	13
2.1. Magnetic tunability in Fe-Cu solid solutions	13
2.2. Towards soft magnetic tunability in Co-Cu	18
2.3. Superior soft magnetic properties in Cu-Fe-Co alloys	21
2.4. Magnetic properties in Ag-based materials systems	24
3. Summary and Outlook	27
4. Bibliography	29
5. List of appended publications and proceedings	35

A. Magnetic Binary Supersaturated Solid Solutions Processed by Severe Plastic Deformation	37
A.1. Introduction	38
A.2. Materials and Methods	39
A.3. Results and Disussion	40
A.3.1. Microstructure	40
A.3.2. Magnetism	42
A.4. Conclusions	45
A.5. References	47
B. Magnetic dilution by severe plastic deformation	49
B.1. Introduction	49
B.2. Experimental	50
B.3. Results and Discussion	51
B.3.1. Microstructural Characterization	51
B.3.2. Magnetic Properties	51
B.3.3. Atom probe tomography	55
B.4. Conclusion	55
B.5. References	56
C. Intermixing of Fe and Cu on the atomic scale	59
C.1. Introduction	60
C.2. Experimental	61
C.3. Results and Discussion	62
C.3.1. Microstructural evolution as a function of temperature	62
C.3.2. Magnetic Properties	67
C.3.3. RKKY-interaction as origin of the magnetic frustrated phase	75
C.4. Conclusion	76
C.5. References	77
D. On the magnetic nanostructure of a Co-Cu alloy processed by high-pressure torsion	83
D.1. Introduction	84
D.2. Experimental	84
D.3. Results and Discussion	85
D.3.1. Sample synthesis with high Co-content	85

D.3.2. Investigations on the thermal stability	87
D.4. Conclusion	95
D.5. References	97
E. Formation of supersaturated solid solutions of Cu-Fe-Co by severe plastic deformation	101
E.1. Introduction	102
E.2. Experimental	102
E.3. Results and Discussion	103
E.3.1. Supersaturated solid solutions by HPT	103
E.3.2. Evolution of the supersaturated state upon annealing	107
E.4. Conclusion	110
E.5. References	110
F. In-situ AC-hysteresis measurements of SPD-processed $\text{Cu}_{20}(\text{Fe}_{15}\text{Co}_{85})_{80}$	113
F.1. Introduction	113
F.2. Experimental	114
F.3. Results and Discussion	114
F.4. Conclusion	119
F.5. References	119

1. Introduction

1.1. Structure-property relationships in ferromagnetic materials

Ferromagnetic materials exhibit spontaneous ordering, meaning the spins align parallel to each other without any external force. Therefore, these materials can exhibit a magnetization even in absence of an external field. In ferromagnetic materials, areas of the same direction of magnetization form out, which are denoted as domains and separated by domain walls. Typically, a ferromagnet consists of several domains. Size of the domains and their magnetization direction yield the magnetization of the ferromagnet. The overall magnetization can be reduced to zero when applying a field in the opposite direction of the magnetization. This field is called coercive field or coercivity. By cycling a full loop (i.e. saturation along one direction, saturation in the opposite direction and back again), energy is partially converted into heat. The energy loss is given by the hysteresis loops' area, being mainly controlled by the coercivity. Based on the coercivity, magnetic materials can be separated into two different types: hard and soft magnetic materials. Hard magnetic materials exhibit large coercivities and can be found, e.g., in loudspeakers, electric motors or simply as refrigerator magnets. In contrast, soft magnetic materials exhibit low coercivities. Their main areas of application are magnetic shielding and conversion of electric energy, e.g. in transformers. As in transformers, full hysteresis loops are passed in fractions of seconds, the accompanying energy loss plays a key role in such devices. By tuning the coercivity, the energy efficiency of such devices can be improved significantly [1–3].

It is known for quite a while that the coercivity depends on the microstructure, in particular a correlation to grain size has been found. Smallest coercivities are usually achieved for large grain sizes, which is because domain walls can move unimpeded, whereas for small grain sizes, grain boundaries hinder the domain wall motion [2]. In the mid 1970s, small coercivities were as well observed in amorphous materials [4]. This quite surprising result was traced back to an exorbitant reduction in magnetocrystalline anisotropy, since in such

1. Introduction

materials no easy axis can form. This effect has been observed for nanocrystalline materials in the early 1990s as well [5]. A theoretical model, describing the dependence of coercivity on grain size, was developed in the mid 1990s and is still state of the art [6]. Fig. 1.1 shows the coercivity as a function of grain size. Large grain sizes favor soft magnetic properties. As the grain size decreases the coercivity increases until a state forms, in which the grain size equals the domain size, i.e. single domain behavior. Further decrease in grain size causes the magnetocrystalline anisotropy to average out, leading to a reduction in coercivity, which is proportional to the sixth power of the grain size.

The interplay of microstructure and magnetic properties does not only apply to coercivity. Instead, nanoscaled materials show unique magnetic effects, as for example superparamagnetism [7]. As the volume of an isolated ferromagnetic particle falls below a certain limit, an initially magnetized particle loses its magnetization in a specific period of time (the so-called Néel relaxation time). This effect occurs because the energy barrier to fall into a demagnetized state (which scales with volume) can be overcome by thermal energy. Although the model describes the behavior of isolated ferromagnetic particles, it has also been observed for ferromagnetic particles in a non-magnetic matrix [8].

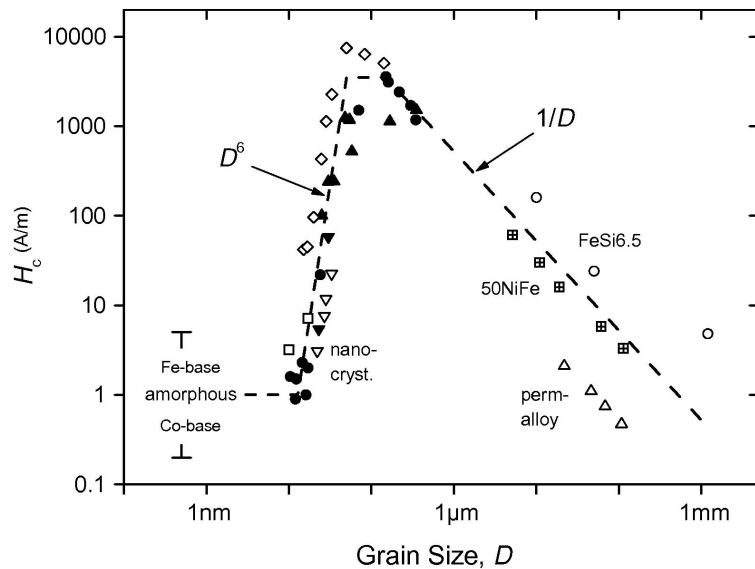


Figure 1.1.: Coercivity as a function of grain size. Reprinted from [9] with permission from Elsevier.

1.2. Motivation and aim of the work

Magnetic components can be found in a lot of everyday objects and are centerpieces of many electronic devices. A significant role of magnetic materials is also their use in the fields of sustainable energy and electric mobility, as electromagnetic interactions are fundamental in electric motors or generators and also in conversion of electrical energy. The usage of magnetic materials is of course not only limited to energy applications and consumer electronics, but is manifold as magnetic materials are also used in mechanical engineering (e.g. bearings), data storage (e.g. hard disc drive HDD), refrigeration [10], medicine (e.g. magnet resonance tomography MRT or blood cleansing [11]), or even in the generation of highly brilliant X-ray beams (undulators in synchrotron facilities) to name a few. Although being all magnetic materials, for every application certain requirements must be met, which is where materials science sets in.

In terms of soft magnetic materials, superior properties can be achieved for smallest grains as described above. Currently, such materials are commercially available and processed from amorphous sheets. The magnetic properties are tuned by subsequent annealing treatments causing the formation of ferromagnetic nanometre-sized particles. The superior magnetic properties come with the drawback of high production costs due to complex manufacturing processes. Furthermore, for the production of bulk materials subsequent processing steps such as stacking of sheets need to be carried out. The synthesis of soft magnetic materials, which are directly available in bulk form, is therefore desirable.

With sample processing by high-pressure torsion (HPT), a technique of severe plastic deformation (SPD), bulk materials can be produced [12]. Moreover, grain refinement can be induced down to hundreds or even tens of nanometers [13]. A concomitant change in the magnetic properties has already been reported [14–17], although very few research is available on this topic. Furthermore, it has to be stated that the interplay between microstructure and magnetic properties in SPD materials is poorly understood owing to the complex microstructure. For this purpose, the main focus in this thesis is on the correlation of magnetic properties and microstructure. For an in-depth investigation of the structure-property relationships, the usage of cutting edge methodologies is necessary, such as atom probe tomography (APT), magnetic force microscopy (MFM) and magnetometry by using a superconducting quantum interference device (SQUID).

The aim of this thesis is the synthesis of magnetically tunable and soft magnetic materials. Magnetic tunability is ensured by the usage of elements which do not mix in the thermodynamical equilibrium. For this purpose the sample compositions investigated in this

1. Introduction

study consist of one diamagnetic (Cu, Ag) and at least one ferromagnetic component (Fe, Co). Upon HPT-deformation the formation of supersaturated solid solutions is aimed for, delivering homogeneous material properties.

1.3. High-pressure torsion

In this thesis, sample synthesis is performed by HPT. Initially invented by Bridgman in the 1930s to study materials under high-pressure [18], HPT experienced a renaissance since Valiev and co-workers found this method to be capable of grain refinement [19]. In HPT, a coin-shaped specimen is located between two anvils under large hydrostatic pressure (several GPa). The anvils rotate against each other, resulting in large shear strain acting onto the material. During deformation, the geometry of the sample does not change. The achieved shear strain γ can be calculated according to the following equation [12]:

$$\gamma = \frac{2\pi nr}{t} \quad (1.1)$$

where n is the number of turns, r is the radius and t is the sample thickness. Theoretically, a coin-shaped HPT-sample reflects therefore all states between $\gamma(r = 0) = 0$ and $\gamma(r = r_{MAX})$. For large numbers in γ , a steady state is achieved, meaning that the microstructure does not change anymore as γ increases [20]. Such a homogeneous microstructure is desirable to achieve uniform properties over a sufficient large radius. A steady state regime is usually observed, when applying high numbers of turns and was found to originate from grain boundary migration [21].

By HPT-deformation of multi-phase materials, intermixing can be observed, even for materials which do not mix in thermodynamical equilibrium, resulting in supersaturated solid solutions [22]. The occurrence and the grade of supersaturation depend on the used materials and the driving force to induce supersaturation is still not well understood [23].

HPT-deformation results in a large number of lattice defects and grain refinement. As the shear strain increases, the grain size decreases until a microstructural saturation is reached. Whereas in single phase materials the saturation grain size is found to be in the ultrafine-grained (UFG) regime [20], multiphase materials exhibit lower saturation grain size and even attain the nanocrystalline regime [24], as shown in fig. 1.2. Furthermore, it was found that the saturation grain size can be controlled by the deformation temperature, which is attributed to the enhanced mobility of triple junctions [25].

1.4. Methodologies for resolving structure-property relationships

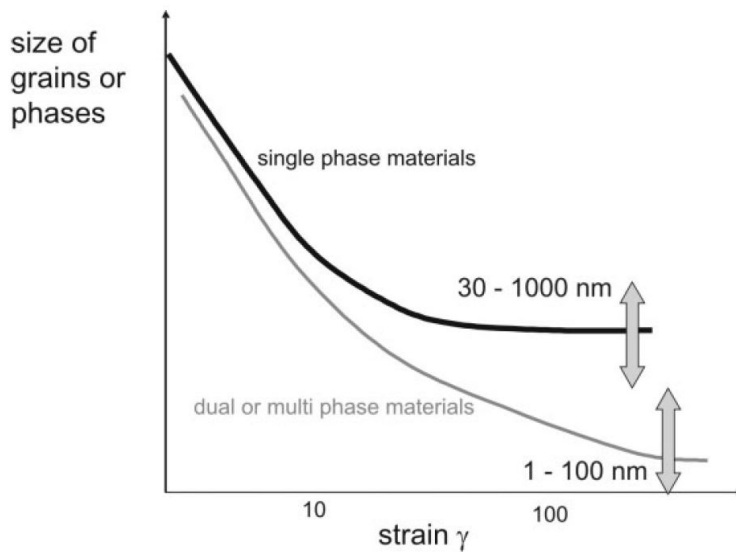


Figure 1.2.: Sketched evolution of the grain size as a function of strain for single-phase and multiphase materials by HPT. Reprinted from [24] with permission from John Wiley & Sons.

1.4. Methodologies for resolving structure-property relationships

The preparation of materials by SPD results in complex, non-equilibrium microstructures. To be able to correlate microstructural and magnetic properties, an in-depth analysis of both is crucial. The methods used in this thesis for investigating microstructural and magnetic properties are briefly presented in the following chapters.

1.4.1. Atom probe tomography data analysis

APT is a characterization method to gain a 3-dimensional image of the sample's atomic arrangement. A needle-shaped specimen is exposed to a pulsed high-voltage. Due to the extreme curvature of the tip of the needle, the electric field rises in the vicinity of the sample's tip, such that individual atoms overcome the binding energy, i.e., evaporate. The atoms are directed towards a detector, gaining the lateral atomic position. In-depth position and mass-to-charge ratio are measured by time-of-flight mass spectroscopy. From this data, a 3d-image, i.e. reconstruction, of the atomic structure can be calculated ending up in a four-dimensional dataset (x -, y -, z -position, mass-to-charge ratio). To suppress thermal artifacts, such measurements are usually conducted at cryogenic temperatures [26].

1. Introduction

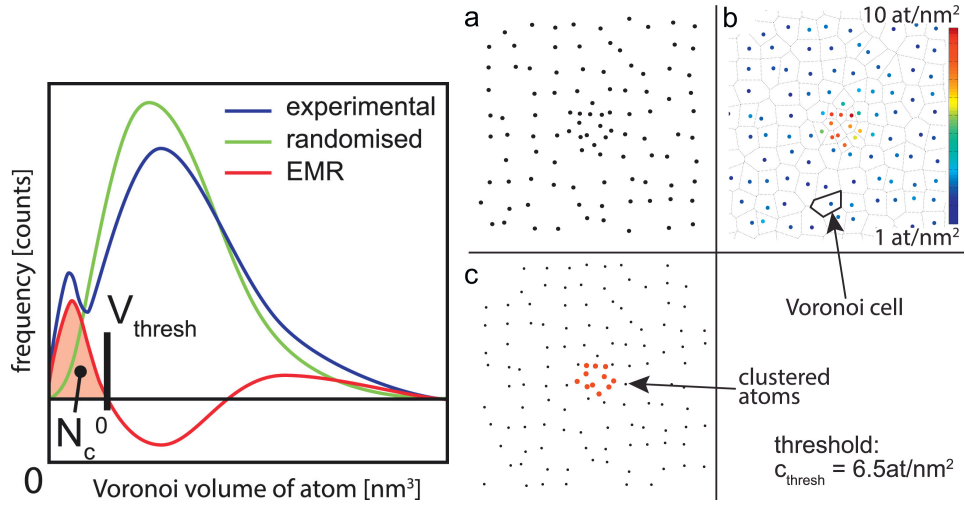


Figure 1.3.: Cluster analysis with Voronoi-cells. On the left, the experimental and the randomized distribution of Voronoi-volumes is shown. The experimental minus random curve (EMR) gives the threshold for the volume V_{thresh} and the amount of significantly clustered atoms N_c^0 . On the right, the extraction of clustered atoms is shown as an example for 2-dimensional distributed atoms (a). First, the Voronoi-volumes are calculated (b). Atoms with a concentration larger than c_{thresh} (Voronoi-volume smaller than V_{thresh}) are the ones, which are significantly clustered (colored red in (c)). Reproduced from [30] with permission from Elsevier.

The quantitative analysis of a reconstruction has to be treated with caution, since errors, inherent to the field evaporation process occur: in the preparation of the reconstruction, often a hemispherical sample tip is assumed, which does not necessarily reflect the true shape of the specimen [26], but the initial shape can be determined with transmission electron microscopy (TEM) investigations which have to be conducted beforehand [27]. In [28] it was shown, that the spatial resolution in APT depends on the crystal orientation, whereas the resolution is worse in lateral direction than in-depth. Furthermore, the trajectories of different atomic species differ, causing errors in the reconstruction, referred to as "chromatic aberrations" [29].

Quantitative evaluation of the reconstruction is therefore often based on the analysis of atomic distributions since the reconstruction provides good statistics due to the large dataset. One type of analysis is therefore cluster analysis, for instance based on the evaluation of Voronoi-volumes [30]. The Voronoi-volumes are evaluated for one or more atomic species. To reveal the amount of significantly clustered atoms, this data are subtracted from the distribution of Voronoi-volumes measured for a randomized data set revealing an upper limit for cluster size. An example for the extraction of clustered data is shown in fig. 1.3.

1.4. Methodologies for resolving structure-property relationships

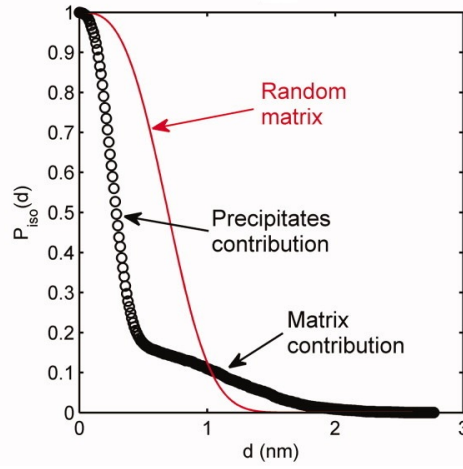


Figure 1.4.: Probability of a solute atom to be isolated. Reproduced from [31] with permission from John Wiley & Sons

The analysis based on Voronoi-volumes depends on a parameter, which is gained from a randomized data set. In contrast, De Geuser proposed an algorithm based on the evaluation of nearest-neighbor distances which does not depend on any input parameter. The distribution of isolated atoms for the determination of matrix composition (DIAM) is based on the analysis of the radial distribution function, i.e., the analysis of the nearest-neighbor distances only [31]. We consider a volume, consisting of two atomic species A and B. Species B is present in form of precipitates (concentration C_p) as well as embedded in the matrix (concentration C_m). The probability of finding two atoms of species B at distance d reads then:

$$P_{iso}(d) = f C_p/C_0 e^{-\frac{4\pi}{3}d^3} \rho_p + (1 - f) C_m/C_0 e^{-\frac{4\pi}{3}d^3} \rho_m \quad (1.2)$$

with C_0 being the overall concentration of B in the observed volume, f being the molar fraction of precipitates, ρ_p and ρ_m represent the average atomic density of species B in the precipitate and matrix, respectively. The evaluated nearest-neighbor distance can therefore be described in terms of precipitates as well as matrix contribution, as shown in fig. 1.4. In further studies [32] it has been shown that the precipitates volume fraction can be written as:

$$f_V = \frac{C_0 - C_m}{C_p - C_m} \quad (1.3)$$

The DIAM analysis has also been compared to data from small-angle scattering revealing a good agreement for large precipitate sizes [33], but show that the size might be overestimated for too small precipitates due to, e.g., chromatic aberration [29].

1. Introduction

1.4.2. Magnetic force microscopy

In MFM, a magnetic tip is mounted on a cantilever. The tip is scanned over a sample, and the interaction between tip and sample is measured. The magnetic interaction of tip and sample can be expressed as

$$\vec{F} = \nabla(\vec{m} \cdot \vec{B}) \quad (1.4)$$

m represents the magnetic moment of the tip and B is the magnetic stray field of the sample at the position of the tip. As this force is usually rather small (in the range of 10^{-11} N), the magnetic interaction cannot be measured by determining the cantilever's bending, but instead, dynamic measurement techniques are used. In such types of measurements the cantilever is operated close to its resonance frequency ω . Any interaction between tip and sample changes the cantilever's effective spring constant and therefore the resonance frequency according to [34] by

$$\Delta\omega \approx -\frac{\omega_0}{2k} \frac{dF}{dz} \quad (1.5)$$

with k being the spring constant of the cantilever. The tip-to-sample interaction is therefore monitored by the shift of the resonance frequency. Instead of the force, the force gradient is measured in this mode.

Due to a small tip volume, the interaction is also restricted to a small volume, given by the stray field. To attain high resolution, small tips are therefore favorable [35]. The higher resolution comes with the drawback of a smaller signal, since smaller volume causes less interaction.

For the purpose of gaining a scan signal which does only include magnetic interactions, it is necessary to separate topographic effects. Therefore, scans are usually performed in two-pass mode: in the first pass the topography is measured yielding an atomic force microscopy (AFM) scan signal. In the second pass the tip is raised to a predefined lift height (usually tens or hundreds of nanometres) and the MFM data are acquired by keeping the tip to sample distance constant.

To quantitatively analyze the MFM data, methods which have been employed for surface roughness characterization by AFM and soft X-ray diffraction [36, 37] can be used for MFM as well [38, 39]. These procedures consider the autocorrelation function and the height-height correlation function [40]. The auto-correlation function $C(x)$ is calculated for each line in the scan and is written

$$C(x) = \langle [z(x_0 + x) - \langle z \rangle][z(x_0) - \langle z \rangle] \rangle \quad (1.6)$$

1.4. Methodologies for resolving structure-property relationships

with z representing the phase signal of the MFM signal. The calculated auto-correlation function can then be approximated by, e.g., a self-affine surface with a cut-off, reading

$$C(x) = \sigma^2 e^{-(|x|/\xi)^{2\alpha}} \quad (1.7)$$

with σ representing the standard deviation of the magnetic signal (for AFM this value represents the root mean square roughness). ξ is the lateral correlation length, i.e., the length scale within two points of the scan correlate. α is the Hurst parameter, describing the "jaggedness" of the signal and ranges from 0 to 1. Small values in α represent sudden fluctuations in the phase signal. Another function describing surface roughness is the height-height correlation function

$$H(x) = \langle [z(x_0 + x) - z(x_0)]^2 \rangle \quad (1.8)$$

exhibiting the following behavior [40]

$$H(x) = \begin{cases} x^{2\alpha} & \text{for } x \ll \xi \\ 2\sigma^2 & \text{for } x \gg \xi \end{cases} \quad (1.9)$$

The parameter set of σ , ξ and α is calculated from both functions, yielding quantitative description of the scan signal and thus the magnetic structure of the investigated material.

1.4.3. Magnetometry

In magnetometry, the magnetic moment is measured as a function of field and / or temperature. Such measurements are typically performed in DC-mode, representing the static properties of a magnetic material. An example for a magnetometric scan is the hysteresis, as the magnetic moment is measured as a function of the magnetic field. To fully characterize the behavior of a magnetic material, temperature dependent scans have to be performed. The measurement of the saturation magnetic moment versus temperature for instance, reveals the Curie temperature. Furthermore, zero field cooling (ZFC) and field cooling (FC) scans should be mentioned at this point, which are usually performed between room temperature and cryogenic temperatures [41, 42].

In ZFC mode, a demagnetized sample is cooled in absence of an external field. At the lowest temperature a magnetic field is switched on and the magnetic moment is measured upon heating. As the highest temperature is reached, the sample is cooled and the magnetic

1. Introduction

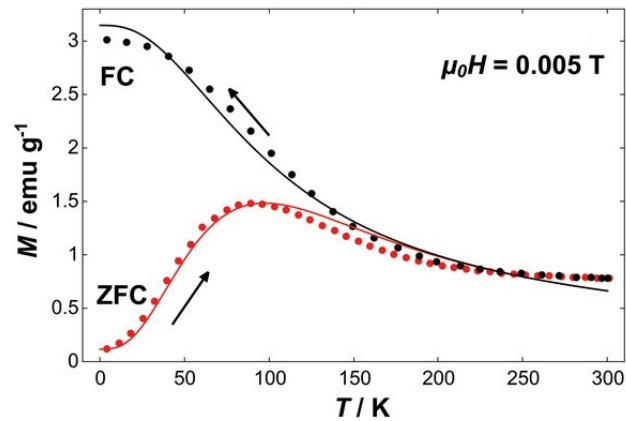


Figure 1.5.: ZFC (red) and FC curves (black) for nanoporous Pd(Co). Arrows indicate temperature sweep direction. Reproduced under the terms of the CC-BY 4.0 license. [46] © 2019, John Wiley & Sons.

moment is measured during cooling. The latter measurement is called FC measurement. From the temperature dependence of both curves, for instance magnetic phase transitions can be observed, as for example superparamagnetism [43], spin-glass behavior [44] or superconductivity [45]. Fig. 1.5 shows the magnetic moment of nanoporous Pd(Co) as an example, measured in ZFC and FC condition [46]. The splitting of both curves represents a behavior typical for superparamagnetism, with the maximum in ZFC representing the superparamagnetic blocking temperature. Below the blocking temperature, the material behaves ferromagnetic. Above the blocking temperature, the magnetization decays, since the energy barrier can be overcome by thermal energy. This behavior is usually observed for ferromagnetic particles with several nanometers in size, embedded in a non-magnetic matrix.

1.4.4. AC-hysteresis measurement

As mentioned above, the application of soft magnets involves cycling of the hysteresis loop in fractions of seconds. Therefore, also the investigation of the dynamic magnetic behavior is crucial. For AC-hysteresis measurements a wound core is fabricated. The core material is made of the material to be investigated, whereas two wire coils are wound on, which are denoted as primary and secondary windings in the following [47, 48]. Usually these measurements are performed on a ring-core sample, since shape anisotropy can be neglected for such geometries. Applying an electrical current on the primary coil leads to a magnetic

1.4. Methodologies for resolving structure-property relationships

field H , according to

$$H(t) = \frac{I(t) \cdot N_P}{l_m} \quad (1.10)$$

In the above equation, I is the applied current, N_P is the number of primary windings and l_m is the mean length of the core material. The induced magnetic voltage V in the secondary winding yields the magnetic flux B

$$B(t) = \frac{\int U(t') dt'}{N_S \cdot A} \quad (1.11)$$

in the above equation, N_S stand for the number of windings and A is the cross-section area of the core material. From monitoring the time-dependent H and B , the magnetic hysteresis is generated.

The dynamic behavior can therefore be investigated by tuning the applied current according to [eq. 1.10]. Exposing the material to high frequencies of the magnetic field leads to larger losses. This behavior is reflected in the measurements by an increasing area of the hysteresis loop for an increasing frequency. A mathematical model describing the evolution of the energy losses as a function of frequency reads as follows

$$W(f) = W_h + W_{cl}(f) + W_{exc}(\sqrt{f}) \quad (1.12)$$

[Eq. 1.12] shows that the losses can be separated into three different terms, which are the (static) hysteresis loss W_h , the classical loss W_{cl} and the anomalous or excess loss W_{exc} [49–51]. The classical loss depends on the formation of eddy currents and is linearly proportional to the frequency f . The excess loss W_{exc} is controlled by the motion of domains and scales with \sqrt{f} [52]. Furthermore the (static) hysteresis loss W_h can be evaluated from an extrapolation of the loss curve to $f \rightarrow 0$.

2. Results and discussion

Starting with conventional powders, in total five different systems are investigated, each consisting of one diamagnetic element and at least one ferromagnetic element: Cu-Fe, Cu-Co, Cu-Fe-Co, Ag-Fe and Ag-Co. For each composition the formation of a nanocrystalline saturated state from initial powders is aimed. Therefore a homogeneous deformation by HPT has to be ensured. Investigations regarding the microstructure as well as the magnetic properties are carried out as depicted in fig. 2.1. In the following, the results are presented individually for the different material systems.

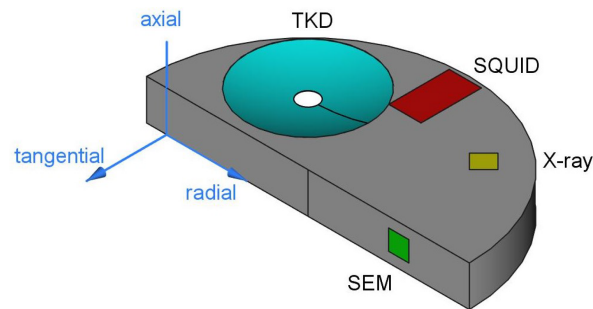


Figure 2.1.: Schematic layout of one half of an HPT-sample. The used methods with their respective observation directions are highlighted. Reproduced under the terms of the CC-BY 4.0 license. [53] © 2019, MDPI.

2.1. Magnetic tunability in Fe-Cu solid solutions

To achieve a saturated steady state in Fe-Cu solid solution, the necessary deformation has been evaluated. The hardness is very sensitive to the microstructure and can be used to estimate the formation of the saturated state. In fig. 2.2 the hardness as a function of shear strain γ is shown for as-deformed Fe14wt.%-Cu. The first plateau at 150 HV_{0.5} arises from the formation of substructures and is already reached at small strains. A significant

2. Results and discussion

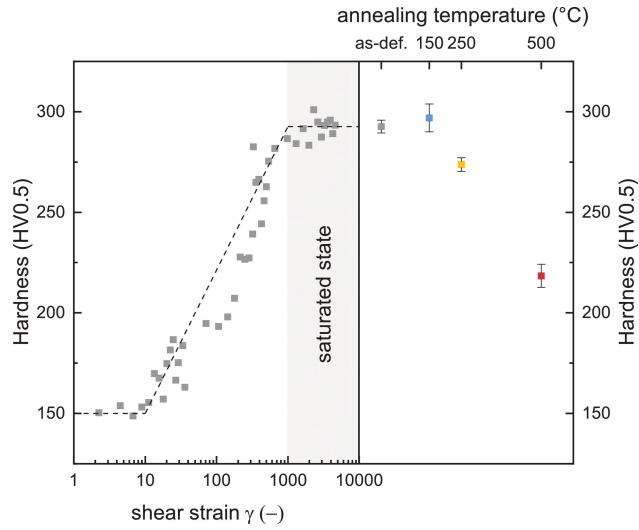


Figure 2.2.: Vickers hardness of HPT-deformed Fe14wt.%-Cu. On the left, the hardness as a function of shear strain γ is shown in as-deformed state, revealing a saturation for $\gamma \geq 1000$. On the right, the mean hardness ($\gamma \geq 1000$) is shown as a function of annealing temperature. Reproduced from [54] with permission from Elsevier.

rise in hardness is visible between $\gamma=10$ and $\gamma=1000$, but no further increase is visible at higher strains, indicating a microstructural saturation for $\gamma \geq 1000$. Therefore the samples investigated in the Fe-Cu system have been prepared using 100 turns leading to shear strain of $\gamma \approx 4500$ at $r=3$ mm, maintaining a microstructural saturated steady state. Scanning electron microscopy (SEM) show a homogeneous microstructure in the nanocrystalline regime.

Upon annealing treatment, a slightly higher hardness is visible for 150°C, but at higher annealing temperatures the hardness decreases, which is associated to demixing and grain coarsening. From synchrotron X-ray diffraction (XRD) (fig. 2.3), a major fcc-phase can be identified for Fe14wt.%-Cu, but small and broad reflections in the synchrotron XRD pattern point at the presence of tiny bcc-Fe particles. Similar observations are made for Fe07wt.%-Cu and Fe25wt.%-Cu.

In the following, an exhaustive analysis on the magnetic properties of as-deformed Fe14wt.%-Cu is carried out and correlated to the microstructure. The hysteresis is depicted in fig. 2.4(a) and shows a large high-field susceptibility in the as-deformed state. Furthermore, the total magnetic moment is lowered with respect to bulk-Fe as well as a coercivity in the semi-hard regime is measured. Further analysis is performed by measuring ZFC-FC-curves (fig. 2.4(b)), showing distinct peaks in the ZFC- and FC-curve, indicating superparamagnetic behavior. In-depth characterization of the magnetic behavior is carried out by AC-SQUID susceptometry, leading to the conclusion, that a spin-glass state is present as well as a superparamagnetic

2.1. Magnetic tunability in Fe-Cu solid solutions

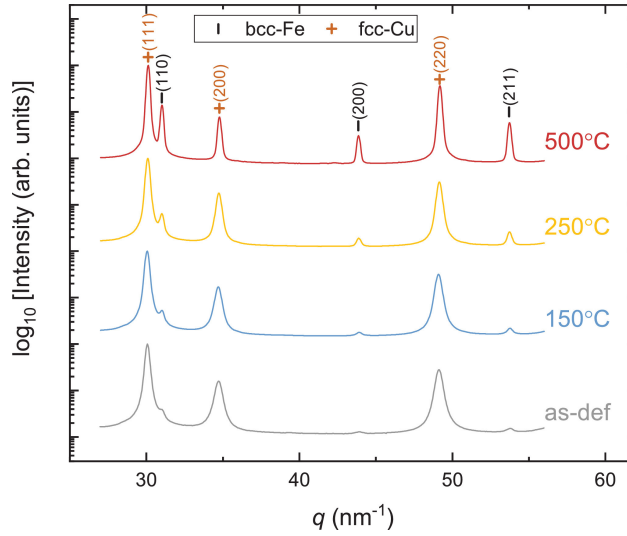


Figure 2.3.: Synchrotron XRD pattern of Fe14wt.%-Cu as a function of annealing temperature. The measurement was carried out using a beam energy of 100 keV in transmission mode. Reproduced from [54] with permission from Elsevier.

phase exists in the as-deformed state. To correlate the measured magnetic properties with the microstructure, detailed APT-investigations are carried out, as shown in fig. 2.5. In the reconstructed volumes, tiny Fe-particles are visible, whereas the concentration is investigated in the proximity of these particles, showing Fe-contents of up to 40 at.% inside the particles. The grain boundaries are investigated as well, where Fe- and Cu-concentrations have been observed to rise locally, showing large inhomogeneities along the grain boundaries. Both, the Fe-particles and Fe along the grain boundary are expected to cause the bcc-pattern in the XRD-spectra as well as the superparamagnetic behavior. The composition of the Cu-grain is investigated as well, using the DIAM-algorithm as described in section 1.4.1. The Fe-content inside the grain is determined to be 18.81 at.%. This composition exceeds the thermodynamical limit of solubility and shows the presence of a supersaturated solid solution.

Exchange coupling is sensitive to the interatomic distance. Fe, which is present in a supersaturated solid solution with Cu, exhibits a larger interatomic distance than bulk-Fe, whereas the effective exchange coupling can be calculated from Ruderman-Kittel-Kasuya-Yosida (RKKY)-interaction and covers ferromagnetic as well as antiferromagnetic exchange leading to a spin-glass state [44]. The susceptometric measurements are therefore a direct evidence of the supersaturated solid solution and the capability of HPT to tune the microstructure even on an atomic scale.

To investigate the thermal stability of the metastable state observed in the as-deformed

2. Results and discussion

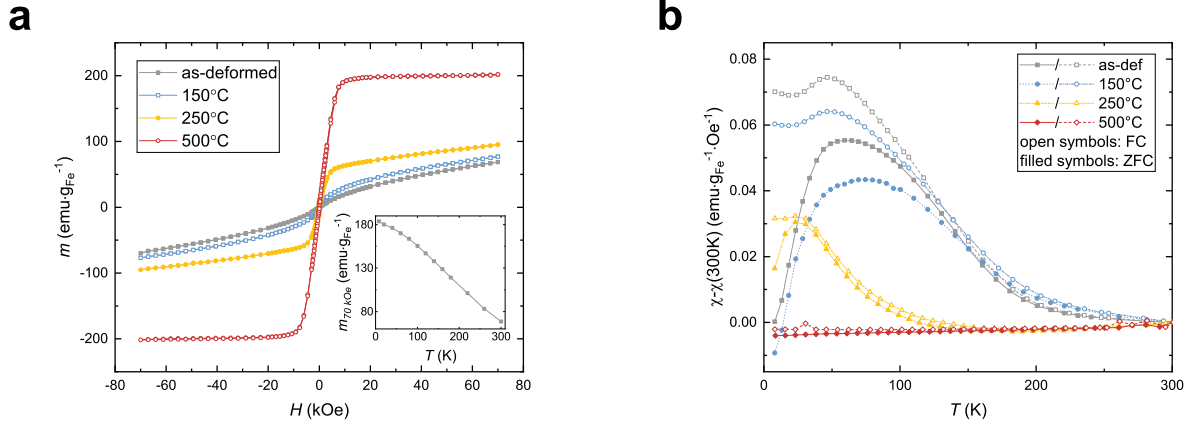


Figure 2.4.: In (a), the specific magnetic moment versus magnetic field of Fe14wt.%-Cu as a function of annealing temperatures, measured at 300 K, is shown. The inset gives the magnetic moment at 70 kOe as a function of temperature in the as-deformed state. The magnetic moment of bulk Fe is $218 \text{ emu}\cdot\text{g}^{-1}$ [2]. (b) shows ZFC-FC-curves for Fe14wt.%-Cu measured at 50 Oe as a function of annealing treatments. Adapted from [54] with permission from Elsevier.

material, magnetic measurements are conducted for the 150°C, 250°C and 500°C annealed states as well. Fig. 2.4(a) shows the hysteresis for the different annealing treatments. The decreasing slope in the high-field regime points at a diminishing Fe-content in the supersaturated solid solution. The hysteresis evolves towards a typical bulk hysteresis loop at 500°C owing to the demixing of phases. Furthermore, AC-susceptometry measurements show that the spin-glass state is not dominant anymore at 250°C. To sum up, the study on AC-susceptometry demonstrates that the magnetic properties can be changed from a ferromagnetic to a spin-glass state by HPT corresponding to a supersaturated solid solution. Furthermore, a successive removal of the spin-glass phase can be achieved by annealing treatments. The investigations on AC-susceptometry are shown in detail in Paper C.

The detailed analysis as described above is carried out for Fe14wt.%-Cu, but these results apply to Fe07wt.%-Cu and Fe25wt.%-Cu as well, since similar microstructures and magnetic properties are observed for these compositions. ZFC-FC measurements on Fe25wt.%-Cu show a larger contribution of superparamagnetism, whereas in Fe07wt.%-Cu almost no indications of superparamagnetism are observed. Since all samples have been processed with the same parameters, the varying magnetic behavior is expected to arise from different microstructural arrangements. Therefore, APT experiments have been conducted and the Fe cluster sizes have been analyzed for all three compositions by Voronoi-volumes, showing that larger clusters are present as the Fe-content increases. These results are in line with magnetometry

2.1. Magnetic tunability in Fe-Cu solid solutions

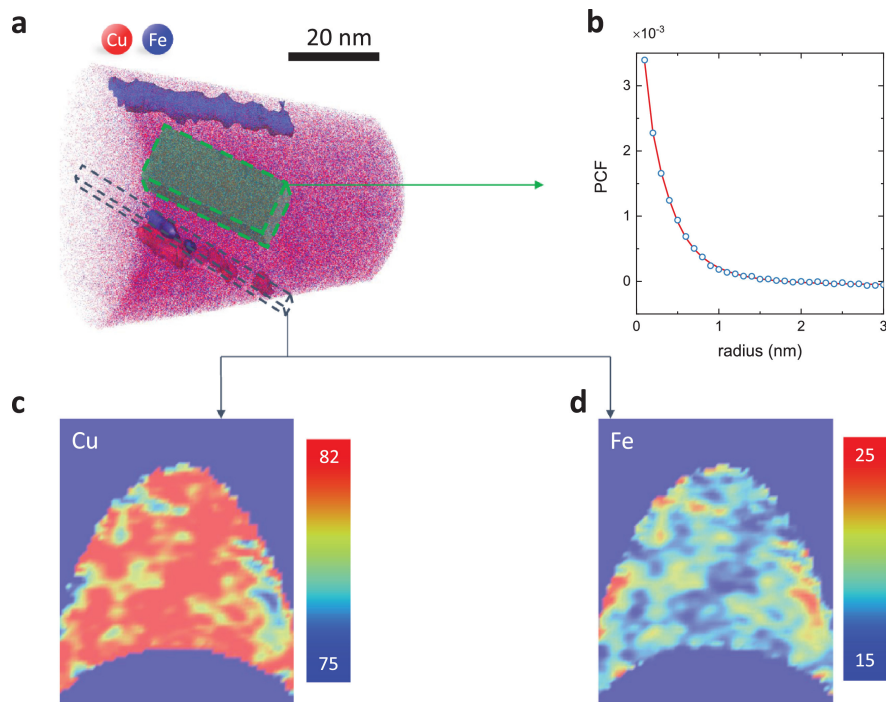


Figure 2.5.: APT analysis of Fe14wt.%-Cu. The reconstructed volume in (a) consists of Fe19.1at%-Cu80.8at.%. Isosurfaces indicate regions with 28.1at.% Fe or 63.7at.%Cu. The composition of the volume in the green box is investigated with the DIAM-algorithm, as shown in (b). (c) and (d) represent the compositions of Cu and Fe, respectively along the grain boundary (grey box in (a)). The heat maps give the composition in at.%. Reproduced from [54] with permission from Elsevier.

which shows a superparamagnetic behavior for Fe25wt.%-Cu and a spin-glass behavior for Fe07wt.%-Cu, whereas for Fe14wt.%-Cu both magnetic phases are present as shown in the AC-susceptometry study above. For the evolution of magnetic hysteresis, in particular the coercivity, a similar behavior is observed for all compositions investigated: at 150°C, stress relief takes place, leading to a diminishing coercivity according to magnetoelastic anisotropy. At intermediate annealing temperature agglomeration of Fe sets in, leading to the formation of clusters close to single-domain. Upon annealing at 500°C a ferromagnetic hysteresis curve forms, exhibiting multi-domain behavior with the saturation magnetization of bulk Fe. The study on magnetic properties for various Fe-Cu compositions is covered in detail in Paper B.

The results demonstrate a tunability from spin-glass to superparamagnetic behavior, which can be achieved by varying the Fe-content. Furthermore, the coercivity can be controlled by additional annealing treatments, which was found to cover a broad range from single-domain to multi-domain behavior.

2.2. Towards soft magnetic tunability in Co-Cu

Homogeneous microstructures have been obtained during HPT at room temperature (RT) between 28wt.% and 67wt.% of Co. For lower Co-contents residual particles are visible. RT-deformation of higher Co-contents leads to brittle specimen and accompanying crack formation. It is possible to push the limits of processing towards higher Co-contents by applying two consecutive steps of HPT-deformation at different temperatures: in the first step HPT-deformation is conducted at high temperatures (e.g. 500°C) leading to a chemical homogenization and grain refinement in the UFG-regime with absence of cracks. The second step is applied at RT causing grain refinement in the nanocrystalline regime and further homogenization. The 2-step processing method by HPT is shown in detail in paper D.

Although Co is present in hcp crystal structure in the initial powder, for all Co-Cu samples, an fcc single-phase microstructure is obtained in the as-deformed state as shown in fig. 2.6(a). The patterns of the as-deformed state exhibit an extreme peak broadening arising from the high defect density but also from grain refinement [55]. To quantify the grain size, transmission Kikuchi diffraction (TKD) measurements are carried out at multiple positions, revealing a median grain size of 100 nm (Co28wt.%-Cu), 78 nm (Co49wt.%-Cu) and 77 nm (Co67wt.%-Cu; see paper A for more details).

The composition which exhibits the highest ferromagnetic content (Co72wt.%-Cu) is prepared by a 2-step deformation process, as mentioned above, whereby investigations on the

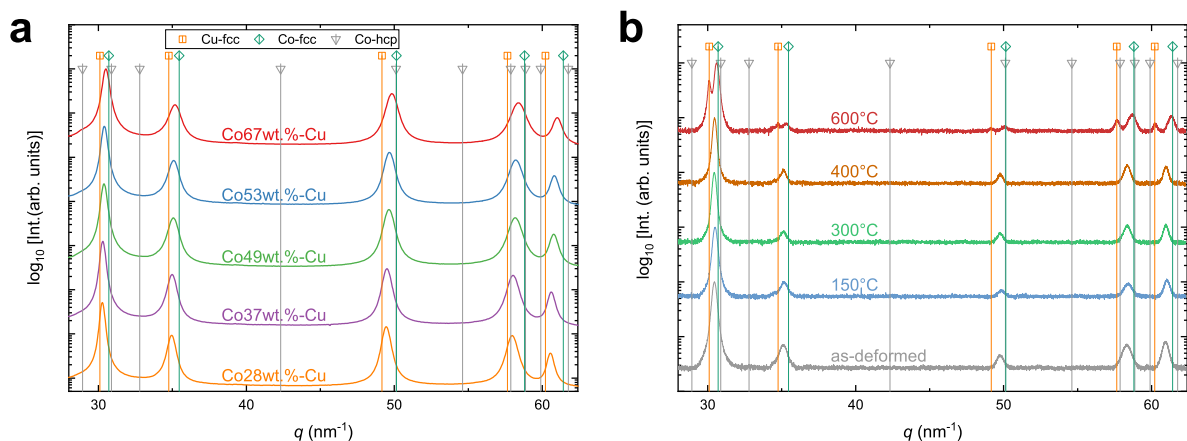


Figure 2.6.: XRD-patterns of Cu-Co HPT-deformed samples. (a) shows synchrotron XRD patterns as a function of composition, measured in transmission mode at 100 keV. (b) shows Co72wt.%-Cu in as-deformed and annealed states, measured in reflection mode with Co-K α radiation. The legend in (a) applies to (b) as well.

2.2. Towards soft magnetic tunability in Co-Cu

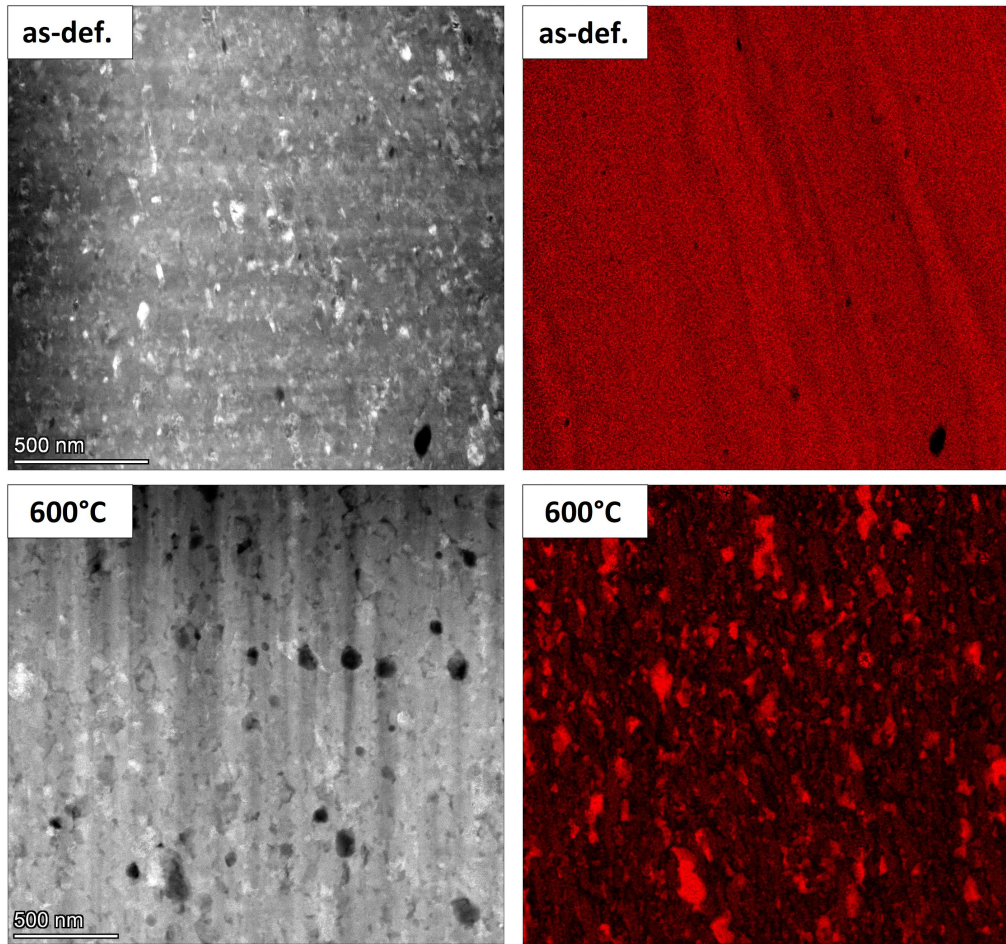


Figure 2.7.: HAADF-TEM micrographs of Co72wt.%-Cu in as-deformed state and 600°C-annealed state (left). On the right, the corresponding EDS maps show the Cu-distribution.

thermal stability are conducted on this sample. The XRD-patterns (fig. 2.6(b)) show the single-phase microstructure to be stable up to 400°C. At 600°C, two fcc-patterns are visible. TEM micrographs in high-angle annular dark-field (HAADF)-mode reveal the evolution of grain size and chemical homogeneity and are taken of the as-deformed and 600°C annealed state (fig. 2.7). Only small changes in grain size are visible upon annealing but the distribution of Cu, as shown in the energy dispersive X-ray spectroscopy (EDS) maps, changes from a homogeneous appearance in the as-deformed state, to the formation of Cu-rich regions at 600°C, corresponding to the XRD-pattern in fig. 2.6(b).

Hysteresis measurements reveal a ferromagnetic behavior for all compositions investigated, as can be seen in fig. 2.8(a). Slopes in the high-field regime of Co28wt.%-Cu and Co37wt.%-Cu indicate a partial break-down in long-range ordering and therefore the presence of small

2. Results and discussion

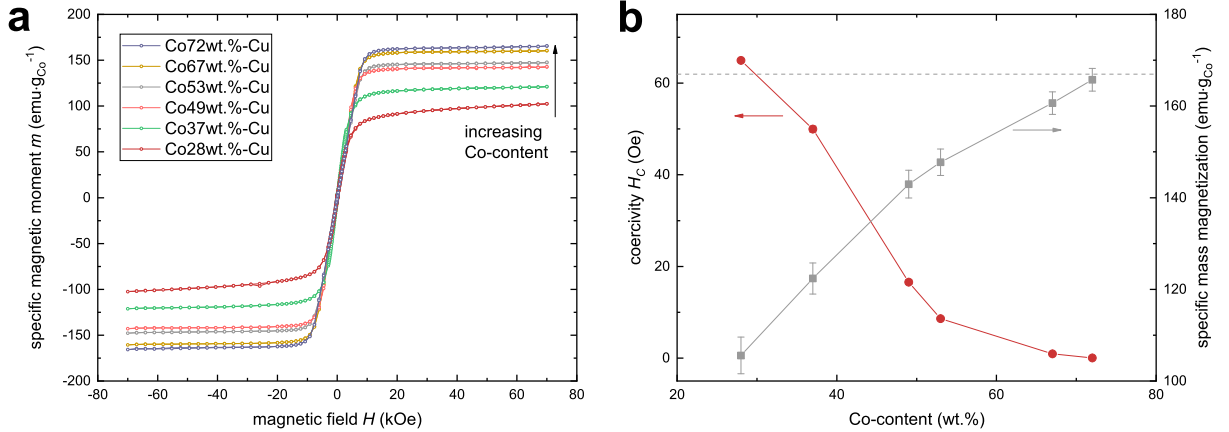


Figure 2.8.: Specific magnetic moment m as a function of applied field H measured at 300 K for various compositions of Co-Cu (a). In (b) the evaluated coercivity H_C and the saturation magnetic moment m_{SAT} are plotted as a function of Co-content. The dashed line in (b) represents the saturation magnetic moment of fcc-Co= 166.1 emu.g^{-1} .

amounts of paramagnetic Co. The specific magnetic moment deviates from the bulk magnetic moment of Co, which is typical for the formation of solid solutions [56], but attains the magnetic moment of fcc-Co for Co72wt.-%-Cu. The coercivity H_C , as evaluated from hysteresis loops diminishes as the Co-content increases, which can be seen in fig. 2.8(b). The results show that soft magnetic properties can be induced in mixtures of Co-Cu by HPT and enhanced properties can be observed as the Co-content increases.

The magnetocrystalline anisotropy is a material parameter closely related to the coercivity. Hcp-Co exhibits a large magnetocrystalline anisotropy, causing hard magnetic behavior for single-domain Co [57]. Upon phase transformation to fcc-Co, the magnetocrystalline anisotropy is expected to decrease [58], causing a magnetic softening. As shown above, all Co-Cu samples exhibit nanocrystalline microstructures in the as-deformed state, pointing at a further lowering in the magnetocrystalline anisotropy due to random anisotropy [6]. Despite, a quantitative description of the measured, low, coercivity fails, even when both parameters are taken into account. Since the microstructure does not show isolated fcc-Co particles in a Cu-matrix, as a description by random anisotropy would suggest, a contribution from alloying, namely due to formation of supersaturated solid solution is conceivable.

For further analysis of the magnetic properties, the domain structure is investigated, which is conducted by MFM for Co72wt.-%-Cu. The as-deformed state and annealed states are measured to investigate the evolution of domain structure upon annealing, i.e., demixing. Quantitative analysis of the scans is performed as shown in sec. 1.4.2, revealing a lowering

2.3. Superior soft magnetic properties in Cu-Fe-Co alloys

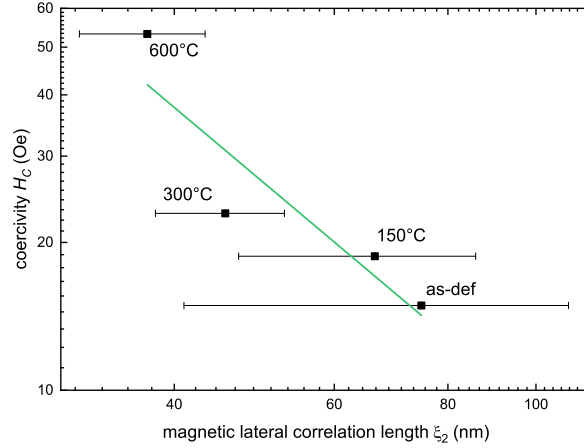


Figure 2.9.: Coercivity H_C determined from SQUID-magnetometry as a function of magnetic lateral correlation length ξ from MFM for different annealing treatments. The line is a guide to the eyes. Reproduced under the terms of the CC-BY 4.0 license. [61] © 2020, Elsevier.

in the lateral correlation length ξ with increasing annealing temperature. When putting ξ into relation with H_C as measured with SQUID-magnetometry, a magnetic hardening effect upon annealing is visible, as shown in fig. 2.9. Since the as-deformed state exhibits a single-phase supersaturated solid solution, as shown above, the diminishing ξ is likely to arise from demixing processes, as for instance spinodal decomposition [59, 60], causing the Co-atoms to agglomerate. The Co-rich regions grow upon annealing and attain the bulk magnetic properties of Co. The 600°C annealed state exhibits the smallest ξ with the highest H_C . The study on MFM is covered in further detail Paper D.

For solid solutions of Cu-Co both, the magnetic moment and the coercivity is controlled by the Cu-to-Co ratio. The materials investigated show soft magnetic properties, which are enhanced by larger Co-contents. A further improvement of soft magnetic properties is limited by the relatively large magnetocrystalline anisotropy of Co.

2.3. Superior soft magnetic properties in Cu-Fe-Co alloys

As shown above, Cu-Co samples form supersaturated solid solutions with soft magnetic properties upon HPT-processing. Since Fe-Co alloys exhibit smaller magnetocrystalline anisotropies as well as higher magnetic moment, further improvement towards superior soft magnetic properties can be made by addition of Fe [62].

2. Results and discussion

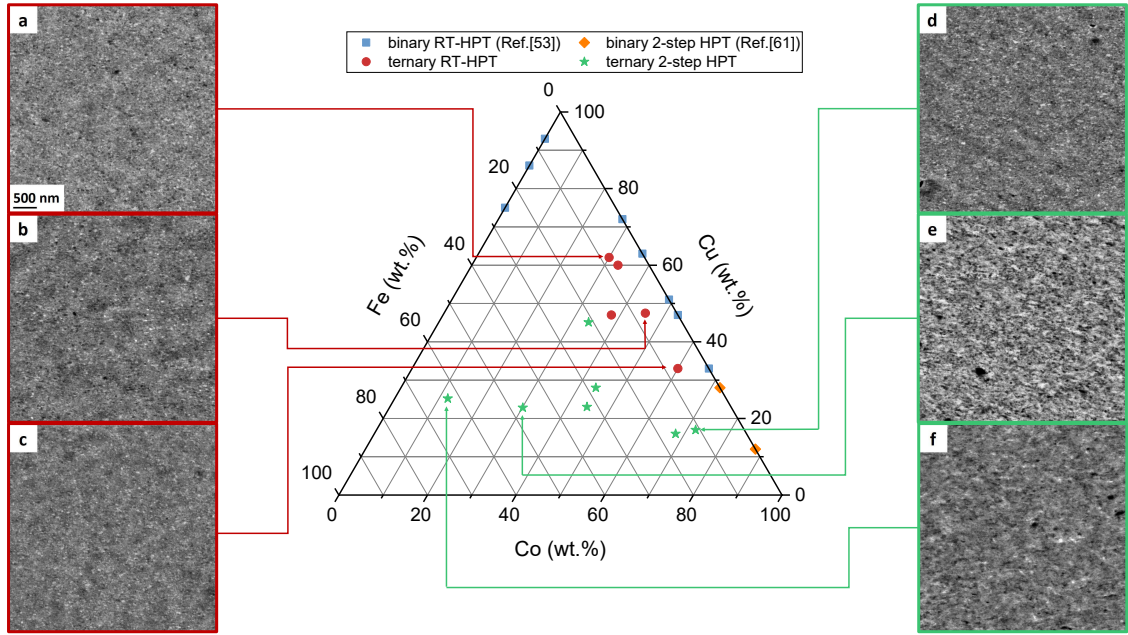


Figure 2.10.: SEM micrographs of as-deformed samples with ternary compositions. The diagram in the middle shows the compositions investigated in comparison to binary compositions from above (Fe-Cu, Co-Cu). Images on the left (a)-(c) show samples processed by RT deformation. Images on the right (d)-(f) shows samples processed by 2-step HPT deformation. The scale bar in (a) applies to all micrographs.

Similarly to binary Co-Cu samples, HPT-deformation at RT yields a homogeneous deformation only for intermediate Co or Fe concentrations. For higher concentrations of the ferromagnetic phase, the 2-step deformation process, as described above, is employed. In fig. 2.10 SEM micrographs of various compositions, processed either by RT deformation (red dots) or 2-step deformation (green stars), are shown. To investigate the influence of various ratios of Co and Fe a constant ferromagnetic content is maintained, i.e. the Cu-content remains at about 20wt.% for various Fe-to-Co-ratios. The addition of high amounts of Fe (≥ 20 wt.%) leads to the formation of a compound consisting of two crystalline phases, namely an fcc-phase and a bcc-phase. Hysteresis measurement of an Fe-rich sample, consisting of $\text{Cu}_{25}\text{Fe}_{63}\text{Co}_{12}$, reveal a rather high coercivity of ≈ 40 Oe. Furthermore, an enhanced saturation magnetic moment is measured, showing the formation of an Fe-Co alloy, corresponding to results from XRD-measurements.

For Co-rich ternary compositions, single-phase supersaturated solid solutions form upon HPT-deformation, as in the case for binary Co-Cu samples. Investigations on the magnetic properties of $\text{Cu}_{17}\text{Fe}_{11}\text{Co}_{72}$ (wt.%) show a magnetic moment, which equals the sum of Fe and Co magnetic moments. This result demonstrates that no Fe-Co alloys form, as an Fe-Co

2.3. Superior soft magnetic properties in Cu-Fe-Co alloys

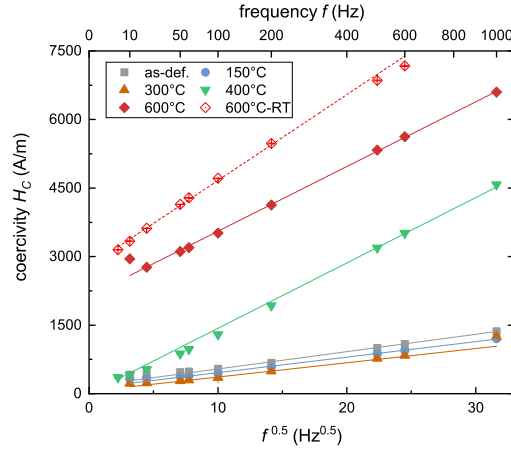


Figure 2.11.: Evolution of coercivity of $\text{Cu}_{17}\text{Fe}_{11}\text{Co}_{72}$ versus frequency for various in-situ annealing treatments.

alloys would exhibit a higher magnetic moment. The coercivity of this composition cannot be properly resolved by SQUID-magnetometry, as the coercivity is smaller than the remanent field of the superconducting magnet [63, 64]. Instead, the coercivity is determined by means of AC-hysteresis measurements. For this purpose a ring core is fabricated. The frequency dependent evolution of the hysteresis provides insights into the dynamic contributions of losses (arising from domain wall motion and eddy currents) [49–52]. Furthermore, the static coercivity can be approximated by extrapolating the dynamic loss curve towards zero frequency, which is determined to 162 A/m in the as-deformed state. Eddy current losses scale with conductivity. Since HPT-processed materials exhibit high densities of lattice defects the conductivity is significantly lowered [65] and eddy current losses can be neglected. Instead, the dynamic behavior is found to arise to a major extend from a low mobility of domain wall motion. To investigate the evolution of magnetic properties upon annealing the hysteresis is measured in-situ during thermal treatment. Fig. 2.11 shows the dynamic behavior for the in-situ annealing treatments, as investigated in paper F. Up to 400°C, a decreasing coercivity is measured, arising from temperature dependence of the magnetocrystalline anisotropy [66], but might also arise from stress relief [67]. At 600°C, a large increase in coercivity is measured, corresponding to the decomposition of the single-phase supersaturated solid solution and the formation of a compound with significantly larger grain size. The dynamic loss parameter b shows a huge increase at 400°C, preceding the increasing coercivity at 600°C. This behavior indicates the formation of pinning centres, such as precipitates, hindering the motion of domain walls. Ex-situ experiments on the microstructure reveal a persisting

2. Results and discussion

single-phase crystallographic configuration up to 400°C. It should be stated that pinning centres which have precipitated have not been resolved by SEM or XRD. However, the evolution of hardness as a function of annealing temperatures peaks at 400°C which might arise from a formation of tiny precipitates. At 600°C a compound consisting of three phases, according to the thermodynamical equilibrium, is present. The in-situ study is covered in detail in paper F.

The results demonstrate a significant enhancement in soft magnetic properties with respect to Co-Cu samples by adding small amounts of Fe. XRD- and SEM-investigations on the thermal stability show a persisting single-phase microstructure up to 400°C. At 600°C, decomposition into the stable phases according to the thermodynamical equilibrium is observed.

2.4. Magnetic properties in Ag-based materials systems

In the Fe-Ag systems, a strong localization of deformation is observed for high Fe-contents. Low Fe-contents (≤ 30 wt.%) in contrast, show a homogeneous deformation and grain refinement (fig. 2.12(a)) for Fe and Ag with respect to the grain size of the initial powders. In SEM-backscattered electrons (BSE) images, a high phase contrast is visible, indicating a poor grade of intermixing. Hysteresis measurements, reveal a typical bulk Fe hysteresis loop (fig. 2.13), pointing again out, that the Ag-phase and the Fe-phase did not mix during deformation (see Paper A for more details).

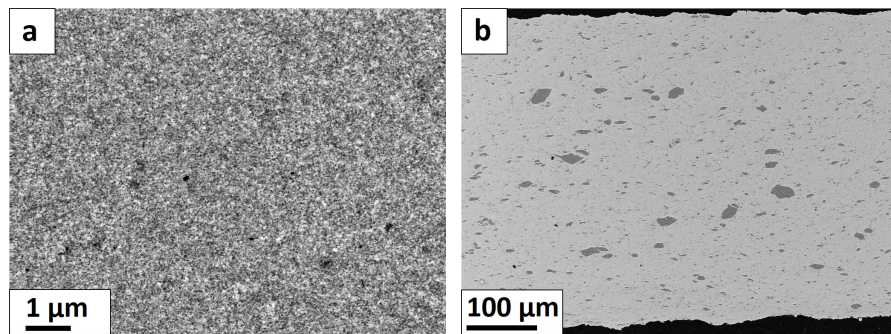


Figure 2.12.: SEM-BSE micrographs for Fe30wt.%-Ag (a) at an equivalent strain of $\gamma \approx 3000$ and Co20wt.%-Ag (b) at an equivalent strain of $\gamma \approx 6000$. Note the different scale bars.

In the Co-Ag system also strong localization during deformation can be observed for high Co-contents. For small Co-contents, deformation leads to grain refinement only in the

2.4. Magnetic properties in Ag-based materials systems

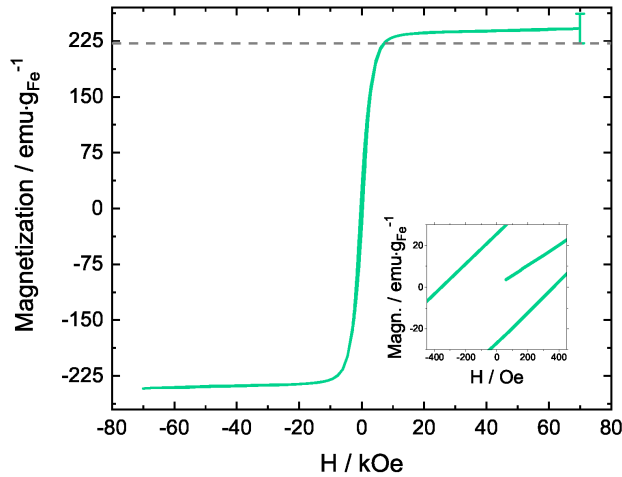


Figure 2.13.: Hysteresis of Fe18wt.%-Ag measured with SQUID at 300 K. The dashed line represents the saturation magnetic moment of bulk Fe $218 \text{ emu}\cdot\text{g}^{-1}$. The inset shows a coercivity of 400 Oe. Reproduced under the terms of the CC-BY 4.0 license. [53] © 2020, MDPI.

Ag-phase. Shape and grain size of the Co-particles do not change during deformation as can be seen in fig. 2.12(b). The lack of deformation in the Co-particles is expected to arise from the large difference in plastic deformation behavior of both, the Ag- and the Co-powder [22]. Since no intermixing could be achieved for any composition in the Co-Ag systems, the magnetic properties have not been investigated, but are expected to show no deviation with respect to the ferromagnetic behavior of the initial powder.

In comparison to the Cu-based systems shown above, the Ag-based systems have found to be rigid to the formation of solid solutions by HPT. As has been described in [22], the intermixing upon HPT depends to a major extend on the mechanical properties, in particular plastic properties, of the used materials. Since the Ag exhibits a much smaller hardness than the Fe or Co phase, the soft Ag-phase is deformed stronger than the Fe or Co phases. On the other hand, Fe exhibits a smaller hardness than Co, explaining the grain refinement of Fe particles. In the Co-Ag alloys, fragmentation of Co-particles can be observed only to a small extend.

3. Summary and Outlook

This study demonstrates the capability of SPD by HPT in producing bulk materials with functional properties. The initial multi phase materials form nanocrystalline microstructures upon processing. Several material systems have been investigated in this study, whereby the magnetic properties are traced back to the microstructure. In case of the Fe-Cu system, a spin-glass state is formed upon deformation, where the amount of the spin-glass phase is controlled by the composition, caused by the formation of a supersaturated solid solution. Larger Fe-contents favor the formation of superparamagnetic Fe-particles. Furthermore, with subsequent annealing treatments, demixing is triggered, leading to the formation or growth of Fe-particles, exhibiting magnetic single-phase and for higher temperatures even multi-phase behavior.

In case of Co-Cu solid solutions, tunability in the magnetic moment and the coercivity has been observed, which was achieved by varying the Co-to-Cu ratio. The alloys form homogeneous supersaturated solid solutions. Soft magnetic properties have been observed for high Co-contents. A further improvement of the soft magnetic properties was achieved by substituting small amounts of Co with Fe. With too large Fe-contents the magnetic properties change to a hard magnetic behavior, arising from a different deformation characteristic.

Although wide compositional ranges have been investigated in the Co-Cu and the Cu-Fe-Co systems, the processing is limited by the characteristics of the initial phases. In particular, mechanical properties are assumed to be responsible for the limits in processability. For this reason, in the Fe-Ag system no intermixing has been observed. In case of the Co-Ag system fragmentation of the mechanically harder Co-particles is observed to a very small extend, whereat the majority of the deformation is restricted to the mechanically soft Ag-phase.

Moreover, in this study it has been demonstrated that by combining microstructural with magnetic measurement techniques an in-depth analysis of the microstructural assembly can be worked out, since even smallest changes in the atomic arrangement cause changes in the magnetic properties. A correlation of both techniques can be therefore used in the development of an holistic understanding of the microstructure, which would be utterly

3. *Summary and Outlook*

impossible by using solely microstructural investigation techniques.

Further improvements in terms of soft magnetic properties of HPT-processed materials can be achieved by reducing the grain size even further. One possibility to diminish the grain size is the usage of an additional step of HPT-deformation: since the grain size in HPT-deformed materials depends on the deformation temperature, a subsequent deformation step at lower temperatures is expected to lead to enhanced soft magnetic properties. Another approach to achieve smaller grain sizes includes the synthesis of initial powders. It has been reported that powder preparation by inert-gas condensation or microwave plasma synthesis is capable of producing powders with grain sizes in the range of several nanometers [13, 68, 69]. A fully dense and bulky specimen can then be produced by means of HPT.

To push the boundaries in terms of coercivity, the ultimate goal is the formation of an amorphous microstructure by HPT. In this context, combinations of materials have to be used, which enable the formation of bulk metallic glasses. Research on mechanical alloying has already demonstrated the formation of amorphous microstructures in a large variety of systems, e.g. in mixtures of transition metals with Zr and Ti [70–74]. An amorphization by HPT-deformation has also been already observed for certain compositions [75], although very limited literature is available on this topic.

4. Bibliography

- [1] A. Hubert and R. Schäfer. *Magnetic domains: the analysis of magnetic microstructures*. Springer Science & Business Media, 2008.
- [2] B.D. Cullity and C.D. Graham. *Introduction to magnetic materials*. John Wiley & Sons, 2011.
- [3] R. Gross and A. Marx. *Festkörperphysik*. Walter de Gruyter GmbH & Co KG, 2018.
- [4] R. Alben, J.J. Becker, and M.C. Chi. “Random anisotropy in amorphous ferromagnets”. In: *J. Appl. Phys.* 49.3 (1978), pp. 1653–1658. DOI: 10.1063/1.324881.
- [5] K. Suzuki et al. “Soft magnetic properties of nanocrystalline bcc Fe-Zr-B and Fe-M-B-Cu (M = transition metal) alloys with high saturation magnetization”. In: *J. Appl. Phys.* 70.10 (1991), pp. 6232–6237. DOI: 10.1063/1.350006.
- [6] G. Herzer. “Soft magnetic nanocrystalline materials”. In: *Scr. Mater.* 33.10-11 (1995), pp. 1741–1756. DOI: 10.1016/0956-716X(95)00397-E.
- [7] C.P. Bean and J.D. Livingston. “Superparamagnetism”. In: *J. Appl. Phys.* 30.4 (1959), S120–S129. DOI: 10.1063/1.2185850.
- [8] W.C. Nunes et al. “Temperature dependence of the coercive field in single-domain particle systems”. In: *Phys. Rev. B* 70 (1 2004), p. 014419. DOI: 10.1103/PhysRevB.70.014419.
- [9] G. Herzer. “Modern soft magnets: Amorphous and nanocrystalline materials”. In: *Acta Mater.* 61.3 (2013). The Diamond Jubilee Issue, pp. 718–734. DOI: 10.1016/j.actamat.2012.10.040.
- [10] O. Gutfleisch et al. “Magnetic Materials and Devices for the 21st Century: Stronger, Lighter, and More Energy Efficient”. In: *Adv. Mater.* 23.7 (2011), pp. 821–842. DOI: 10.1002/adma.201002180.
- [11] J.H. Kang et al. “An extracorporeal blood-cleansing device for sepsis therapy”. In: *Nat. Med.* 20.10 (2014), pp. 1211–1216. DOI: 10.1038/nm.3640.
- [12] R.Z. Valiev, R.K. Islamgaliev, and I.V. Alexandrov. “Bulk nanostructured materials from severe plastic deformation”. In: *Prog. Mater. Sci.* 45.2 (2000), pp. 103–189. DOI: 10.1016/S0079-6425(99)00007-9.
- [13] H. Gleiter. “Nanocrystalline materials”. In: *Prog. Mater. Sci.* 33.4 (1989), pp. 223–315. DOI: 10.1016/0079-6425(89)90001-7.

4. Bibliography

- [14] B.B. Straumal et al. “Effect of severe plastic deformation on the coercivity of Co–Cu alloys”. In: *Philos. Mag. Lett.* 89.10 (2009), pp. 649–654. DOI: 10.1080/09500830903246268.
- [15] S. Scheriau et al. “Magnetic characteristics of HPT deformed soft-magnetic materials”. In: *J. Magn. Magn. Mater.* 322.20 (2010), pp. 2984–2988. DOI: 10.1016/j.jmmm.2010.04.032.
- [16] K. Edalati et al. “High-pressure torsion of pure cobalt: hcp-fcc phase transformations and twinning during severe plastic deformation”. In: *Appl. Phys. Lett.* 102.18 (2013), p. 181902. DOI: 10.1063/1.4804273.
- [17] A. Bachmaier et al. “Tailoring the magnetic properties of nanocrystalline Cu-Co alloys prepared by high-pressure torsion and isothermal annealing”. In: *J. Alloys Comps.* 725 (2017), pp. 744–749. DOI: 10.1016/j.jallcom.2017.07.200.
- [18] P.W. Bridgman. “Effects of High Shearing Stress Combined with High Hydrostatic Pressure”. In: *Phys. Rev.* 48 (10 1935), pp. 825–847. DOI: 10.1103/PhysRev.48.825.
- [19] K. Edalati and Z. Horita. “A review on high-pressure torsion (HPT) from 1935 to 1988”. In: *Mater. Sci. Eng. A* 652 (2016), pp. 325–352. DOI: 10.1016/j.msea.2015.11.074.
- [20] K. Edalati and Z. Horita. “High-pressure torsion of pure metals: Influence of atomic bond parameters and stacking fault energy on grain size and correlation with hardness”. In: *Acta Mater.* 59.17 (2011), pp. 6831–6836. DOI: 10.1016/j.actamat.2011.07.046.
- [21] R. Pippan et al. “Saturation of fragmentation during severe plastic deformation”. In: *Annu. Rev. Mater. Sci.* 40 (2010), pp. 319–343. DOI: 10.1146/annurev-matsci-070909-104445.
- [22] K.S. Kormout, R. Pippan, and A. Bachmaier. “Deformation-induced supersaturation in immiscible material systems during high-pressure torsion”. In: *Adv. Eng. Mater.* 19.4 (2017), p. 1600675. DOI: 10.1002/adem.201600675.
- [23] A. Bachmaier et al. “On the process of co-deformation and phase dissolution in a hard-soft immiscible CuCo alloy system during high-pressure torsion deformation”. In: *Acta Mater.* 115 (2016), pp. 333–346. DOI: 10.1016/j.actamat.2016.06.010.
- [24] R. Pippan et al. “The limits of refinement by severe plastic deformation”. In: *Adv. Eng. Mater.* 8.11 (2006), pp. 1046–1056. DOI: 10.1002/adem.200600133.
- [25] O. Renk and R. Pippan. “Saturation of Grain Refinement during Severe Plastic Deformation of Single Phase Materials: Reconsiderations, Current Status and Open Questions”. In: *Mater. Trans.* 60.7 (2019), pp. 1270–1282. DOI: 10.2320/matertrans.MF201918.
- [26] B. Gault et al. *Atom probe microscopy*. Vol. 160. Springer Science & Business Media, 2012.
- [27] M. Herbig, P. Choi, and D. Raabe. “Combining structural and chemical information at the nanometer scale by correlative transmission electron microscopy and atom probe tomography”. In: *Ultramicroscopy* 153 (2015), pp. 32–39. DOI: 10.1016/j.ultramicro.2015.02.003.

- [28] B. Gault et al. “Spatial Resolution in Atom Probe Tomography”. In: *Microsc. Microanal.* 16.1 (2010), pp. 99–110. DOI: 10.1017/S1431927609991267.
- [29] E. A. Marquis and F. Vurpillot. “Chromatic aberrations in the field evaporation behavior of small precipitates”. In: *Microsc. Microanal.* 14.6 (2008), p. 561. DOI: 10.1017/S1431927608080793.
- [30] P. Felfer et al. “Detecting and extracting clusters in atom probe data: A simple, automated method using Voronoi cells”. In: *Ultramicroscopy* 150 (2015), pp. 30–36. DOI: 10.1016/j.ultramicro.2014.11.015.
- [31] F. De Geuser and W. Lefebvre. “Determination of matrix composition based on solute-solute nearest-neighbor distances in atom probe tomography”. In: *Microsc. Res. Tech.* 74.3 (2011), pp. 257–263. DOI: 10.1002/jemt.20899.
- [32] H. Zhao et al. “Parameter free quantitative analysis of atom probe data by correlation functions: Application to the precipitation in Al-Zn-Mg-Cu”. In: *Scripta Mater.* 154 (2018), pp. 106–110. DOI: 10.1016/j.scriptamat.2018.05.024.
- [33] F. De Geuser and B. Gault. “Metrology of small particles and solute clusters by atom probe tomography”. In: *Acta Mater.* 188 (2020), pp. 406–415. DOI: 10.1016/j.actamat.2020.02.023.
- [34] O. Kazakova et al. “Frontiers of magnetic force microscopy”. In: *J. Appl. Phys.* 125.6 (2019), p. 060901. DOI: 10.1063/1.5050712.
- [35] M.R. Koblischka, U. Hartmann, and T. Sulzbach. “Resolving magnetic nanostructures in the 10-nm range using MFM at ambient conditions”. In: *Mater. Sci. Eng. C* 23.6-8 (2003), pp. 747–751. DOI: 10.1016/j.msec.2003.09.146.
- [36] C. Teichert et al. “Comparison of surface roughness of polished silicon wafers measured by light scattering topography, soft-x-ray scattering, and atomic-force microscopy”. In: *Appl. Phys. Lett.* 66.18 (1995), pp. 2346–2348. DOI: 10.1063/1.113978.
- [37] C. Teichert. “Self-organization of nanostructures in semiconductor heteroepitaxy”. In: *Phys. Rep.* 365.5 (2002), pp. 335–432. DOI: 10.1016/S0370-1573(02)00009-1.
- [38] J.F. MacKay et al. “Element specific magnetization of buried interfaces probed by diffuse x-ray resonant magnetic scattering”. In: *Phys. Rev. Lett.* 77.18 (1996), p. 3925. DOI: 10.1103/PhysRevLett.77.3925.
- [39] C. Teichert, J.J. De Miguel, and T. Bobek. “Ion beam sputtered nanostructured semiconductor surfaces as templates for nanomagnet arrays”. In: *J. Phys. Condens. Matter* 21.22 (2009), p. 224025. DOI: 10.1088/0953-8984/21/22/224025.
- [40] Y. Zhao, G.-C. Wang, and T.-M. Lu. *Characterization of Amorphous and Crystalline Rough Surface—Principles and Applications*. Elsevier, 2000.

4. Bibliography

- [41] M. McElfresh. “Fundamentals of magnetism and magnetic measurements featuring Quantum Design’s magnetic property measurement system”. In: *Quantum Design* 11578 (1994), p. 132.
- [42] J. Clarke and A.I. Braginski. “The SQUID handbook. Vol. 2. Applications of SQUIDs and SQUID systems”. In: (2006).
- [43] M. Knobel et al. “Superparamagnetism and other magnetic features in granular materials: a review on ideal and real systems”. In: *J. Nanosci. Nanotechnology* 8.6 (2008), pp. 2836–2857. DOI: 10.1166/jnn.2008.15348.
- [44] K. Binder and A.P. Young. “Spin glasses: Experimental facts, theoretical concepts, and open questions”. In: *Rev. Mod. Phys.* 58.4 (1986), p. 801. DOI: 10.1103/RevModPhys.58.801.
- [45] T. Nishizaki et al. “Superconducting properties in bulk nanostructured niobium prepared by high-pressure torsion”. In: *Physica C Supercond.* 493 (2013), pp. 132–135. DOI: 10.1016/j.physc.2013.03.046.
- [46] M. Göbller et al. “Magneto-Ionic Switching of Superparamagnetism”. In: *Small* 15.46 (2019), p. 1904523. DOI: 10.1002/smll.201904523.
- [47] S. Hartl. “Magnetic Properties of deformed Electrical Steel”. MA thesis. Technische Universität Wien, 2014.
- [48] R.S. Turtelli et al. “Hysteresis and Loss Measurements on the Plastically Deformed Fe–(3 wt%) Si Under Sinusoidal and Triangular External Field”. In: *IEEE Trans. Magn.* 52.5 (2016), pp. 1–7. DOI: 10.1109/TMAG.2016.2530683.
- [49] G. Bertotti, F. Fiorillo, and G.P. Soardo. “The prediction of power losses in soft magnetic materials”. In: *J. Phys. Colloq.* 49.C8 (1988), pp. C8–1915. DOI: 10.1051/jphyscol:19888867.
- [50] F. Fiorillo. *Measurement and characterization of magnetic materials*. North-Holland, 2004.
- [51] R. Hilzinger and W. Rodewald. *Magnetic materials: fundamentals, products, properties, applications*. Vacuumschmelze, 2013.
- [52] F. Fiorillo et al. *Soft Magnetic Materials*. Webster, J.G., 2016. DOI: 10.1002/047134608X.W4504.pub2.
- [53] M. Stückler et al. “Magnetic Binary Supersaturated Solid Solutions Processed by Severe Plastic Deformation”. In: *Nanomaterials* 9.1 (2018), p. 6. DOI: 10.3390/nano9010006.
- [54] M. Stückler et al. “Intermixing of Fe and Cu on the atomic scale by high-pressure torsion as revealed by DC-and AC-SQUID susceptometry and atom probe tomography”. In: *Acta Mater.* 196 (2020), pp. 210–219. DOI: 10.1016/j.actamat.2020.06.035.
- [55] T. Ungár and G. Tichy. “The effect of dislocation contrast on X-ray line profiles in untextured polycrystals”. In: *Phys. Status Solidi A* 171.2 (1999), pp. 425–434. DOI: 10.1002/(SICI)1521-396X(199902)171:2<425::AID-PSSA425>3.0.CO;2-W.

- [56] J.R. Childress and C.L. Chien. “Reentrant magnetic behavior in fcc Co-Cu alloys”. In: *Phys. Rev. B* 43.10 (1991), p. 8089. DOI: 10.1103/PhysRevB.43.8089.
- [57] H. Kronmüller and M. Fähnle. *Micromagnetism and the microstructure of ferromagnetic solids*. Cambridge University Press, 2003.
- [58] J.P. Chen et al. “Magnetic properties of nanophase cobalt particles synthesized in inversed micelles”. In: *J. Appl. Phys.* 76.10 (1994), pp. 6316–6318. DOI: 10.1063/1.358280.
- [59] A. Hütten and G. Thomas. “Investigation of heterogeneous $\text{Cu}_{1-x}\text{Co}_x$ alloys with giant magnetoresistance”. In: *Ultramicroscopy* 52.3-4 (1993), pp. 581–590. DOI: 10.1016/0304-3991(93)90077-B.
- [60] A. Bachmaier et al. “Phase separation of a supersaturated nanocrystalline Cu-Co alloy and its influence on thermal stability”. In: *Acta Mater.* 96 (2015), pp. 269–283. DOI: 10.1016/j.actamat.2015.05.0530.
- [61] M. Stückler et al. “On the magnetic nanostructure of a Co-Cu alloy processed by high-pressure torsion”. In: *J. Sci. Adv. Mater. Dev.* (2020). in press. DOI: 10.1016/j.jsamd.2020.09.013.
- [62] C. Kuhrt and L. Schultz. “Formation and magnetic properties of nanocrystalline mechanically alloyed Fe-Co”. In: *J. Appl. Phys.* 71.4 (1992), pp. 1896–1900. DOI: 10.1063/1.351177.
- [63] *Application Note 1500-011*. Rev. A0. Quantum Design, San Diego, California. 2010.
- [64] M. Buchner et al. “Tutorial: Basic principles, limits of detection, and pitfalls of highly sensitive SQUID magnetometry for nanomagnetism and spintronics”. In: *J. Appl. Phys.* 124.16 (2018), p. 161101. DOI: 10.1063/1.5045299.
- [65] J.M. Cubero-Sesin, M. Arita, and Z. Horita. “High Strength and Electrical Conductivity of Al-Fe Alloys Produced by Synergistic Combination of High-Pressure Torsion and Aging”. In: *Adv. Eng. Mater.* 17.12 (2015), pp. 1792–1803. DOI: 10.1002/adem.201500103.
- [66] N.L. Brukhatov and L.V. Kirensky. “The anisotropy of the magnetic energy in single crystals of Nickel as a function of temperature”. In: *Phys. Z. Sowjetunion* 12.5 (1937), p. 601.
- [67] T.D. Shen, R.B. Schwarz, and J.D. Thompson. “Soft magnetism in mechanically alloyed nanocrystalline materials”. In: *Phys. Rev. B* 72.1 (2005), p. 014431. DOI: 10.1103/PhysRevB.72.014431.
- [68] U. Brossmann et al. “Oxygen diffusion in ultrafine grained monoclinic ZrO_2 ”. In: *J. Appl. Phys.* 85.11 (1999), pp. 7646–7654. DOI: 10.1063/1.370567.
- [69] D. Vollath and D.V. Szabo. “The Microwave plasma process—a versatile process to synthesise nanoparticulate materials”. In: *J. Nanoparticle Res.* 8.3-4 (2006), pp. 417–428. DOI: 10.1007/s11051-005-9014-0.

4. Bibliography

- [70] B.P. Dolgin et al. “Mechanical alloying of Ni, Co, and Fe with Ti. Formation of an amorphous phase”. In: *J. Non Cryst. Solids* 87.3 (1986), pp. 281–289. DOI: 10.1016/S0022-3093(86)80002-3.
- [71] E. Hellstern and L. Schultz. “Glass formation in mechanically alloyed transition metal-titanium alloys”. In: *Mater. Sci. Eng.* 93 (1987), pp. 213–216. DOI: 10.1016/0025-5416(87)90426-5.
- [72] E. Hellstern and L. Schultz. “Glass formation in mechanically alloyed transition-metal-Zr alloys”. In: *Philos. Mag. B* 56.4 (1987), pp. 443–448. DOI: 10.1080/13642818708221330.
- [73] E. Hellstern, L. Schultz, and J. Eckert. “Glass-forming ranges of mechanically alloyed powders”. In: *J. Less Common Met.* 140 (1988), pp. 93–98. DOI: 10.1016/0022-5088(88)90371-2.
- [74] M. Sherif El-Eskandarany et al. “Cyclic crystalline–amorphous transformations of mechanically alloyed Co 75 Ti 25”. In: *Appl. Phys. Lett.* 70.13 (1997), pp. 1679–1681. DOI: 10.1063/1.118667.
- [75] A.M. Glezer, R.V. Sundeev, and A.V. Shalimova. “Phase transformations \ll amorphization \Leftrightarrow crystallization \gg in metallic materials by severe plastic deformation”. In: *Rev. Adv. Mater. Sci.* 54.1 (2018). DOI: 10.1515/rams-2018-0021.

5. List of appended publications and proceedings

In the framework of the present doctoral thesis, the following peer-reviewed manuscripts have been prepared. The doctoral candidate has performed all experiments, data analysis and interpretation as well as writing of the manuscripts, with some exceptions given below.

- Paper A: **Magnetic binary supersaturated solid solutions processed by severe plastic deformation**

M. Stückler, H. Krenn, R. Pippan, L. Weissitsch, S. Wurster and A. Bachmaier
Nanomaterials **9** (2018). doi: 10.3390/nano9010006

K. Kormout conducted the synchrotron XRD measurements. TKD experiments were performed and analyzed by S. Wurster.

- Paper B: **Magnetic dilution by severe plastic deformation**

M. Stückler, L. Weissitsch, S. Wurster, P. Felfer, H. Krenn, R. Pippan, and A. Bachmaier
AIP Advances **10** 015210 (2020). doi: 10.1063/1.5128058

APT experiments were conducted by A. Bachmaier and P. Felfer. The respective reconstructions were processed by P. Felfer. S. Wurster created the electron backscatter diffraction (EBSD) scan.

- Paper C: **Intermixing of Fe and Cu on the atomic scale by high-pressure torsion as revealed by DC- and AC-SQUID susceptometry and atom probe tomography**

M. Stückler, H. Krenn, P. Kürsteiner, B. Gault, F. De Geuser, L. Weissitsch, S. Wurster, R. Pippan, and A. Bachmaier
Acta Materialia **196** 210-219 (2020). doi: 10.1016/j.actamat.2020.06.035

APT experiments were conducted by P. Kürsteiner who also built the APT reconstructions. Analysis of the reconstructed volume was performed by B. Gault and F. De Geuser.

5. List of appended publications and proceedings

- Paper D: **On the magnetic nanostructure of a Co-Cu alloy processed by high-pressure torsion**
M. Stücker, C. Teichert, A. Matković, H. Krenn, L. Weissitsch, S. Wurster, R. Pippan and A. Bachmaier
Journal of Science: Advanced Materials and Devices (2020) in press
doi: 10.1016/j.jsamd.2020.09.013

C. Teichert and A. Matković contributed to analyzing the AFM and MFM data.
- Paper E: **Formation of supersaturated solid solutions of Cu-Fe-Co by severe plastic deformation**
M. Stücker, L. Weissitsch, S. Wurster, H. Krenn, R. Pippan, A. Bachmaier
Journal of Alloys and Compounds submitted

Sample preparation by HPT was performed by M. Kasalo in parts. A. Paulischin provided several hardness values for the ternary hardness diagram .
- Paper F: **In-situ AC-hysteresis measurements of SPD-processed $\text{Cu}_{20}(\text{Fe}_{15}\text{Co}_{85})_{80}$**
M. Stücker, S. Wurster, R. Pippan, A. Bachmaier
AIP Advances submitted

S. Wurster contributed to the development of the experimental set-up as well as to the conduction of the in-situ experiment.

On the following pages, the manuscripts listed above are presented.

A. Magnetic Binary Supersaturated Solid Solutions Processed by Severe Plastic Deformation

Martin Stückler¹, Heinz Krenn², Reinhard Pippan¹, Lukas Weissitsch¹, Stefan Wurster¹ and Andrea Bachmaier¹

¹ *Erich Schmid Institute of Materials Science, Austrian Academy of Sciences, Jahnstraße 12, 8700 Leoben, Austria*

² *Institute of Physics, University of Graz, Universitätsplatz 5, 8010 Graz, Austria*

Abstract

Samples consisting of one ferromagnetic and one diamagnetic component which are immiscible at the thermodynamic equilibrium (Co-Cu, Fe-Cu, Fe-Ag) are processed by high-pressure torsion at various compositions. The received microstructures are investigated by electron microscopy and synchrotron X-ray diffraction, showing a microstructural saturation. Results gained from microstructural investigations are correlated to magnetometry data. The Co-Cu samples show mainly ferromagnetic behavior and a decrease in coercivity with increasing Co-content. The saturation microstructure of Fe-Cu samples is found to be dual phase. Results of magnetic measurements also revealed the occurrence of two different magnetic phases in this system. For Fe-Ag, the microstructural and magnetic results indicate that no intermixing between the elemental phases takes place.

Keywords: severe plastic deformation, high-pressure torsion, supersaturation, magnetic properties, nanocrystalline

A.1. Introduction

Creating materials with tailored functional properties has been a large field of interest for many years. In the field of magnetism, for example, it was shown that the magnetic moment of γ -Fe₂O₃ can be tuned electrochemically [1]. Another approach to create materials with tunable magnetic properties is to exploit effects of magnetic dilution. Therefore, metastable materials are fabricated, consisting of elements which exhibit large miscibility gaps in the thermodynamic equilibrium. The concept is to synthesize homogeneous structures consisting of components with different magnetic properties (e.g., ferromagnetic and diamagnetic). For instance, Chien et al. [2] processed Fe-Cu samples by the vapor quenching method or Childress et al. [3] produced Co-Cu samples by magnetron sputtering. Both approaches showed that magnetic properties can be tuned, e.g., the Curie-temperature was shifted towards smaller values for high Cu-containing compositions. Such metastable solid solutions can also be processed with ball-milling [4, 5], leading to samples in powder form. Another route to prepare such samples is with high-pressure torsion (HPT) deformation [6, 7], a severe plastic deformation (SPD) technique, which has the advantage that the resulting sample is already in bulk form. It was shown that binary supersaturated solid solutions can be processed at high homogeneity by HPT [8, 9]. The microstructure of as-deformed samples typically exhibits grain sizes in the nanocrystalline regime. First, investigations regarding magnetic tunability have been carried out on HPT-processed Co26wt.%-Cu, showing large deviations in the saturation behaviour of the as-deformed state with respect to bulk hcp-Co [10]. Further investigations revealed the sensitivity of the magnetic properties, such as coercivity and remanence, on the processing parameters as well as the influence of subsequent annealing treatments as the microstructure and elemental distribution could change.

As covered by Herzer [11], grain sizes in the nanometer regime lead to a decrease in coercivity. In this regime, the coercivity is not controlled by domain wall motion and its hindering due to obstacles like grain boundaries. Instead, the grains' random alignment of the magnetic easy axes lead to a breakdown in coercivity [12].

In this study, supersaturated solid solutions are prepared by HPT consisting of one ferromagnetic and one diamagnetic component. The microstructure of the as-deformed samples, which are already available in bulk form, are characterized and correlated to their magnetic properties.

A.2. Materials and Methods

The investigated binary compounds consist of Co-Cu, Fe-Cu or Fe-Ag. To obtain any desired chemical composition, conventional powders are used as starting materials (Fe: MaTeck 99.9% –100+200 mesh, Co: GoodFellow 99.9% 50–150 μm , Cu: AlfaAesar 99.9% –170+400 mesh, Ag: AlfaAesar 99.9% –500 mesh). An Ar-filled glovebox is used to store the powders and prepare the powder mixtures, which are hydrostatically compacted in Ar-atmosphere at a nominal pressure of 5 GPa applied. Pre-compacted samples are then severely deformed by HPT for 50 or 100 turns at the same pressure at room temperature. A detailed description of the used setup is given in Ref. [13]. The resulting samples are 8 mm in diameter and about 0.5 mm thick. Samples in the Co-Cu system are prepared at medium compositional ranges. Co37wt.%-Cu, Co49wt.%-Cu and Co53wt.%-Cu samples are processed using 50 turns at the HPT, leading to shear strains of $\gamma \sim 1500$ at $r = 2$ mm. Co28wt.%-Cu and Co67wt.%-Cu samples are processed by using 100 turns, leading to shear strains of $\gamma \sim 3000$ at $r = 2$ mm. In this system, compositions with lower or higher Co-contents could not be successfully processed, due to large residual Co-particles or cracking during HPT deformation. In the Fe-Cu system, samples with low Fe-content (Fe7wt.%-Cu, Fe14wt.%-Cu, Fe25wt.%-Cu) are processed using 100 turns at the HPT, leading to a shear strain of $\gamma \sim 3000$ at $r = 2$ mm. Samples with higher Fe-contents fail due to shear band formation during HPT deformation. The Fe18wt.%-Ag sample is deformed with 100 turns at the HPT ($\gamma \sim 3000$ at $r = 2$ mm).

Figure A.1 shows a schematic diagram of an as-deformed sample and a layout of the positions where the measurements are carried out. Vickers hardness measurements are performed at half height of the sample in a tangential direction in steps of $\Delta r = 0.25$ mm (not shown). Further investigations of the microstructure are carried out by scanning electron microscopy (SEM; Zeiss LEO 1525, LEO Electron Microscopy Inc., Thornwood, USA) in a tangential direction of the sample. The chemical compositions of the samples, as stated above, are measured by energy dispersive X-ray spectroscopy (EDX; Model 7426, Oxford Instruments plc, Abingdon, UK). To investigate the grain sizes, an EBSD/TKD (Electron Back Scattering Diffraction/Transmission Kikuchi Diffraction) system (Bruker Nano GmbH, Berlin, Germany) attached to the SEM was used. For TKD data analysis, the manufacturer's software Esprit version 2.1 was utilized. Additional microstructural investigations are carried out with synchrotron X-ray diffraction measurements in transmission mode (Petra III: P07 synchrotron facility at Deutsches Elektronen-Synchrotron DESY, Hamburg, Germany; Beam Energy: 100 keV; Beam Size: 0.2×0.2 mm²). Diffraction patterns are recorded in the axial orientation at $r \geq 2$ mm.

A. Magnetic Binary Supersaturated Solid Solutions Processed by Severe Plastic Deformation

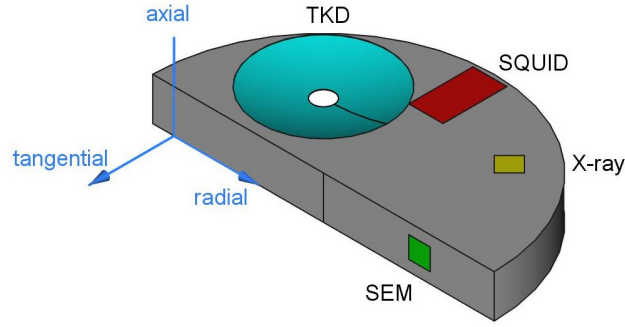


Figure A.1.: Schematic representation of half of an high-pressure torsion (HPT) sample. Regions for the described measurements are highlighted. Scanning Electron Microscopy (SEM) images are taken in a tangential direction of the sample at $r \geq 2$ mm, Transmission Kikuchi Diffraction (TKD) investigations are carried out in the samples axial direction. X-ray diffraction (XRD) measurements are carried out in transmission mode ($r \geq 2$ mm; beam parallel to axial direction). Samples for SQUID-magnetometric measurements are cut out at $r \geq 2$ mm.

Magnetic properties are measured in a SQUID-Magnetometer (Quantum Design MPMS-XL-7, Quantum Design, Inc., San Diego, USA) operated with the manufacturer's software MPMS MultiVu Application (version 1.54). The applied magnetic field points in the axial orientation of the sample. Magnetic hysteresis are measured at 300 K in magnetic fields up to 70 kOe. Zero Field Cooling (ZFC) and Field Cooling (FC) measurements are recorded between 5 K and 300 K at 50 Oe.

A.3. Results and Disussion

A.3.1. Microstructure

Vickers hardness measurements are carried out as the measurements are very sensitive to small changes in the microstructure. Hardness values plotted versus shear strain showed a saturation behavior starting at $r \geq 2$ mm, indicating the as-deformed microstructures reached a steady state above this position.

Figure A.2a–c show SEM images of as-deformed Co-Cu samples, taken in a tangential direction of the sample at $r \geq 2$ mm (back-scatter mode). The micrographs indicate a homogeneous phase and show very small grain sizes in the nanocrystalline regime. Figure A.2d–f show TKD orientation maps of similar samples, taken in an axial direction. At least three EBSD-scans per specimen were jointly analyzed to evaluate the area weighted grain sizes. Taking only high angle boundaries into account leads to the following results: 100 nm, 78 nm

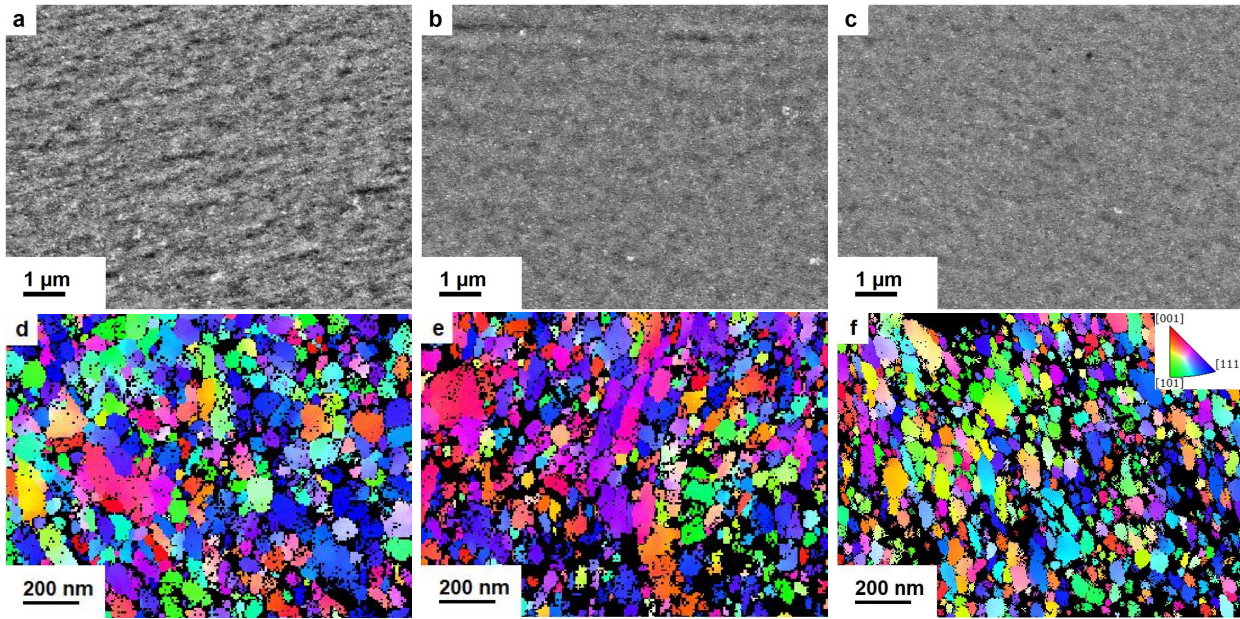


Figure A.2.: Backscattered Electrons (BSE) micrographs of as-deformed Co-Cu samples at $r \geq 2$ mm in tangential direction. Images of Co28wt.%-Cu (a); Co49wt.%-Cu (b); and Co67wt.%-Cu (c) show homogeneous microstructures. In (d–f), the corresponding TKD images, taken along the axial direction, are shown. High Co-containing compositions show smaller grain sizes.

and 77 nm for Co28wt.%-Cu, Co49wt.%-Cu, Co67wt.%-Cu, respectively. SEM images of Fe-Cu with low (7 wt.%) and high (25 wt.%) Fe-contents are shown in Figure A.3a,b. A few remaining particles are visible in the micrograph of Fe25wt.%-Cu. In Figure A.3c, the SEM image of Fe18wt.%-Ag is displayed. The deformed microstructure exhibits many remaining dark particles at various sizes.

Statistically significant information of each sample's constituting phases are revealed by synchrotron diffraction measurements, as shown in Figure A.4. In the diffraction patterns of the Co-Cu samples (Figure A.4a), only very weak occurrence of hcp-Co may persist. The received patterns consist mainly of fcc-peaks, showing that Co undergoes a phase transformation from hcp to fcc during HPT as reported in previous studies [14–16]. The deviations of the fcc-Cu peaks can be explained with the change of the chemical composition of the samples, summarizing that the received microstructures is mainly fcc, either rich in Cu or Co.

Diffraction patterns of Fe-Cu (Figure A.4b) samples exhibit pronounced peaks of fcc-Cu, but also weak bcc-Fe peaks can be identified. These results are in agreement with SEM images as described above, which also show a few remaining particles and leads to the conclusion that a dual phase structure is present. The diffraction pattern of the Fe18wt.%-Ag sample

A. Magnetic Binary Supersaturated Solid Solutions Processed by Severe Plastic Deformation

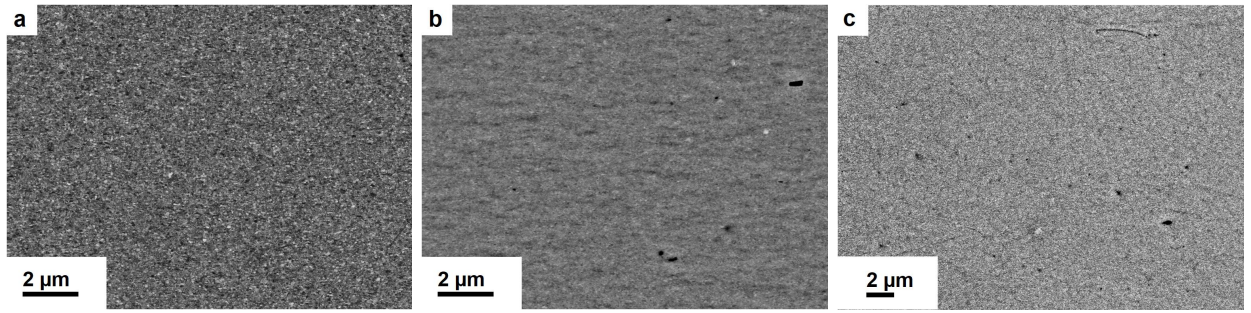


Figure A.3.: BSE micrographs of as-deformed Fe-based samples at $r \geq 2$ mm along the tangential direction. The microstructure of Fe7wt.-%-Cu (a) appears homogenous. Fe25wt.-%-Cu (b) exhibits some remaining particles embedded in a highly homogeneous matrix. Fe18wt.-%-Ag (c) shows high contrast variations indicating less Fe dissolved in the Ag-matrix.

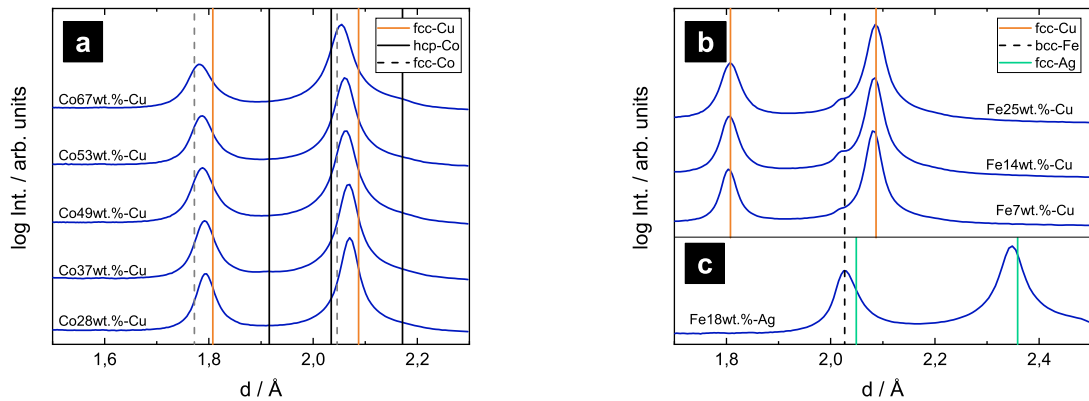


Figure A.4.: Synchrotron XRD patterns of as-deformed samples. In the patterns of Co-Cu samples (a), only one set of fcc-peaks remains; (b) XRD patterns of Fe-Cu samples show pronounced fcc-Cu peaks and weak bcc-Fe peaks. In the XRD pattern of Fe18wt.-%-Ag, (c) bcc-Fe and fcc-Ag peaks overlap.

is shown in Figure A.4c. The occurring phases in the pattern can not be clearly identified due to an overlap in the bcc-Fe and fcc-Ag peaks. These peaks are very broad, indicating a remaining dual phase structure.

A.3.2. Magnetism

Figure A.5a shows the hysteresis of Co-Cu samples measured at 300 K. The magnetic moment per gram of cobalt is plotted versus the applied field. The three samples with the highest Co-content (Co49wt.-%-Cu, Co53wt.-%-Cu, Co67wt.-%-Cu) saturate easily, indicating a pronounced ferromagnetic ordering. The saturation behavior of the samples with lower

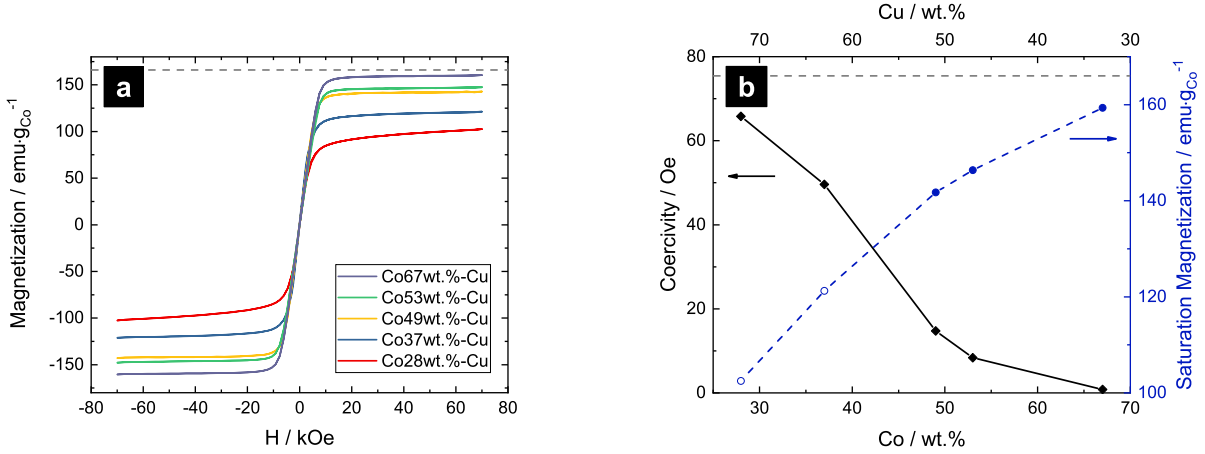


Figure A.5.: (a) magnetization versus applied field for Co-Cu samples measured at 300 K; (b) coercivity and saturation magnetization are plotted versus Co-content. The grey dotted lines in both figures indicate the magnetic moment of fcc-Co ($166 \text{ emu}\cdot\text{g}^{-1}$). Full saturation is not achieved for Co contents ≤ 40 wt.% in a field of 70 kOe (open symbols in (b)).

Co-content, Co28wt.%-Cu and Co37wt.%-Cu illustrate a slight increase of the magnetization with increasing magnetic field. Saturation is not completed even at the highest applied field of 70 kOe, which indicates a paramagnetic contribution and, therefore, a partial breakdown in the long-range ordering. In Figure A.5b, the magnetic moment per gram of Co in saturation is plotted versus the Co-content. Therefore, the mean of the magnetic moment was calculated at fields between 20 kOe and 70 kOe (filled symbols). For the samples with low Co-content, Co28wt.%-Cu and Co37wt.%-Cu, the magnetization at 70 kOe is plotted (open symbols). It can be seen that the magnetic moment of Co increases with increasing Co-content and approaches the magnetic moment of bulk fcc-Co ($166 \text{ emu}\cdot\text{g}^{-1}$ [17]). This result is in accordance with findings on magnetron sputtered Co-Cu, but slightly shifted towards higher magnetic moments [3]. The coercivity is evaluated with a least-squares fit of the hysteresis two halves between -800 Oe and 800 Oe and plotted in Figure A.5b. The coercivity decreases with increasing Co-content, reaching from 66 Oe down to 0.8 Oe.

From the TKD analysis, it was shown that high Co-containing compositions exhibit smaller grain sizes than low Co-containing compositions. Comparing the coercivity of the samples with their grain sizes, it can be seen that the coercivity decreases with decreasing grain size, entering the regime of random anisotropy due to exchange coupled nanograins. Apart from the decrease in grain size, the various chemical compositions may also lead to deviations of the micromagnetic properties.

In Figure A.6a, the hysteresis of the Fe-Cu samples are shown. The magnetic moment

A. Magnetic Binary Supersaturated Solid Solutions Processed by Severe Plastic Deformation

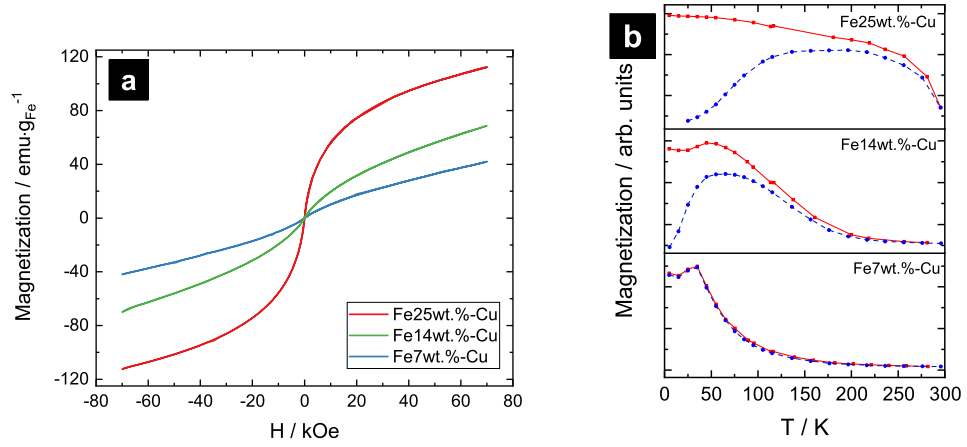


Figure A.6.: (a) magnetization versus applied field for Fe-Cu samples measured at 300 K. Saturation is not achieved, even at the highest applied field; (b) ZFC-FC for Fe-Cu samples at 50 Oe. Splitting is not pronounced for Fe7wt.%-Cu. For Fe7wt.%-Cu and Fe14wt.%-Cu a cusp at the FC-curve is found.

per gram of Fe is plotted versus applied field. The hysteresis of the Fe-Cu samples show a very pronounced paramagnetic behavior at high applied fields. At low fields, a steep increase in magnetization occurs, indicating the presence of long-range magnetic ordering and, therefore, a ferromagnetic phase as expected from SEM and synchrotron XRD measurements. This contribution increases with increasing Fe-content. The magnetization, even at the highest applied field, is far away from the value of bulk bcc-Fe at $222 \text{ emu}\cdot\text{g}^{-1}$ for all investigated compositions. This can be explained by the disorder of surface spins on genuine Fe clusters formed by HPT deformation. Further magnetic characterization is carried out by performing temperature dependent measurements at low magnetic field (50 Oe). Results of ZFC-FC measurements on the Fe-Cu samples are shown in Figure A.6b. In the ZFC-FC measurement of Fe25wt.%-Cu and Fe14wt.%-Cu, superparamagnetic blocking peaks below room temperature can be identified, indicating the presence of remaining Fe clusters. Splitting of the ZFC-FC-curves is not pronounced for the Fe7wt.%-Cu sample, but Fe7wt.%-Cu and Fe14wt.%-Cu show a cusp in the FC curve at very low temperatures. Its origin may be found in spin-glass behaviour, as reported in Refs. [18–20]. This phase transition is expected to apply for Fe-contents below 20 at.% at about 50 K [2], which leads to the assumption that Fe is not only clustered, but is also partially diluted in Cu. As the expected magnetic effects for Fe-Cu samples are highly sensitive to the elemental distributions, further microstructural investigations need to be carried out at atomic scales (e.g., by Atom Probe Tomography) to get more in-depth information.

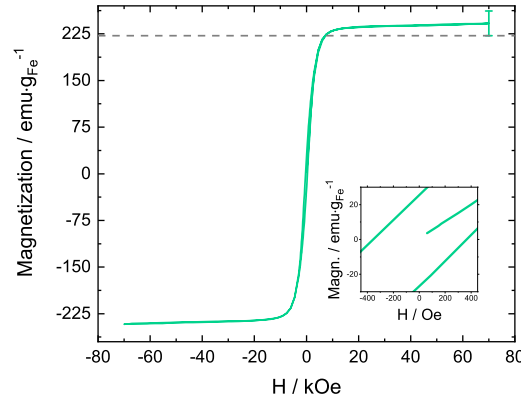


Figure A.7.: Magnetization versus applied field for Fe18wt.%-Ag measured at 300 K. The saturation magnetization is $240 \pm 20 \text{ emu}\cdot\text{g}^{-1}$, the coercivity is 400 Oe.

The hysteresis of the Fe18wt.%-Ag sample is shown in Figure A.7. Any deviation between the saturation magnetization and the magnetic moment of bulk bcc-Fe is in the range of the chemical composition uncertainty, leading to the conclusion that no distortion of the Fe magnetic moment is observed. The coercivity, evaluated as described above, is 400 Oe. These results again indicate that no intermixing between Ag and Fe takes place during HPT and a dual-phase structure remains. It can be concluded that, for the Fe18wt.%-Ag sample, only grain refinement takes place.

A.4. Conclusions

Binary solid solutions are processed by HPT. Three different systems, immiscible at the thermodynamic equilibrium and consisting of one ferromagnetic and one diamagnetic component, are investigated (Co-Cu, Fe-Cu, Fe-Ag). Correlating microstructural and magnetic data lead to the following results: for Co-Cu samples, fcc-structures can be processed in the medium composition range. Higher Co-containing compositions show the smallest grain sizes as well as the lowest coercivity, demonstrating that the coercivity can be tuned by varying the chemical composition. Co-Cu HPT samples are near the crossover of free-domain motion and exchange-coupling of ultra-small grains exhibiting randomization of anisotropy, with nearly identical initial susceptibilities independent of Co-composition. On the other hand, Fe-Cu samples deliver phase separation of Fe-grains with monodomain magnetism obeying Stoner–Wolfarth behavior with strongly composition dependent slopes of hysteresis curves and a typical magnetic blocking effect. For Fe-concentrations below 20 wt.%, a partial

dissolution of Fe in Cu is expected with spin-glass behavior (to be probed by frequency dependent AC susceptibility measurements). For the Fe-Ag sample, magnetic measurements indicate only grain refinement, but no intermixing of the elemental phases takes place.

Author Contributions

Conceptualization, M.S., R.P. and A.B.; Methodology, M.S., S.W. and A.B.; Validation, M.S., H.K., R.P., L.W., S.W. and A.B.; Formal Analysis, M.S., Investigation, M.S. and S.W.; Resources, H.K.; Data Curation, M.S.; Writing—Original Draft Preparation, M.S.; Writing—Reviewing and Editing H.K., R.P., L.W., S.W. and A.B.; Visualization, M.S.; Supervision, R.P. and A.B.; Funding Acquisition, A.B.

Funding

This project has received funding from the European Research Council (ERC) under the European Union’s Horizon 2020 research and innovation programme (Grant No. 757333).

Acknowledgements

The measurements leading to these results have been performed at PETRA III: P07 at DESY Hamburg (Germany), a member of the Helmholtz Association (HGF). We gratefully acknowledge the assistance by Norbert Schell. The authors thank Karoline Kormout, Sandra Ebner, Christina Hofer and Stefan Zeiler for their help with the synchrotron measurements.

Conflicts of Interest

The authors declare no conflict of interest.

Abbreviations

The following abbreviations are used in this manuscript:

BSE	Backscattered Electrons
EBSD	Electron Backscatter Diffraction
EDX	Energy Dispersive X-Ray Spectroscopy
FC	Field Cooling
HPT	High-Pressure Torsion
SEM	Scanning Electron Microscopy
SPD	Severe Plastic Deformation
SQUID	Superconducting Quantum Interference Device
TKD	Transmission Kikuchi Diffraction
ZFC	Zero Field Cooling

A.5. References

- [1] T. Traußnig et al. “Magnetization of Fe-oxide based nanocomposite tuned by surface charging”. In: *Phys. Status Solidi* 5.4 (2011), pp. 150–152. DOI: 10.1002/pssr.201004483.
- [2] C.L. Chien, S.H. Liou, and M.A. Gatzke. “Magnetic Percolation in new crystalline fcc Fe-Cu Alloys”. In: *MRS Proc.* 80 (1987), pp. 395–400. DOI: 10.1557/PROC-80-395.
- [3] J.R. Childress and C.L. Chien. “Reentrant magnetic behavior in fcc Co-Cu alloys”. In: *Phys. Rev. B* 43.10 (1991), p. 8089. DOI: 10.1103/PhysRevB.43.8089.
- [4] P. Crespo et al. “Magnetic and structural properties of as-milled and heat-treated bcc-Fe₇₀Cu₃₀ alloy”. In: *J. Magn. Magn. Mater.* 150 (1995), pp. 409–416. DOI: 10.1016/0304-8853(95)00280-4.
- [5] T. Ambrose, A. Gavrin, and C.L. Chien. “Magnetic properties of metastable fcc Fe-Cu alloys prepared by high energy ball milling”. In: *J. Magn. Magn. Mater.* 124 (1993), pp. 15–19. DOI: 10.1016/0304-8853(93)90063-8.
- [6] R. Pippan et al. “Saturation of fragmentation during severe plastic deformation”. In: *Annu. Rev. Mater. Sci.* 40 (2010), pp. 319–343. DOI: 10.1146/annurev-matsci-070909-104445.
- [7] R.Z. Valiev, R.K. Islamgaliev, and I.V. Alexandrov. “Bulk nanostructured materials from severe plastic deformation”. In: *Prog. Mater. Sci.* 45.2 (2000), pp. 103–189. DOI: 10.1016/S0079-6425(99)00007-9.
- [8] K.S. Kormout, R. Pippan, and A. Bachmaier. “Deformation-induced supersaturation in immiscible material systems during high-pressure torsion”. In: *Adv. Eng. Mater.* 19.4 (2017), p. 1600675. DOI: 10.1002/adem.201600675.

- [9] X. Sauvage, F. Wetscher, and P. Pareige. “Mechanical alloying of Cu and Fe induced by severe plastic deformation of a Cu-Fe composite”. In: *Acta Mater.* 53.7 (2005), pp. 2127–2135. DOI: 10.1016/j.actamat.2005.01.024.
- [10] A. Bachmaier et al. “Tailoring the magnetic properties of nanocrystalline Cu-Co alloys prepared by high-pressure torsion and isothermal annealing”. In: *J. Alloys Compds.* 725 (2017), pp. 744–749. DOI: 10.1016/j.jallcom.2017.07.200.
- [11] G. Herzer. “Soft magnetic nanocrystalline materials”. In: *Scr. Mater.* 33.10-11 (1995), pp. 1741–1756. DOI: 10.1016/0956-716X(95)00397-E.
- [12] R. Alben, J.J. Becker, and M.C. Chi. “Random anisotropy in amorphous ferromagnets”. In: *J. Appl. Phys.* 49.3 (1978), pp. 1653–1658. DOI: 10.1063/1.324881.
- [13] A. Hohenwarter et al. “Technical parameters affecting grain refinement by high pressure torsion”. In: *I. J. Mater. Res.* 100.12 (2009), pp. 1653–1661. DOI: 10.3139/146.110224.
- [14] A. Bachmaier et al. “Phase separation of a supersaturated nanocrystalline Cu-Co alloy and its influence on thermal stability”. In: *Acta Mater.* 96 (2015), pp. 269–283. DOI: 10.1016/j.actamat.2015.05.0530.
- [15] K. Edalati et al. “High-pressure torsion of pure cobalt: hcp-fcc phase transformations and twinning during severe plastic deformation”. In: *Appl. Phys. Lett.* 102.18 (2013), p. 181902. DOI: 10.1063/1.4804273.
- [16] J. Sort et al. “Microstructural effects and large microhardness in cobalt processed by high pressure torsion consolidation of ball milled powders”. In: *Acta Mater.* 51.20 (2003), pp. 6385–6393. DOI: 10.1016/j.actamat.2003.08.006.
- [17] M. B. Stearns. *1.1.2.4 Spontaneous magnetization, magnetic moments and high-field susceptibility: Datasheet from Landolt-Börnstein - Group III Condensed Matter Volume 19A: “3d, 4d and 5d Elements, Alloys and Compounds” in SpringerMaterials*. Ed. by H.P.J. Wijn. 1986.
- [18] K. Adachi et al. “Spin Glass of liquid-quenched Cu-Fe alloys”. In: *J. Magn. Magn. Mater.* (1986), pp. 80–81. DOI: 10.1016/0304-8853(86)90511-1.
- [19] J.M. Franz and D.J. Sellmyer. “Magnetic Interactions and High-Field Magnetization in Dilute Magnetic Alloys”. In: *Phys. Rev. B* 8.5 (1973). DOI: 10.1103/PhysRevB.8.2083.
- [20] A.V. Vedyayev and V. Cherenkov. “Spin Glass State in Alloys of Copper With Manganese, Iron and Cobalt”. In: *Sov. Phys. JETP-USSR* 55.2 (1982), pp. 287–290.

B. Magnetic dilution by severe plastic deformation

Martin Stückler¹, Lukas Weissitsch¹, Stefan Wurster¹, Peter Felfer², Heinz Krenn³, Reinhard Pippan¹ and Andrea Bachmaier¹

¹ *Erich Schmid Institute of Materials Science, Austrian Academy of Sciences, Jahnstraße 12, 8700 Leoben, Austria*

² *Department of Materials Science, Friedrich-Alexander-Universität Erlangen-Nürnberg, Martensstraße 5, 91058 Erlangen, Germany*

³ *Institute of Physics, University of Graz, Universitätsplatz 5, 8010 Graz, Austria*

Abstract

Mixtures of Fe and Cu powders are cold-compacted and subsequently deformed with severe plastic deformation by high-pressure torsion, leading to bulk samples. The dilution of Fe in the Cu matrix is investigated with SQUID-magnetometry, whereas the magnetic properties change as a function of Fe-content from a frustrated regime to a thermal activated behaviour. The magnetic properties are correlated with the microstructure, investigated by synchrotron X-ray diffraction and atom probe tomography. Annealing of the as-deformed states leads to demixing and grain growth, with the coercivity as a function of annealing temperature obeying the random anisotropy model. The presented results show that high-pressure torsion is a technique capable to affect the microstructure even on atomic length scales.

B.1. Introduction

Metastable phases exhibit a high potential in application, since attractive functional and magnetic properties were observed in such non-equilibrium states [1–3]. In particular, the

B. Magnetic dilution by severe plastic deformation

immiscible Fe-Cu system is of great interest, as Fe, mixed with a low amount of Cu, exhibits desirable magnetostrictive properties [4]. On the other hand, Cu mixed with low amounts of Fe shows the granular giant magnetoresistive effect [5, 6]. But all of the mentioned studies have in common, that sample preparation routes were used, which are hardly accessible for industrial applications in terms of bulk products. Whereas magnetron sputtering or vapour depositions turn out to be not feasible on large scales, upscaling is possible in the case of mechanical alloying or rapid solidification. Anyway, one has to prepare a bulky sample, either from powder or thin ribbons. Therefore, sample preparation directly in bulk form is desirable. Techniques of severe plastic deformation, such as high-pressure torsion (HPT), are capable to prepare such metastable phases directly in bulk form and can also be used at large scales. However the achievable degree of intermixing has to be examined. Therefore, non-equilibrium Fe-Cu samples are processed with HPT in this study, whereas intermixing is investigated for various Fe-contents with advanced microstructural characterization techniques in combination with SQUID-magnetometry.

B.2. Experimental

Powder mixtures, consisting of high purity powders (Fe: MaTeck 99.9% -100 +200 mesh, Cu: AlfaAesar 99.9% -170 +400 mesh), were prepared with three different Fe-contents, namely Fe07wt%-Cu, Fe14wt%-Cu and Fe25wt%-Cu, and hydrostatically compacted at 5 GPa. The cylindrical samples ($d=8$ mm, $h\sim 0.5$ mm) were subsequently deformed with HPT at 5 GPa for 100 turns at room temperature. The applied amount of shear strain at $r=3$ mm was $\gamma\sim 3000$. More details on sample preparation can be found elsewhere [7]. All compositions were exposed to annealing treatments at 150°C, 250°C and 500°C for 1 h each, which were conducted in vacuum ($p\leq 10^{-3}$ mbar) to prevent oxidation. Microstructural analysis was carried out with a scanning electron microscope (SEM; Zeiss LEO 1525), with attached electron backscatter diffraction (EBSD; Bruker Nano eFlash^{FS}), in samples tangential direction. Investigation on crystallographic compositions was carried out with synchrotron X-ray diffraction at DESY (beam energy: 100 kV; beam size: 0.2x0.2 mm²). The beam was oriented in axial direction of the sample at $r=3$ mm. Further microstructural analysis was performed via atom probe tomography (APT) experiments on a LEAP4000 X at 50 K in laser mode with a pulse repetition rate of 250 kHz. Magnetic properties were investigated using a SQUID-magnetometer (Quantum Design MPMS-XL-7).

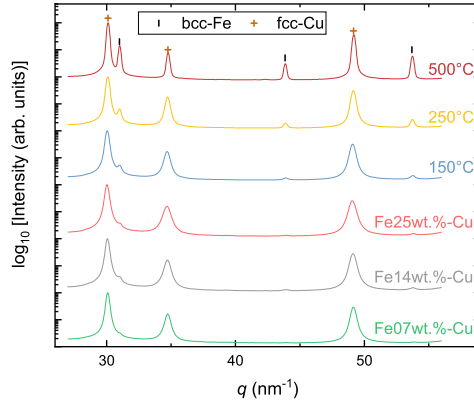


Figure B.1.: Synchrotron-XRD diffraction patterns of as-deformed samples and of Fe14wt.%-Cu in annealed states, measured in transmission mode.

B.3. Results and Discussion

B.3.1. Microstructural Characterization

HPT-processing applies a shear strain onto the sample, which increases with increasing radius [8], causing a microstructural evolution, which strongly affects the mechanical properties. To verify that a steady state is reached, Vickers hardness testing is carried out. The hardness shows a saturating behaviour at $r \geq 1$ mm for 100 turns and therefore further investigations are carried out at large radii. Fig. B.1 shows synchrotron XRD-patterns of as-deformed samples, as well as the patterns of Fe14wt.%-Cu in annealed states as an example. The as-deformed samples exhibit very prominent fcc-Cu peaks, but tiny bcc-Fe peaks can also be identified. The latter are two orders in magnitude smaller and reveal the presence of residual Fe-particles. Annealed samples show an increasing intensity for bcc-Fe, indicating demixing. While the peak-width of the 150°C-annealed sample does not change with respect to the as-deformed state, the 250°C- and the 500°C-annealed sample both show a narrowing of peak-width arising from grain growth. Annealed Fe07wt.%-Cu and Fe25wt.%-Cu samples exhibit the same behaviour.

B.3.2. Magnetic Properties

The magnetization versus the applied magnetic field is measured in the as-deformed state for all compositions at 300 K and at 8 K (Fig. B.2). The hysteresis, measured at 300 K,

B. Magnetic dilution by severe plastic deformation

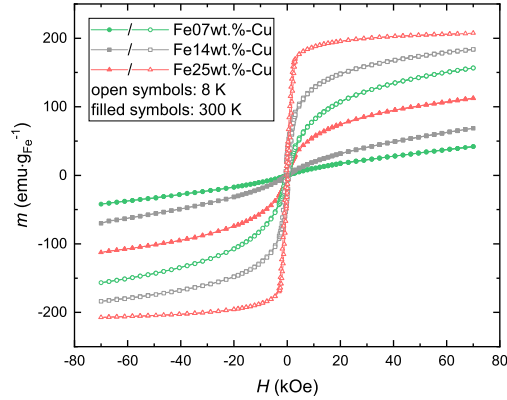


Figure B.2.: Specific magnetization m versus the applied field H as a function of Fe-concentration, measured at 300 K and 8 K. Note: the saturation magnetization of bulk Fe is 220 emu/g.

do not saturate, even at the highest applied field of 70 kOe. The observed high-field susceptibility is expected to arise from diluted Fe with suppressed long-range interaction. A non-zero high-field susceptibility was also observed in measurements at 8 K. Although the hysteresis show paramagnetic features, non-zero coercivities are observed. Fig. B.3 shows the coercivities deduced from hysteresis measurements for all investigated configurations. The coercivity as a function of annealing temperature shows the same development in all investigated compositions. This behaviour can be correlated with the microstructural states in this system. It is known, that HPT-processed samples exhibit a high amount of residual stresses σ in the as-deformed state [9]. The high magnetostriction λ_S of Fe gives then rise to an enhancement of anisotropy by magnetoelastic anisotropy, which reads $K_\sigma = 3/2 \cdot \sigma \lambda_S$. Approximating the coercivity with the anisotropy field, as proposed in the Stoner-Wohlfarth model, $H_C \propto K_{eff}/M_S$, this further leads to an increase in coercivity [10]. Upon annealing at 150°C neither grain growth nor demixing was observed, but recovery mechanisms lead to a reduction in residual stresses [11], which therefore lowers the coercivity. The coercivity of the as-deformed, as well as of the 150°C-annealed sample arises therefore from random anisotropy [12]. Annealing at higher temperatures leads to demixing and grain growth. The coercivity as a function of annealing temperature increases for the 250°C-annealed sample to around 400 Oe. The random anisotropy model peaks at $d = \sqrt{A/K}$ and breaks down for larger grain sizes d . Using typical values for bcc-Fe [13], the peak coercivity can be calculated to $H_C \approx 600$ Oe, in the order of the measured value. Annealing at 500°C leads to a drop in coercivity, indicating a crossover from single-domain to multi-domain behaviour with a

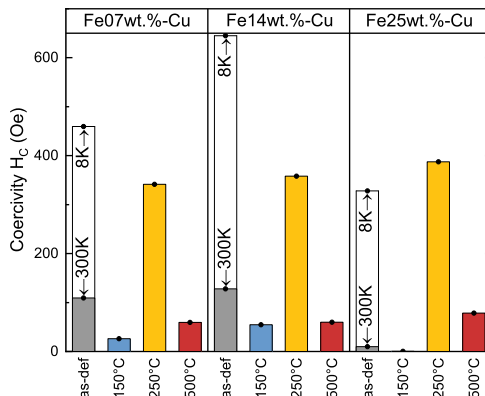


Figure B.3.: Coercivity H_C as a function of Fe-concentration and annealing temperature. The coercivity shows the same behaviour in all investigated compositions. Filled bars represent measurements at 300 K, whereas open bars represent measurements at 8 K. For the 150°C annealed state of Fe25wt.%-Cu the coercivity is below the measurements resolution.

classical $1/d$ -scaling law. Fig. B.4 shows the phase map derived from an EBSD scan of the 500°C-annealed sample (Fe14wt%-Cu). The Fe grain size was analyzed to $d=(210\pm 80)$ nm. The corresponding coercivity can be calculated, leading to $H_C^{th}=(100\pm 50)$ Oe, higher than the coercivity determined from hysteresis measurements ($H_C=60$ Oe). For HPT-processed samples, grains elongate in radial direction, therefore the grain size is underestimated in the direction observed in the EBSD scan, which might explain the deviation.

Additionally, low-field magnetic measurements are carried out. In Zero-Field Cooling (ZFC) measurements, the demagnetized sample is cooled in the absence of an external field. Starting from the lowest observed temperature, the magnetic moment is recorded during heating. In Field-Cooling (FC) measurements, the magnetic moment is recorded during cooling in an external field. Fig. B.5 shows ZFC/FC-measurements for the as-deformed states. For reasons of comparability, the data are normalized, i.e. the susceptibility at 300 K is subtracted from all values. Herein, Fe25wt.%-Cu shows a large splitting and a broad peak in the ZFC-curve, which is a typical behaviour for thermal activation [14]. The ZFC/FC-curves of Fe14wt.%-Cu also shows splitting of both curves, but in the FC-curve also a maximum at around 50 K can be identified. A local maximum in the FC-curve is also observed in Fe07wt.%-Cu. In the literature this feature is often attributed to a spin-glass behaviour of diluted Fe [15–17].

B. Magnetic dilution by severe plastic deformation

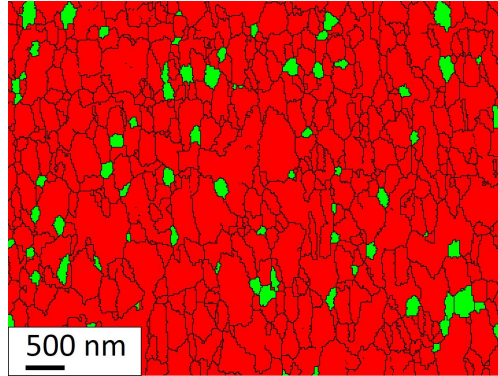


Figure B.4.: Post-processed EBSD scan of Fe14wt.%-Cu, annealed at 500°C. Red regions represent Cu grains, while green regions represent Fe grains. Lines mark grain boundaries. The mean grain size of Fe is determined to (210 ± 80) nm. The shearing direction is parallel to the horizontal axis.

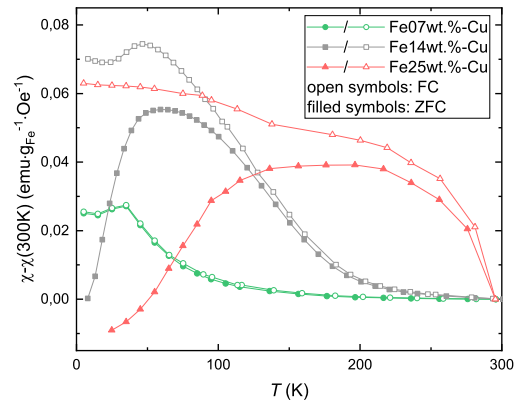


Figure B.5.: Normalized zero-field cooling and field-cooling curves of as-deformed samples as a function of Fe-concentration. In all measurements a field of $H=50$ Oe was applied. Open symbols represent FC-curves, whereas filled symbols represent ZFC-curves.

B.3.3. Atom probe tomography

To investigate the distribution of Fe on the atomic scale, APT experiments are carried out. As mentioned above, the splitting in the ZFC/FC-curve is attributed to thermal activation, and therefore to the presence of Fe particles, small enough for thermal relaxation. Thus, the measured APT data is analyzed with respect to Fe-clusters, using Delaunay triangulation. Details on the used clustering algorithm can be found elsewhere [18]. In Fig. B.6(a)-(c) the atom probe reconstruction of Fe07wt.%-Cu, Fe14wt.%-Cu and Fe25wt.%-Cu respectively is plotted, showing the distribution of Fe. Therein, Fe25wt.%-Cu shows large volumes of clustered Fe-atoms, as expected from the observed ZFC/FC-curve. In Fig. B.6(d)-(f) the results from the clustering algorithm are shown. Qualitative differences arise, as the formation of Fe-clusters depends on the present local crystallographic defects. The cluster sizes span over a wide range, whereas the cluster size for Fe25wt.%-Cu shows the broadest distribution. This can also be attributed to the observed maxima in the ZFC/FC-measurements (Fig. B.5), which are expected to arise from magnetic blocking. Anyway, in every sample about 95% of all Fe-atoms are rejected by the clustering algorithm, meaning the majority of Fe-atoms is diluted in the Cu-matrix, which explains the large high-field susceptibility in Fig. B.2. One important parameter to achieve accurate spatial reconstruction is the detection efficiency of the used APT system. In [19] it has been shown, that the cluster size distribution is systematically underestimated by the detection efficiency.

B.4. Conclusion

In this study, the magnetic and the microstructural properties of HPT-processed binary Fe-Cu samples, in the as-deformed as well as in annealed states, are correlated, whereas a specific focus is on the investigation of the amount of intermixing. In the as-deformed states, Fe is present in two different configurations, namely diluted in the fcc-Cu matrix, as well as in form of clusters. The ratio of clustered and diluted Fe varies as a function of composition and gives rise to either thermal relaxation (in case of Fe25wt.%-Cu), magnetic frustration (in case of Fe07wt.%-Cu) or a superposition of both, which is true for Fe14wt.%-Cu. The results further prove that intermixing of Fe and Cu can be obtained with HPT on an atomic scale. The coercivity as a function of the annealing temperature complies the random anisotropy model, showing Fe-particle sizes below the exchange length persist in annealed states, which further gives rise to magnetic tunability.

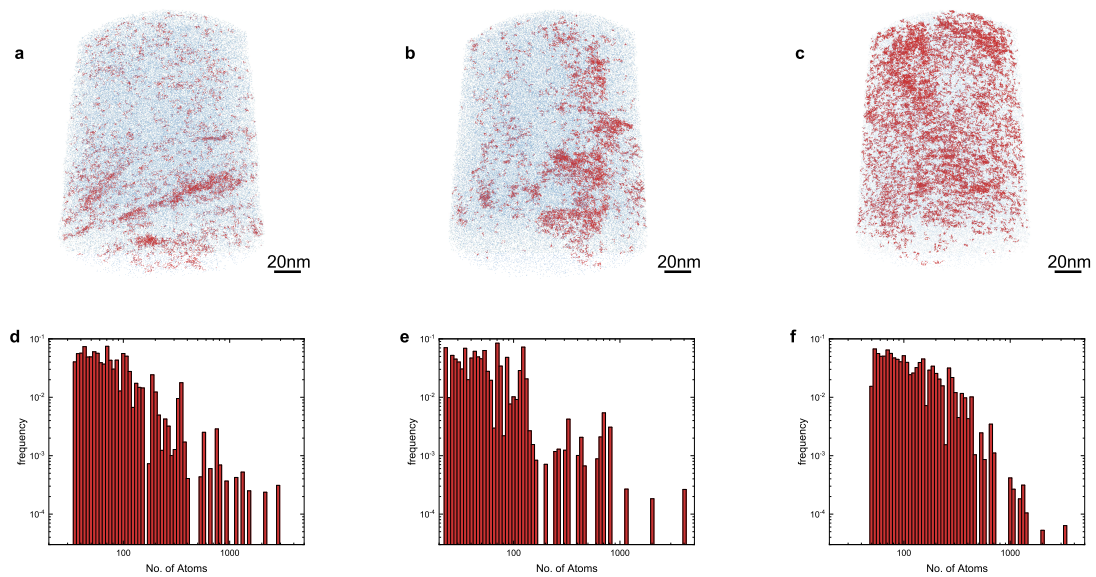


Figure B.6.: APT reconstruction data for Fe07wt.%-Cu (a), Fe14wt.%-Cu (b) and Fe25wt.%-Cu (c). 10^5 Fe-Atoms are plotted (blue dots). Red dots represent clustered Fe-Atoms. (d)-(f) show the Fe-cluster size distributions of Fe07wt.%-Cu, Fe14wt.%-Cu and Fe25wt.%-Cu, respectively.

Acknowledgments

This project has received funding from the European Research Council (ERC) under the European Union’s Horizon 2020 research and innovation programme (Grant No. 757333). Synchrotron measurements have been performed at PETRA III: P07 at DESY Hamburg (Germany), a member of the Helmholtz Association (HGF). We gratefully acknowledge the assistance by N. Schell. The authors thank F. Spieckermann and C. Gammer for their help with data processing.

B.5. References

- [1] A.E. Berkowitz et al. “Giant magnetoresistance in heterogeneous Cu-Co and Ag-Co alloy films”. In: *J. Appl. Phys.* 73.10 (1993), pp. 5320–5325. DOI: 10.1063/1.353767.
- [2] T. Ambrose, A. Gavrin, and C.L. Chien. “Magnetic properties of metastable fcc Fe-Cu alloys prepared by high energy ball milling”. In: *J. Magn. Magn. Mater.* 124 (1993), pp. 15–19. DOI: 10.1016/0304-8853(93)90063-8.

- [3] J. He et al. “Transition from negative magnetoresistance behavior to positive behavior in $\text{Co}_{20}(\text{Cu}_{1-x}\text{Ge}_x)_{80}$ ribbons”. In: *Appl. Phys. Lett.* 80.10 (2002), pp. 1779–1781. DOI: 10.1063/1.1458682.
- [4] P. Gorria et al. “Invar effect in fcc-FeCu solid solutions”. In: *Phys. Rev. B* 69.21 (2004), p. 214421. DOI: 10.1103/PhysRevB.69.214421.
- [5] J.Q. Xiao, J.S. Jiang, and C.L. Chien. “Giant magnetoresistance in nonmultilayer magnetic systems”. In: *Phys. Rev. Lett.* 68.25 (1992), p. 3749. DOI: 10.1103/PhysRevLett.68.3749.
- [6] J.-Q. Wang, P. Xiong, and G. Xiao. “Investigation of giant magnetoresistance in magnetic, concentrated, nanostructured alloys”. In: *Phys. Rev. B* 47.13 (1993), p. 8341. DOI: 10.1103/PhysRevB.47.8341.
- [7] M. Stücker et al. “Magnetic Binary Supersaturated Solid Solutions Processed by Severe Plastic Deformation”. In: *Nanomaterials* 9.1 (2018), p. 6. DOI: 10.3390/nano9010006.
- [8] R.Z. Valiev, R.K. Islamgaliev, and I.V. Alexandrov. “Bulk nanostructured materials from severe plastic deformation”. In: *Prog. Mater. Sci.* 45.2 (2000), pp. 103–189. DOI: 10.1016/S0079-6425(99)00007-9.
- [9] J. Todt et al. “Gradient residual strain and stress distributions in a high pressure torsion deformed iron disk revealed by high energy X-ray diffraction”. In: *Scr. Mater.* 146 (2018), pp. 178–181. DOI: 10.1016/j.scriptamat.2017.11.037.
- [10] T.D. Shen, R.B. Schwarz, and J.D. Thompson. “Soft magnetism in mechanically alloyed nanocrystalline materials”. In: *Phys. Rev. B* 72.1 (2005), p. 014431. DOI: 10.1103/PhysRevB.72.014431.
- [11] A. Bachmaier et al. “The formation of supersaturated solid solutions in Fe-Cu alloys deformed by high-pressure torsion”. In: *Acta Mater.* 60.3 (2012), pp. 860–871. DOI: 10.1016/j.actamat.2011.10.044.
- [12] G. Herzer. “Soft magnetic nanocrystalline materials”. In: *Scr. Mater.* 33.10-11 (1995), pp. 1741–1756. DOI: 10.1016/0956-716X(95)00397-E.
- [13] H. Kronmüller and M. Fähnle. *Micromagnetism and the microstructure of ferromagnetic solids*. Cambridge University Press, 2003.
- [14] M. Knobel et al. “Superparamagnetism and other magnetic features in granular materials: a review on ideal and real systems”. In: *J. Nanosci. Nanotechnology* 8.6 (2008), pp. 2836–2857. DOI: 10.1166/jnn.2008.15348.
- [15] O. Schneeweiss et al. “Magnetic properties of the CrMnFeCoNi high-entropy alloy”. In: *Phys. Rev. B* 96.1 (2017), p. 014437. DOI: 10.1103/PhysRevB.96.014437.

- [16] C.L. Chien et al. “Magnetic percolation in new crystalline FCC Fe-Cu alloys”. In: *Mater. Res. Soc. Symp. Proc.* 80 (1986). DOI: 10.1557/PROC-80-395.
- [17] J.A. De Toro et al. “A nanoparticle replica of the spin-glass state”. In: *Appl. Phys. Lett.* 102.18 (2013), p. 183104. DOI: 10.1063/1.4804187.
- [18] P. Felfer et al. “Detecting and extracting clusters in atom probe data: A simple, automated method using Voronoi cells”. In: *Ultramicroscopy* 150 (2015), pp. 30–36. DOI: 10.1016/j.ultramicro.2014.11.015.
- [19] L.T. Stephenson et al. “Estimating the physical cluster-size distribution within materials using atom-probe”. In: *Microsc. Res. Tech.* 74.9 (2011), pp. 799–803. DOI: 10.1002/jemt.20958.

C. Intermixing of Fe and Cu on the atomic scale by high-pressure torsion as revealed by DC- and AC-SQUID susceptometry and atom probe tomography

Martin Stückler¹, Heinz Krenn², Philipp Kürsteiner³, Baptiste Gault^{3,4}, Frédéric De Geuser⁵, Lukas Weissitsch¹, Stefan Wurster¹, Reinhard Pippan¹ and Andrea Bachmaier¹

¹ *Erich Schmid Institute of Materials Science, Austrian Academy of Sciences, Jahnstraße 12, 8700 Leoben, Austria*

² *Institute of Physics, University of Graz, Universitätsplatz 5, 8010 Graz, Austria*

³ *Max-Planck Institut für Eisenforschung, Max-Planck Straße 1, 40237 Düsseldorf, Germany*

⁴ *Department of Materials, Royal School of Mines, Imperial College, Prince Consort Road, London SW7 2BP, UK*

⁵ *University Grenoble Alpes, CNRS, Grenoble INP, SIMaP, F-38000 Grenoble, France*

Abstract

The capability of high-pressure torsion on the preparation of supersaturated solid solutions, consisting of Cu-14Fe (wt.%), is studied. From microstructural investigations a steady state is obtained with nanocrystalline grains. The as-deformed state is analyzed with atom probe tomography, revealing an enhanced solubility and the presence of Fe-rich particles. The DC-hysteresis loop shows suppressed long range interactions in the as-deformed state and evolves towards a typical bulk hysteresis loop when annealed at 500°C. AC-susceptometry measurements of the as-deformed state reveal the presence of a superparamagnetic blocking

C. Intermixing of Fe and Cu on the atomic scale

peak, as well as a magnetic frustrated phase, whereas the transition of the latter follows the Almeida-Thouless line, coinciding with the microstructural investigations by atom probe tomography. AC-susceptometry shows that the frustrated state vanishes for annealing at 250°C.

Keywords: severe plastic deformation (SPD), high-pressure torsion, spin glass, three dimensional atom probe (3DAP), nanocrystalline materials

C.1. Introduction

Metastable solid solutions of immiscible components provide many opportunities for modifying physical properties, making them interesting for potential applications. The components forming such solid solutions should obey several conditions: they are immiscible and do not form any stable phases at thermal equilibrium. When ensuring these conditions, a continuous tunability of the mechanical and magnetic properties is possible by simply changing the composition.

Regarding magnetic properties, the binary Fe-Cu system is of particular interest, because it exhibits attractive aspects regarding cost and of course because of the well-known high magnetic moment of Fe. Several studies report on the improvement and tuning of the magnetic hysteresis by preparing such solid solutions of Fe and Cu, either by vapor deposition [1] or by mechanical alloying [2–4]. In [5], it was shown that mechanically alloyed solid solutions of Fe-Cu exhibit soft magnetic properties. The resulting coercivity can be modeled by random anisotropy, with grain sizes below the exchange length of Fe [6]. As in the regime of random anisotropy, the coercivity is proportional to the sixth power of the grain size, it is evident that the resulting magnetic properties are extremely sensitive to the method of preparation.

Apart from soft magnetic properties, the metastable Fe-Cu system exhibits also attractive magnetoresistive properties. For instance, the granular giant magnetoresistance (GMR) was measured on mechanically alloyed Fe-Cu [7–9]. Granular GMR systems require ferromagnetic particles separated from the copper matrix rather than a continuously intermixed state, whereby the resistivity can be correlated to the Fe-particle size [10], again making the effect extremely sensitive to the processing method and the involved parameters.

To benefit from the described effects on an industrial scale, it is evident that the major focus has to be directed on the method of sample preparation and on the process parameters.

Whereas vapor deposition turns out not to be feasible on larger scales, upscaling is possible for mechanical alloying, but one has to prepare a bulk sample from powder. This circumstance requires an additional process, which can also give rise to a change in the physical properties, as mentioned above. Therefore, a technique, capable of upscaling as well as to directly prepare a bulk sample is desired. This is where severe plastic deformation (SPD) [11] comes into play. SPD involves techniques like accumulative roll bonding (ARB), equal channel angular pressing (ECAP) and high-pressure torsion (HPT). All of these approaches have in common that the sample does not change its shape during deformation. Among these techniques, especially HPT is of great interest, since the deformation can be applied continuously. Thus, values in shear strain can be reached which are hardly accessible by other techniques of SPD, which gives rise to microstructural refinement and saturation [12]. Some studies already dealt with microstructural characterization of HPT-processed Fe-Cu [13, 14], but the effects described above require a certain amount of intermixing even on an atomic scale. Therefore, the microstructural investigation has now to be extended towards nano scales, thus the capability of HPT for magnetic dilution has to be addressed.

In this study, a sample consisting of Cu-14Fe (wt.%) is prepared by HPT. The focus is on the correlation of microstructural data with the magnetic properties, by combining atom probe tomography (APT) data with SQUID-magnetometry in DC- and AC-mode. As supersaturated states are known to be metastable in thermodynamic equilibrium, a subsequent annealing treatment is expected to lead to large changes in the physical properties. To reveal the evolution of the magnetic properties in particular, also annealed states are investigated in this study, to specifically tune desired magnetic properties such as coercivity.

C.2. Experimental

High purity powders (Fe: MaTeck 99.9% -100 +200 mesh, Cu: AlfaAesar 99.9% -170 +400 mesh) were mixed, with an elemental composition of 14wt.% Fe and 86wt.% Cu, corresponding to 16at.% Fe and 84at.% Cu. The powder mixture was hydrostatically compacted at room temperature, with an applied pressure of 5 GPa, in Ar-atmosphere to avoid contamination. The pre-compacted samples (diameter 8 mm, thickness ~ 0.5 mm) were exposed to HPT at 5 GPa, for 100 turns, with an applied amount of strain $\gamma \sim 3000$ at $r = 3$ mm. A detailed description of the HPT process and sample preparation can be found elsewhere [15–17]. Subsequent annealing treatments were performed in vacuum to avoid oxidation ($p \leq 10^{-3}$ mbar) at 150°C, 250°C and 500°C for 1h, followed by furnace cooling. Vickers

C. Intermixing of Fe and Cu on the atomic scale

hardness testing was carried out with a Buehler Micromet 5100 in tangential sample direction (a detailed description of the sample layout and its respective orientations is given in [16]). Analysis of the microstructural evolution was performed using a Zeiss LEO 1525 Scanning Electron Microscope (SEM) in tangential sample direction. The crystalline phases constituting the material were investigated by synchrotron X-ray diffraction experiments in transmission mode (beam energy 100 keV; beam size 0.2x0.2 mm²). The beam was oriented parallel to the samples axial direction, at a radius of $r = 3$ mm. Needle-shaped specimens for APT were prepared by the standard lift-out process [18] in a FEI Helios NanoLab 600i dual beam focused ion beam / scanning electron microscope (FIB/SEM) device. The final specimens were sharpened using annular milling at 30 kV acceleration voltage followed by a low kV milling at 5 kV acceleration voltage for 2 min to remove regions severely damaged by the implantation of energetic Ga ions. APT experiments were conducted using a LEAP 5000 XS at a temperature of 35 K or 40 K in laser pulsing mode. A pulse repetition rate of 250 kHz, a pulse energy of 25 pJ and a detection rate of 1.5% were used. The commercial software IVAS version 3.8.2 was used to reconstruct the tip volume using a radius evolution according to the voltage curve and an initial tip radius deduced from a high resolution SEM image acquired after final tip sharpening. Magnetic properties were investigated by SQUID-magnetometry (Quantum Design MPMS-XL-7) in AC- and DC-mode. Therefore, samples at $r \geq 2$ mm were cut out, with the external magnetic field pointing in axial orientation of the sample.

C.3. Results and Discussion

C.3.1. Microstructural evolution as a function of temperature

For HPT-processing, the applied shear strain γ increases with increasing radius [eq. C.1] [11], which gives rise to microstructural evolution, e.g. grain and phase refinement [12].

$$\gamma = \frac{2\pi nr}{t} \quad (\text{C.1})$$

In [eq. C.1], n denotes the number of turns and t is the sample thickness. To confirm a saturated steady state, Vickers hardness testing in the tangential direction of the sample is performed (Fig. C.1). The complex hardening behavior is typical for HPT-processed composites of immiscible components [19]. A plateau at 150 HV0.5 is observed, which arises from the formation of substructures in the individual phases [13]. As this plateau is already reached at very low strains ($\gamma \leq 1$), its transition from the undeformed state is not captured

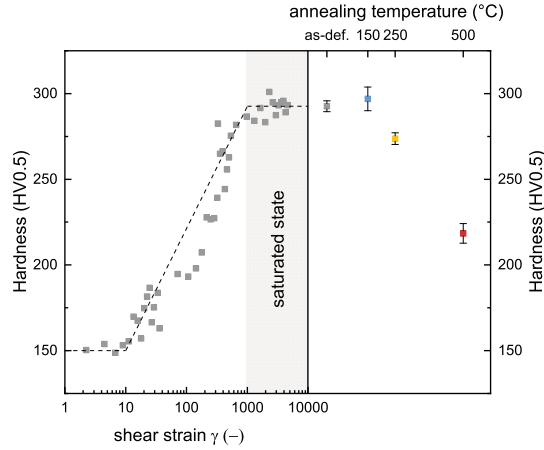


Figure C.1.: Results obtained by Vickers hardness testing in the as-deformed and annealed states. On the left side, the hardness in the as-deformed state is plotted as a function of shear strain. A saturated state is observed at $\gamma \geq 1000$. The dotted line is a guide to the eyes. On the right side the mean hardness ($\gamma \geq 1000$) is plotted as a function of annealing temperature.

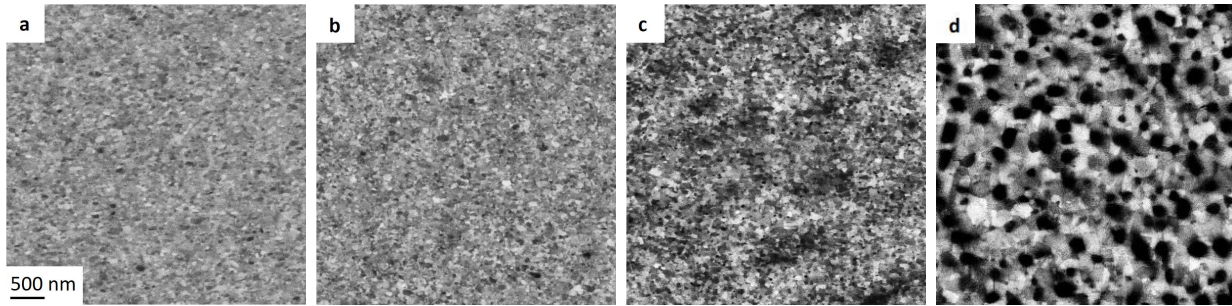


Figure C.2.: Backscattered electron SEM images, taken in tangential direction of the sample, of the as-deformed sample (a) and samples annealed at 150°C (b), 250°C (c) and 500°C (d). The radial direction is parallel to the horizontal axis. The scale bar in (a) applies to all images.

experimentally. The hardness starts to increase at $\gamma = 10$ and shows a second plateau at $\gamma \geq 1000$ and saturation. Thus, in all further measurements the sample is investigated at large radii, i.e. $r \geq 1$ mm to ensure $\gamma \geq 1000$ and therefore a saturated steady state.

Annealing at 150°C leads to a slight increase in hardness with respect to the as-deformed state, which is characteristic for nanocrystalline materials [20]. Upon annealing at higher temperatures, the hardness decreases, arising from grain growth, following the Hall-Petch relation [21, 22].

Fig. C.2 shows backscattered electron micrographs that reveal the microstructural evolution of samples in the as-deformed and annealed states at $r \geq 2$ mm. The as-deformed state (Fig. C.2a) shows a homogeneous and nanocrystalline microstructure. Neither grain growth

C. Intermixing of Fe and Cu on the atomic scale

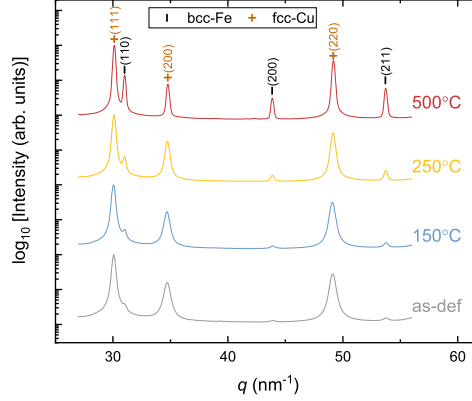


Figure C.3.: Synchrotron-XRD diffraction patterns of as-deformed and annealed samples, measured in transmission mode.

nor demixing is observed during annealing at 150°C (Fig. C.2b). The SEM image of the 250°C-annealed sample (Fig. C.2c) shows the formation of dark, Fe-rich, regions and in the SEM image of the 500°C annealed sample (Fig. C.2d), grain growth, as well as high phase contrast is observed. Synchrotron-XRD measurements reveal the evolution of crystalline phases during annealing (Fig. C.3). The pattern of the as-deformed state shows dominant fcc-Cu peaks, but also weak bcc-Fe reflections can be identified. As the intense (220) Cu-peak does not overlap with another peak, the lattice constant is calculated from the peak position to $a = 0.362$ nm, which is close to the value of pure Cu, as found in the literature ($a_{Cu,lit} = 0.3615$ nm [23]). The Fe-peaks are about two orders in magnitude smaller, and reveal, due to an extreme peak broadening, the presence of tiny residual Fe-particles. During annealing, the bcc-Fe peaks grow, indicating separated Fe and Cu phases for the 500°C-annealed sample. The peak width diminishes with annealing temperature, due to an increase in grain size.

As has been shown in several studies, HPT is capable to enhance the miscibility in the thermodynamically unstable Fe-Cu system [13, 24, 25]. The hardness measurements shown above (c.f. Fig. C.1), points also to a contribution of solid solution hardening, occurring in supersaturated systems [13]. On the other hand, XRD-measurements (c.f. Fig. C.3) show weak bcc-Fe peaks, contradicting a complete supersaturation of Fe in Cu. To investigate the grade of supersaturation in more detail, the distribution of Fe-atoms is analyzed by APT measurements. Two samples are investigated, whereas the overall compositions of the reconstructed data are determined to be Fe19.1at.-%-Cu80.8at.-% and Fe19.0at.-%-Cu80.9at.-%, respectively. In both cases the missing 0.1at.-% splits up into some residuals of H, C, O

and Ga, whereas the latter is expected to originate from FIB milling. Fig. C.4a show the APT reconstruction of a first specimen. Isosurfaces of 28.7at% Fe and 63.7at. % Cu show inhomogeneities in both, the Fe and Cu distributions. As has been proposed in Ref. [26–28], precipitates of the minority phase are likely to occur at the grain boundary. To analyze the composition at the grain boundary, its position is determined by analyzing slices of the tomographic reconstruction perpendicular to the specimen’s long axis (see appendix for more details). The grain boundary position is highlighted by the grey box in Fig. C.4a. To analyze the composition at the grain boundary, 2D-projection maps are plotted in Fig. C.4c and d, showing the distribution of Cu and Fe, respectively. The inhomogeneous distribution along the grain boundary shows distinct Cu- and Fe-enriched regions, with the Fe-composition locally rising to about 25at.%. At this point it is important to mention, that in the APT reconstruction, another Fe-rich region in the upper part of the reconstructed volume is found. In contrast, no indication of a grain boundary is found in the vicinity of this particle. Fig. C.5 shows the reconstruction of a second specimen analyzed by APT. The dashed lines indicate the positions of the grain boundaries, which have been determined in the same way as described in the appendix. Also here, Fe-rich regions are present inside the grains. The local composition of Fe-rich regions is analyzed as shown in Fig. C.5. Proxigrams [29] reveal the local concentration profiles in the proximity of the plotted isosurfaces. In Fig.C.5, proxigrams of three Fe-rich particles are displayed, showing the Fe-concentration locally rising to about 40at.%. We can therefore conclude that Fe-rich particles can be detected at grain boundaries, as well as inside the Cu-grains. Both might be responsible for the small bcc-Fe reflections in the XRD-spectrum (c.f. Fig. C.3). As several Fe-rich particles are found at the grain boundary as well as inside the grains, the amount of Fe, present in the grain (and furthermore being present in a supersaturated state), needs to be analyzed. Therefore, a cuboidal volume inside a grain is chosen to analyze the distribution of Fe. The overall composition of Fe inside the sketched box is $C=18.96\text{at.}\%$. We consider this volume, with Fe-composition C , to consist of Fe-rich precipitates with composition C_p embedded in a matrix with composition C_m . Both parameters can be evaluated by using the DIAM-algorithm, which is based on the evaluation of the first-nearest neighbor distances [30]. The matrix composition is determined to be $C_m=18.81\text{at.}\%$, showing a highly supersaturated state. When assuming the presence of clusters, which consist of pure Fe (i.e. $C_p=1$) we can estimate the minimum volume fraction of Fe-rich precipitates: $f_{V,min} = 0.19\%$ [31]. We furthermore calculate the pair correlation function (PCF), which can be used to quantify the average size of precipitates in the framework of small angle scattering [31, 32]. Fig. C.4b shows the calculated PCF. By fitting the PCF to a function describing a lognormal assembly of spheres we can determine

C. Intermixing of Fe and Cu on the atomic scale

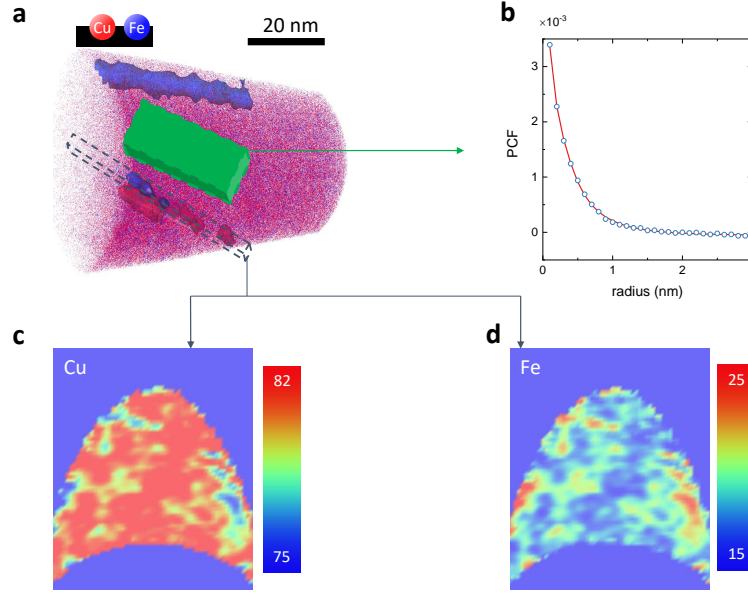


Figure C.4.: APT reconstruction of the as-deformed state. The reconstructed volume (a) consists of Fe19.1at.-%-Cu80.8at.-%. Isosurfaces of 28.7at.-% of Fe and 63.7 at.-% of Cu are displayed. (b) shows the PCF of Fe inside the green box in (a). (c) and (d) show projections of Cu and Fe, respectively, along the grain boundary in (a). The heat maps give the concentrations in at.-%.

the average particle radius from the correlation length to be 0.35 nm. This value should be taken only as an approximation, since particle sizes below 1 nm should be interpreted with caution [33], but indicates the presence of clusters consisting of several atoms. The PCF at zero distance is equal to the mean square fluctuation $(C_p - C)(C - C_m)$, but leads in the present case to $C_p \geq 100\%$. This can likely be ascribed to an artefact of the measurement, caused by the different evaporation fields of both, the precipitate and the matrix, causing local magnification and making the precipitate to appear denser [33, 34].

We can conclude that the analysis, restricted to a limited volume inside the grain, gives clear evidence of an enhanced solubility of Fe in Cu caused by HPT-processing [13, 24, 25]. Fe is found to be present either as solute and additionally, to a minimum fraction of 0.19%, as precipitate in the dimension of several atoms.

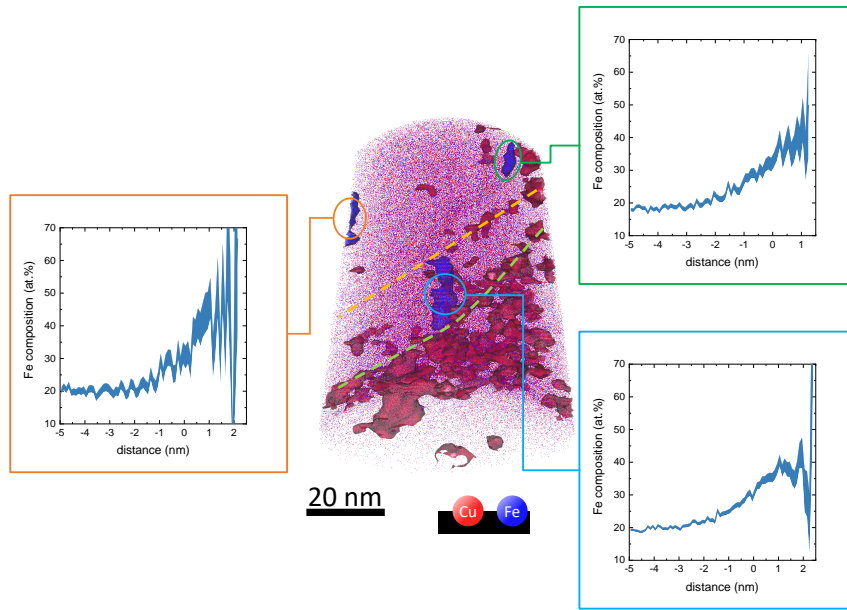


Figure C.5.: APT reconstruction of the as-deformed state. The reconstructed volume consists of Fe19.0at.%-Cu80.9at.%. Isosurfaces of 28.7at.% of Fe and 63.7 at.% of Cu are displayed. The dashed lines mark grain boundaries, which have been detected by analyzing slices of the tomographic reconstruction, as explained in the appendix. Proxigrams of Fe-rich particles show the Fe-concentration locally going up to about 40at.%.

C.3.2. Magnetic Properties

DC-magnetic properties

Figure C.6 shows the DC-magnetization versus applied magnetic field (at 300 K) of samples which were exposed to various annealing treatments. For the as-deformed and 150°C-annealed sample, a significant high-field susceptibility can be identified. This behavior indicates supersaturation of Fe in the Cu-matrix, which suppresses ferromagnetic long range interaction. A non-zero high-field susceptibility is also present in the 250°C-annealed sample, but the slope decreases with respect to the as-deformed and 150°C-annealed sample, corresponding to smaller degree of supersaturation with a concomitant initiation of segregation. The 500°C-annealed sample shows saturation at fields higher than 1 kOe, indicating a restoration of ferromagnetic long range interaction and therefore a separation of Fe and Cu. The inlay of Fig. C.6 displays the specific magnetic moment for the as-deformed state as a function of temperature, recorded at 70 kOe. Although a strong dependence on the temperature is observed, the magnetic moment, recorded at low temperatures does not coincide with the

C. Intermixing of Fe and Cu on the atomic scale

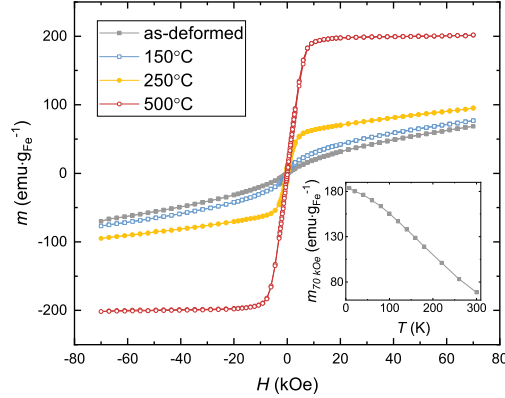


Figure C.6.: Specific Fe-magnetization m versus the applied field H for Fe14wt.%-Cu in the as-deformed and annealed states, measured at 300 K. The inlay shows the magnetic moment m , measured in the as-deformed state at 70 kOe, as a function of temperature T . The magnetic moment of bulk Fe is $218 \text{ emu}\cdot\text{g}^{-1}$ [35].

saturation magnetization of the 500°C-annealed state. This deviation is expected to arise from residual paramagnetic Fe in the as-deformed state, which does not saturate even at low temperatures. In Fig. C.7 an enlarged view of the hysteresis at low magnetic fields is displayed. The coercivity is 128 Oe in the as-deformed state and decreases to 55 Oe for the 150°C-annealed state. HPT-deformed samples exhibit large residual stresses in the as-deformed state [36] and therefore the diminishing coercivity is expected to arise from recovery effects, in particular a reduction in residual stresses upon slight annealing [5]. The 250°C-annealed state exhibits a coercivity of 358 Oe, which decreases to 60 Oe in the 500°C-annealed state, showing the crossover from the random anisotropy regime to the formation of multidomain particles [17].

Additionally, the temperature dependence of the low-field susceptibility was investigated. For zero-field cooling (ZFC) measurements the demagnetized sample is cooled in zero applied field. At the lowest temperature an external field of 50 Oe is applied and the magnetic moment is recorded during heating. In field-cooling (FC) temperature scans, the magnetic moment is measured during cooling in the same external field. In Fig. C.8, ZFC/FC-measurements are displayed. The curves are normalized to zero at 300 K, i.e. the recorded magnetic moment at 300 K is subtracted for reasons of comparability. The 500°C-annealed sample shows no splitting between the ZFC/FC-scans confirming again a reversible ferromagnetic behavior and the absence of any thermal activation below 300 K. Samples annealed below 500°C exhibit a splitting between the ZFC and FC curves, as well as broad peaks in the

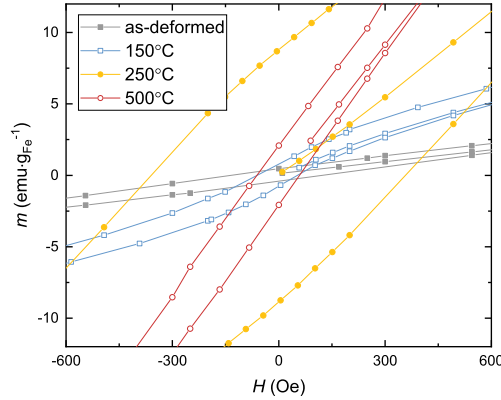


Figure C.7.: Specific magnetization m versus the applied field H for Fe14wt.%-Cu in the as-deformed and annealed states, measured at 300 K. Enlarged view of Fig. C.6.

ZFC-measurements. A local maximum is observed in the FC-curves of the as-deformed state and of the 150°C-annealed state which is characteristic for frustrated systems, rather than for thermal activation [37]. Studies on the supersaturated Fe-Cu system with low amounts of Fe report the existence of a spin-glass state [38–40].

AC-magnetic properties of as-deformed state

To analyze the origin of the observed splittings in the ZFC/FC temperature scans, AC-susceptibility measurements are carried out at different frequencies $f = 1$ Hz and $f = 100$ Hz at an AC-amplitude of 5 Oe, with DC-fields, ranging from 5 Oe up to 5000 Oe, applied. Fig. C.9 shows the results for the measurements at $f = 1$ Hz with various superimposed DC-magnetic fields. The observed maxima decrease in magnitude with increasing DC-magnetic field and shift towards lower temperature. Parts of the AC-susceptibilities, namely at $T \geq 100$ K, seem to decrease faster in magnitude, indicating a second peak, whose behavior at higher applied DC-fields is different. The same behavior is observed for measurements at $f = 100$ Hz. Fig. C.10 shows the in-phase and out-of-phase components of the measurement at $f = 1$ Hz with a superimposed magnetic field of $H = 100$ Oe. The presence of two peaks is clearly visible in the out-of-phase component and indeed, both measurements can be fitted by two lognormal distribution functions with excellent agreement. For further analysis, the in-phase components are evaluated, as these components possess 30-times higher magnitude.

The low-T peak disperses sparsely with increasing DC-field and shows a small peak shift,

C. Intermixing of Fe and Cu on the atomic scale

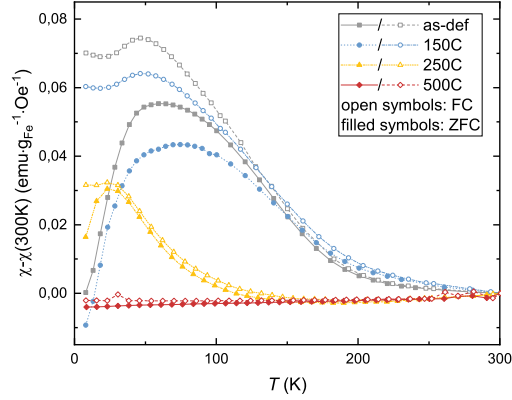


Figure C.8.: Normalized zero-field cooling and field-cooling curves of as-deformed and annealed samples as a function of annealing temperature. In all measurements a field of $H = 50$ Oe is applied. Open symbols represent FC-curves, filled symbols represent ZFC-curves.

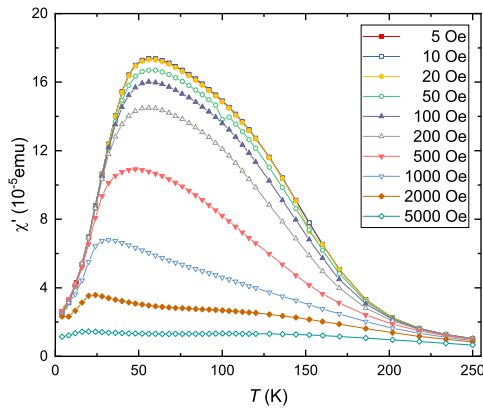


Figure C.9.: AC-susceptibility measurement in the as-deformed state with various superimposed DC-magnetic fields. Only the in-phase component χ' is shown. Measurements are taken at $f = 1$ Hz between 4 K and 250 K.

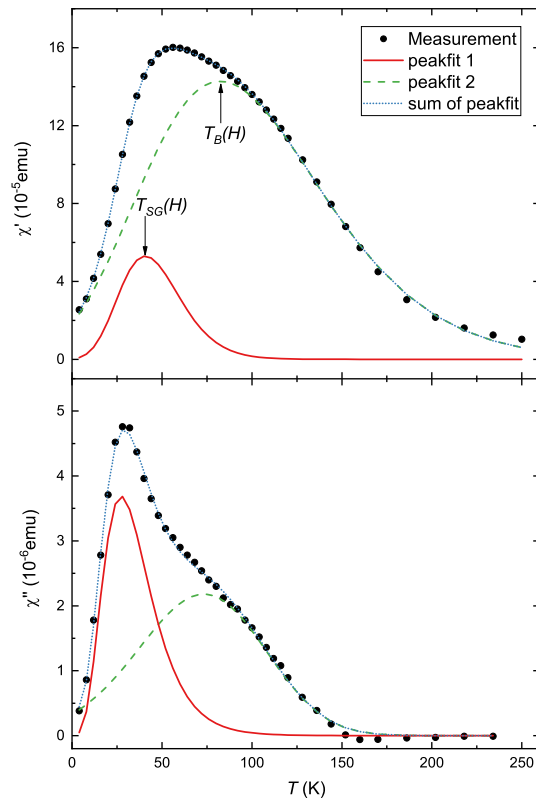


Figure C.10.: Example of an AC-susceptibility measurement in the as-deformed state, measured between 4 K and 250 K at $f = 1$ Hz. Here, a DC-magnetic field is applied ($H = 100$ Oe). The driving amplitude is 5 Oe. The presence of two different peaks is clearly visible in the out-of-phase component. Analysis was carried out by fitting the peaks with two lognormal distribution functions (solid and dashed line).

both being characteristic features for frustrated systems. Experimental evidence of such a frustrated state can be deduced from the scaling behavior of the low-temperature peak position T_{SG} for various magnetic fields. According to the theoretical Sherrington-Kirkpatrick model for spin-glass, $T_{SG}(H)$ follows the Almeida-Thouless line for not too large magnetic fields [41, 42]:

$$H = A \left(1 - \frac{T_{SG}(H)}{T_{SG}(0)} \right)^{3/2} \quad (\text{C.2})$$

In [eq. C.2], H denotes the applied DC-field and A is a constant describing either the Heisenberg or Ising universality class of the system [43, 44]. $T_{SG}(H)$ denotes the spin-glass freezing temperature as a function of H , i.e. the observed peak maximum. To prove for the Almeida-Thouless line, susceptibility measurements are carried out at various DC-fields,

C. Intermixing of Fe and Cu on the atomic scale

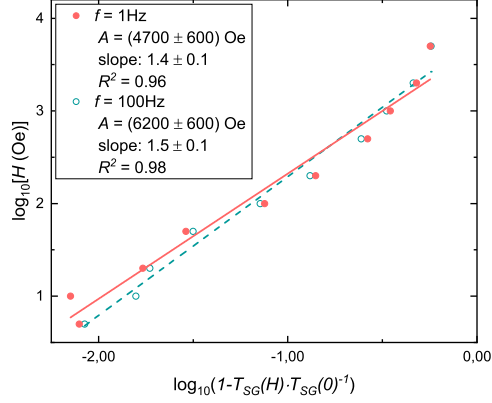


Figure C.11.: AC-susceptibility measurement of the as-deformed state at various applied DC-fields H . The peak position of the lower peak from the in-phase susceptibility is evaluated. $T_{SG}(0)$ was determined from measurements at zero applied fields to 44 K ($f=1$ Hz) and 46 K ($f = 100$ Hz). The data are in agreement with [eq. C.2].

using AC-measurements at two different frequencies ($f = 1$ Hz, 100 Hz respectively). In Fig. C.11 both, the applied DC-field H as well as the reduced temperature, are plotted in logarithmic scale for both frequencies. From a linear fit one gets the slope in agreement with the theoretically expected value of $3/2$ delivering clear evidence of the existence of a spin glass state with random dilution of the magnetic entities.

In contrast to the low-T peak, the high-T peak $T_B(H)$ disperses strongly with increasing field. This behavior is indicative to thermal activation ("magnetic blocking"). Also no proper scaling (power) law like in magnetic frustrated systems was found. For thermal activated systems anticipating mono-domain particles, the magnetic-field-dependence of the blocking temperature $T_B(H)$ can be described according to [eq. C.3a] [45].

$$T_B(H) = T_B(H=0) \cdot \left(1 - \frac{H}{H_{ani}}\right)^2 \quad (\text{C.3a})$$

$$H_{ani} = \frac{2K}{M_S} \quad (\text{C.3b})$$

H_{ani} denotes the anisotropy field, M_S is the saturation magnetization and K is the bulk magnetic anisotropy energy. The blocking temperature in absence of a DC-field $T_B(H=0)=T_B$

obeys the Arrhenius-law [eq. C.4].

$$\tau(f) = \tau_0 \exp\left(\frac{KV}{k_B T_B}\right) \quad (\text{C.4})$$

In [eq. C.4] τ_0 is the characteristic atomic precession time constant of the order 10^{-9} - 10^{-12} s, k_B is the Boltzmann constant, T_B is the blocking temperature, V is the volume of the superparamagnetic particle and $\tau(f)$ denotes the relaxation time (i.e. the inverse of the AC-fields frequency) [45]. Fig. C.12 shows the behavior of T_B , plotted versus the applied DC-field, up to $H = 500$ Oe. For higher values in H , a proper allocation of the peak maximum is hardly possible, due to an increased broadening of the peak width. T_B decreases with increasing DC-field, causing a lowering of the energy minimum for magnetization parallel to the direction of H . A least-mean square fit to [eq. C.3a] yields results for $T_B(H=0)$ and H_{ani} . The latter can be related to the magnetic saturation M_S [eq. C.3b]. Assuming the magnetic anisotropy to arise from magnetocrystalline anisotropy only ($K = K_1^{Fe} = 4.8 \cdot 10^4$ J/m³ [46]), yields $M_S = 3.4$ kG for the measurements at $f = 1$ Hz and $M_S = 3.7$ kG for the measurement at $f = 100$ Hz, leading to 220 emu·g⁻¹ and 239 emu·g⁻¹ respectively, in good agreement with the bulk saturation magnetization of Fe [35]. From $T_B(H=0)$ an average particle size can be estimated [eq. C.4], leading to 9 - 10 nm for both frequencies, when assuming $\tau_0 = 10^{-9}$ s and spherical particles.

To sum up, the described AC-magnetic measurements reveal the presence of two different magnetic phases in the as-deformed state: superparamagnetism can be attributed to residual Fe-particles. On the other hand, the magnetic frustrated phase is expected to arise from individual Fe-atoms diluted in the Cu-matrix, i.e. the supersaturated state.

AC-magnetization: characterization of annealed states

In contrast to the as-deformed and 150°C-annealed state, the FC-curve does not show a significant cusp for the 250°C-annealed state, but a splitting in the ZFC/FC remains (cf. Fig. C.8). To investigate its origin, AC-susceptibility measurements are performed between 4 K and 250 K for various frequencies $f=0.1$ Hz - 1 kHz in absence of an external field H . As mentioned above, the as-deformed sample shows solute Fe-atoms in the Cu-matrix. Therefore, the grade of supersaturation for the 250°C-annealed sample can be evaluated by testing for the dynamic scaling law [eq. C.5], which applies for spin-glasses [47, 48].

$$\tau(f) = \tau^* \left(\frac{T_0}{T_{SG}(f) - T_0} \right)^{z\nu} \quad (\text{C.5})$$

C. Intermixing of Fe and Cu on the atomic scale

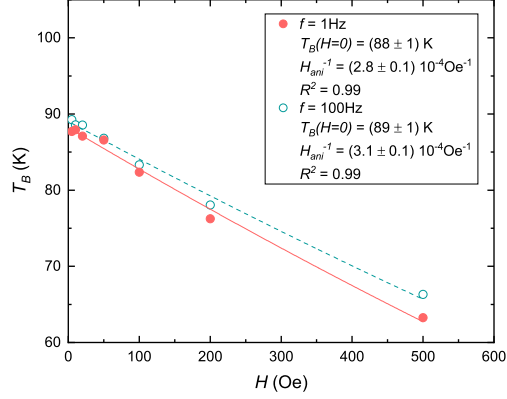


Figure C.12.: Blocking temperature T_B versus the applied DC-field H for the as-deformed state. Data deduced from AC-susceptibility measurements. The lines result from least-squares fits to [eq. C.3].

In [eq. C.5], $\tau(f)$ denotes the relaxation time, i.e. the inverse of the AC-fields frequency, τ^* is a constant, T_0 is the static freezing temperature and $T_{SG}(f)$ is the freezing temperature at a specific frequency f , i.e. temperature of the observed peak maximum in the T -scan. For spin glasses, typical values of $z\nu$ are 4 - 12 [49]. T_0 is obtained by extrapolating $T_{SG}(f)$ to $f = 0$ Hz. The data are plotted in Fig. C.13. For the as-deformed sample $z\nu = 6.0 \pm 0.8$, which denotes a spin-glass behavior, whereas for the 250°C-annealed sample the data do not scale in a proper manner. This is also reflected by the low value of fitting confidence $R^2 = 0.86$ for the latter case. The least-squares fit delivers a slope of 2.0 ± 0.5 , which does also not coincide with the expected values of $z\nu = 4 - 12$, leading to the conclusion that the spin glass behavior is not anymore dominant in the 250°C-annealed state. In contrast, the results obtained for the as-deformed sample fit quite well to the model of magnetic frustration and spin-glass behavior.

From the large coercivity in the 250°C-annealed state (cf. Fig. C.7), also the presence of larger Fe-particles is assumed in this state, which cannot be traced by AC-magnetometry [17]. Additionally, a small amount of solute, non-interacting, atomic iron clusters persists in (super)paramagnetic state, as the hysteresis loop does not saturate (cf. Fig. C.6).

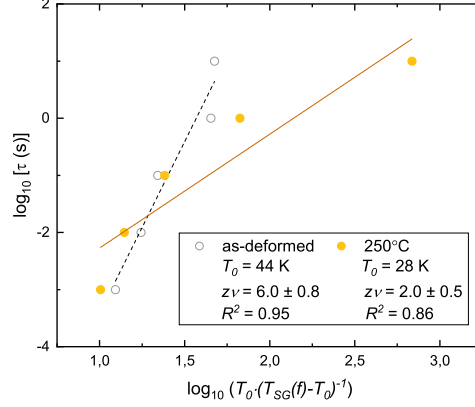


Figure C.13.: Logarithmic plot of the dynamic scaling law [eq. C.5]. Data deduced from AC-susceptibility measurements for the as-deformed and 250°C-annealed sample. T_0 was determined by extrapolating the data towards $f = 0$ Hz.

C.3.3. RKKY-interaction as origin of the magnetic frustrated phase

Magnetic frustration, as obtained with AC-magnetometry, can be attributed to randomly distributed, separated Fe-atoms, coupled via RKKY-interaction [50, 51]. Varying nearest neighbor distances give rise to either ferromagnetic or antiferromagnetic interaction ("bond-disorder"). To estimate the interatomic Fe-Fe distances, a 50x50x50 fcc-supercell is simulated (periodic boundary conditions applied), whereas 16% of all sites are randomly occupied, corresponding to the samples Fe-content (14 wt.% \equiv 16 at.%). The lattice constant of the supercell is set to 0.362 nm, as obtained by synchrotron-XRD. Evaluating the interatomic distances of the supercell leads to a mean Fe-Fe distance of $d_{Fe} = (0.27 \pm 0.04)$ nm. To calculate the RKKY-interaction [eq. C.6] only the nearest-neighbor interaction is taken into account.

$$J_{eff} = J^* \frac{\sin(\xi) - \xi \cdot \cos(\xi)}{\xi^4} \quad (\text{C.6a})$$

$$\xi = 2k_F \cdot d_{Fe} \quad (\text{C.6b})$$

In [eq. C.6], J^* is the on-site exchange constant, arising from the contact-interaction between localized Fe-spins and delocalized conduction electrons of the copper matrix. ξ is a dimensionless parameter of the Fermi wave vector k_F and the interatomic Fe distance d_{Fe} . Fig. C.14 shows a plot of the RKKY-interaction, calculated for $k_F = k_{F,Cu}$, as the matrix consists of Cu. The spread of ξ was deduced from the standard deviation of interatomic Fe-Fe distances

C. Intermixing of Fe and Cu on the atomic scale

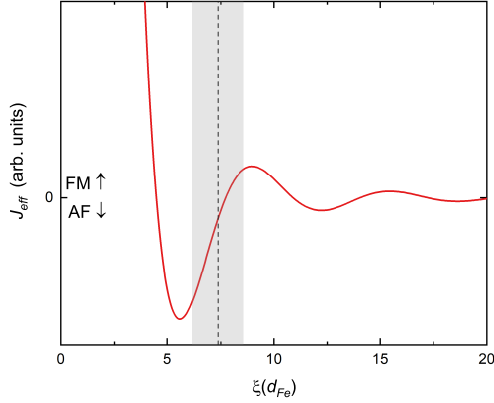


Figure C.14.: RKKY-Interaction calculated for $k_{F,Cu}$ [eq. C.6]. The dashed line represents ξ as estimated from simulation, with the shaded area being the respective standard deviation. ξ spans over a wide range, giving rise to ferromagnetic (FM) and antiferromagnetic (AF) interactions.

as calculated above. ξ spans over a wide range of J_{eff} , covering antiferromagnetic, as well as ferromagnetic interactions, capable to explain the magnetic frustration in the as-deformed state.

It should be stated that the presented model is a simple approach when comparing it to the the complex microstructure, which has been revealed by APT. The exact grades of supersaturation are expected to vary locally, but, as shown by APT, it can locally even exceed the overall Fe-content of 16at.%. Also, Fe-particles which are expected to give rise to superparamagnetism in the as-deformed state are not included. The above presented model should therefore be taken as an approximation of the real system but can sufficiently explain the origin of the magnetically frustrated phase, closely related to the enhanced grade of supersaturation caused by HPT-deformation.

C.4. Conclusion

A powder mixture of Fe and Cu is cold compacted and subsequently deformed with HPT until a saturated microstructure is generated. The grade of intermixing is investigated by correlating microstructural analysis with magnetometry. APT experiments reveal a complex microstructure in the as-deformed state. Apart from Fe-rich particles being present at the grain boundaries and inside the grains, the grains itself exhibit a larger solubility as in the thermodynamical equilibrium. The supersaturated grains are found to consist

of solute Fe as well as tiny precipitates, being a direct evidence of the capability of SPD methods to enhance the solubility limit with respect to the thermodynamical equilibrium. AC-susceptometry measurements of the as-deformed sample reveal a magnetic frustrated state, as well as thermally activated behavior. The magnetic frustrated state was proven by temperature scans as a check of the dynamic scaling law and by magnetic-field shifts following the Almeida-Thouless line and can be associated to supersaturated solid solutions of Cu-Fe. The thermal activated behavior is expected to arise from residual Fe-particles.

The frustrated and thermal activated magnetic phases persist upon annealing at 150°C, but a diminishing coercivity points out that a reduction in residual stresses takes place. The magnetic frustrated phase vanishes during annealing at 250°C. Despite, larger Fe-particles give rise to an enhancement in coercivity. The 500°C-annealed state shows a fully decomposed microstructure, with a bulk ferromagnetic behavior and the formation of multidomain particles with its typical hysteresis loop.

Acknowledgments

This project has received funding from the European Research Council (ERC) under the European Union's Horizon 2020 research and innovation programme (Grant No. 757333). Synchrotron measurements leading to these results have been performed at PETRA III: P07 at DESY Hamburg (Germany), a member of the Helmholtz Association (HGF). We gratefully acknowledge the assistance by Norbert Schell and Peter Knoll and appreciate the encouraged help with data processing by Florian Spieckermann and Christoph Gammer. The authors thank Manoel Kasalo for sample preparation. We thank Uwe Tezins, Christian Broß and Andreas Sturm for their support to the FIB and APT facilities at MPIE.

Determination of grain boundary positions

In Fig. C.15, the APT reconstruction of Cu-14Fe (wt.%) in the as-deformed state is shown, which is used to investigate the grain boundary position. The sequence of 2D-projection slices shows either distinct Cu-poles or a diffuse pattern. The Cu-poles can be attributed to a strong atomic ordering in fcc-configuration and therefore to the presence of grains. The diffuse patterns point at the presence of a grain boundary.

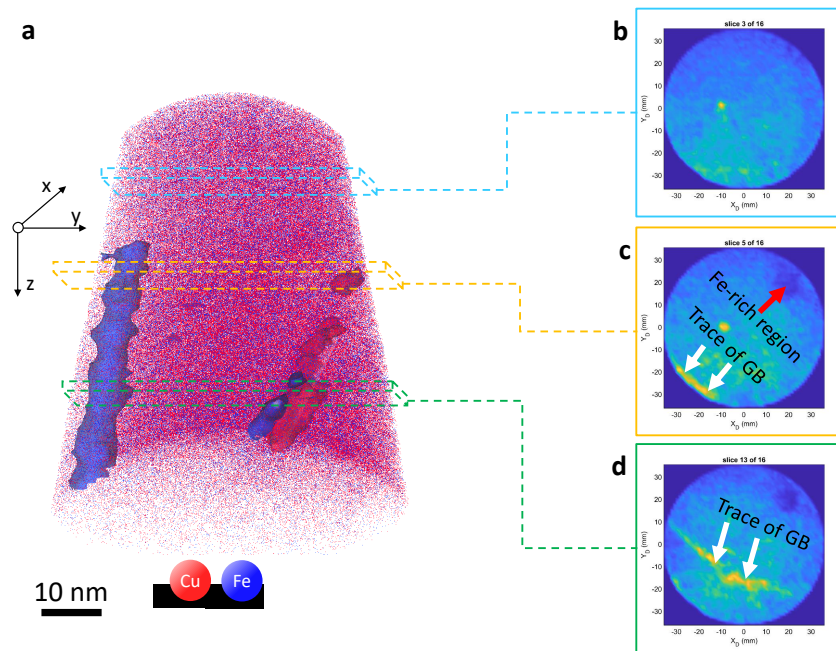


Figure C.15.: APT reconstruction of the as-deformed state. The reconstructed volume (a) consists of Fe19.1at.%-Cu80.8at.%. Isosurfaces of 28.7at.% of Fe and 63.7 at.% of Cu are displayed. Slices of the tomographic reconstruction are used to identify the position of the grain boundary. The distinct pole in (b) corresponds to a strong orientation preference and therefore the presence of a grain. In (c), apart from the pole, a diffuse pattern can be identified, indicating a grain boundary, which is also visible in (d).

C.5. References

- [1] C.L. Chien et al. “Magnetic properties of $\text{Fe}_x\text{Cu}_{100-x}$ solid solutions”. In: *Phys. Rev. B* 33.5 (1986), p. 3247. DOI: 10.1103/PhysRevB.33.3247.
- [2] P. Crespo et al. “Magnetic and structural properties of as-milled and heat-treated bcc- $\text{Fe}_{70}\text{Cu}_{30}$ alloy”. In: *J. Magn. Magn. Mater.* 150 (1995), pp. 409–416. DOI: 10.1016/0304-8853(95)00280-4.
- [3] J.Z. Jiang et al. “Magnetic properties of mechanically alloyed FeCu”. In: *J. Phys. Condens. Matter* 6.16 (1994), p. L227. DOI: 10.1088/0953-8984/6/16/002.
- [4] T. Ambrose, A. Gavrin, and C.L. Chien. “Magnetic properties of metastable fcc Fe-Cu alloys prepared by high energy ball milling”. In: *J. Magn. Magn. Mater.* 124 (1993), pp. 15–19. DOI: 10.1016/0304-8853(93)90063-8.
- [5] T.D. Shen, R.B. Schwarz, and J.D. Thompson. “Soft magnetism in mechanically alloyed nanocrystalline materials”. In: *Phys. Rev. B* 72.1 (2005), p. 014431. DOI: 10.1103/PhysRevB.72.014431.

- [6] G. Herzer. “Soft magnetic nanocrystalline materials”. In: *Scr. Mater.* 33.10-11 (1995), pp. 1741–1756. DOI: 10.1016/0956-716X(95)00397-E.
- [7] J.Q. Xiao, J.S. Jiang, and C.L. Chien. “Giant magnetoresistance in nonmultilayer magnetic systems”. In: *Phys. Rev. Lett.* 68.25 (1992), p. 3749. DOI: 10.1103/PhysRevLett.68.3749.
- [8] A.Y. Yermakov et al. “Magnetoresistance and structural state of Cu-Co, Cu-Fe compounds obtained by mechanical alloying”. In: *Mater. Sci. Forum* 225 (1996), pp. 147–156. DOI: 10.4028/www.scientific.net/MSF.225-227.147.
- [9] S. Wurster et al. “Tuneable Magneto-Resistance by Severe Plastic Deformation”. In: *Metals* 9.11 (2019). DOI: 10.3390/met9111188.
- [10] I. Ennen et al. “Giant magnetoresistance: Basic concepts, microstructure, magnetic interactions and applications”. In: *Sensors* 16.6 (2016), p. 904. DOI: 10.3390/s16060904.
- [11] R.Z. Valiev, R.K. Islamgaliev, and I.V. Alexandrov. “Bulk nanostructured materials from severe plastic deformation”. In: *Prog. Mater. Sci.* 45.2 (2000), pp. 103–189. DOI: 10.1016/S0079-6425(99)00007-9.
- [12] R. Pippan et al. “The limits of refinement by severe plastic deformation”. In: *Adv. Eng. Mater.* 8.11 (2006), pp. 1046–1056. DOI: 10.1002/adem.200600133.
- [13] K.S. Kormout, R. Pippan, and A. Bachmaier. “Deformation-induced supersaturation in immiscible material systems during high-pressure torsion”. In: *Adv. Eng. Mater.* 19.4 (2017), p. 1600675. DOI: 10.1002/adem.201600675.
- [14] A. Bachmaier et al. “The formation of supersaturated solid solutions in Fe-Cu alloys deformed by high-pressure torsion”. In: *Acta Mater.* 60.3 (2012), pp. 860–871. DOI: 10.1016/j.actamat.2011.10.044.
- [15] A. Hohenwarter et al. “Technical parameters affecting grain refinement by high pressure torsion”. In: *I. J. Mater. Res.* 100.12 (2009), pp. 1653–1661. DOI: 10.3139/146.110224.
- [16] M. Stückler et al. “Magnetic Binary Supersaturated Solid Solutions Processed by Severe Plastic Deformation”. In: *Nanomaterials* 9.1 (2018), p. 6. DOI: 10.3390/nano9010006.
- [17] M. Stückler et al. “Magnetic dilution by severe plastic deformation”. In: *AIP Adv.* 10.1 (2020), p. 015210. DOI: 10.1063/1.5128058.
- [18] D.J. Larson et al. “Local electrode atom probe tomography”. In: *New York, US: Springer Science* (2013).
- [19] K.S. Kormout et al. “Deformation mechanisms during severe plastic deformation of a CuAg composite”. In: *J. Alloys Compd.* 695 (2017), pp. 2285–2294. DOI: 10.1016/j.jallcom.2016.11.085.

- [20] O. Renk et al. “Increasing the strength of nanocrystalline steels by annealing: Is segregation necessary?” In: *Scr. Mater.* 95 (2015), pp. 27–30. DOI: 10.1016/j.scriptamat.2014.09.023.
- [21] E.O. Hall. “The deformation and ageing of mild steel: III discussion of results”. In: *Proc. Ph. Soc. London Sect. B* 64.9 (1951), p. 747. DOI: 10.1088/0370-1301/64/9/303.
- [22] N.J. Petch. “The cleavage strength of polycrystals”. In: *J. Iron Steel Inst.* 174 (1953), pp. 25–28.
- [23] G Chiarotti. “1.6 Crystal structures and bulk lattice parameters of materials quoted in the volume”. In: *Interaction of Charged Particles and Atoms with Surfaces*. Springer, 1995, pp. 21–26.
- [24] X. Queleñec et al. “Homogeneous Cu-Fe supersaturated solid solutions prepared by severe plastic deformation”. In: *Philos. Mag.* 90.9 (2010), pp. 1179–1195. DOI: 10.1080/14786430903313682.
- [25] A. Lukyanov et al. “Microstructure transformation in a cast Cu-Fe alloy at high pressure torsion deformation”. In: *Rev. Adv. Mater. Sci.* 45.1-2 (2016), pp. 20–27.
- [26] B.B. Straumal et al. “Increase of Co solubility with decreasing grain size in ZnO”. In: *Acta Mater.* 56.20 (2008), pp. 6246–6256. DOI: 10.1016/j.actamat.2008.08.032.
- [27] Y. Ivanisenko et al. “Bulk nanocrystalline ferrite stabilized through grain boundary carbon segregation”. In: *Adv. Eng. Mater.* 20.10 (2018), p. 1800443. DOI: 10.1002/adem.201800443.
- [28] A.A. Mazilkin et al. “Competition for impurity atoms between defects and solid solution during high pressure torsion”. In: *Scr. Mater.* 173 (2019), pp. 46–50. DOI: 10.1016/j.scriptamat.2019.08.001.
- [29] B. Gault et al. *Atom probe microscopy*. Vol. 160. Springer Science & Business Media, 2012.
- [30] F. De Geuser and W. Lefebvre. “Determination of matrix composition based on solute-solute nearest-neighbor distances in atom probe tomography”. In: *Microsc. Res. Tech.* 74.3 (2011), pp. 257–263. DOI: 10.1002/jemt.20899.
- [31] H. Zhao et al. “Parameter free quantitative analysis of atom probe data by correlation functions: Application to the precipitation in Al-Zn-Mg-Cu”. In: *Scripta Mater.* 154 (2018), pp. 106–110. DOI: 10.1016/j.scriptamat.2018.05.024.
- [32] L. Couturier, F. De Geuser, and A. Deschamps. “Direct comparison of Fe-Cr unmixing characterization by atom probe tomography and small angle scattering”. In: *Mater. Charact.* 121 (2016), pp. 61–67. DOI: 10.1016/j.matchar.2016.09.028.
- [33] F. De Geuser and B. Gault. “Metrology of small particles and solute clusters by atom probe tomography”. In: *Acta Mater.* 188 (2020), pp. 406–415. DOI: 10.1016/j.actamat.2020.02.023.

- [34] E. A. Marquis and F. Vurpillot. “Chromatic aberrations in the field evaporation behavior of small precipitates”. In: *Microsc. Microanal.* 14.6 (2008), p. 561. DOI: 10.1017/S1431927608080793.
- [35] B.D. Cullity and C.D. Graham. *Introduction to magnetic materials*. John Wiley & Sons, 2011.
- [36] J. Todt et al. “Gradient residual strain and stress distributions in a high pressure torsion deformed iron disk revealed by high energy X-ray diffraction”. In: *Scr. Mater.* 146 (2018), pp. 178–181. DOI: 10.1016/j.scriptamat.2017.11.037.
- [37] O. Schneeweiss et al. “Magnetic properties of the CrMnFeCoNi high-entropy alloy”. In: *Phys. Rev. B* 96.1 (2017), p. 014437. DOI: 10.1103/PhysRevB.96.014437.
- [38] A.V. Vedyayev and V. Cherenkov. “Spin Glass State in Alloys of Copper With Manganese, Iron and Cobalt”. In: *Sov. Phys. JETP-USSR* 55.2 (1982), pp. 287–290.
- [39] T. Uchiyama, M. Matsui, and K. Adachi. “Spin glass of liquid-quenched CuFe alloys”. In: *IEEE Trans. Magn.* 23.5 (1987), pp. 2305–2307. DOI: 10.1109/TMAG.1987.1065365.
- [40] C.L. Chien et al. “Magnetic percolation in new crystalline FCC Fe-Cu alloys”. In: *Mater. Res. Soc. Symp. Proc.* 80 (1986). DOI: 10.1557/PROC-80-395.
- [41] D. Sherrington and S. Kirkpatrick. “Solvable model of a spin-glass”. In: *Phys. Rev. Lett.* 35.26 (1975), p. 1792. DOI: 10.1103/PhysRevLett.35.1792.
- [42] J.R.L. De Almeida and D.J. Thouless. “Stability of the Sherrington-Kirkpatrick solution of a spin glass model”. In: *J. Phys. A* 11.5 (1978), p. 983. DOI: 10.1088/0305-4470/11/5/028.
- [43] H. Aruga Katori and A. Ito. “Experimental study of the de Almeida-Thouless line by using typical Ising spin-glass $\text{Fe}_x\text{Mn}_{1-x}\text{TiO}_3$ with $x=0.41, 0.50, 0.55$ and 0.57 ”. In: *J. Phys. Soc. Jpn.* 63.8 (1994), pp. 3122–3128. DOI: 10.1143/JPSJ.63.3122.
- [44] A. Sharma and A.P. Young. “de Almeida–Thouless line in vector spin glasses”. In: *Phys. Rev. E* 81.6 (2010), p. 061115. DOI: 10.1103/PhysRevE.81.061115.
- [45] M. Knobel et al. “Superparamagnetism and other magnetic features in granular materials: a review on ideal and real systems”. In: *J. Nanosci. Nanotechnology* 8.6 (2008), pp. 2836–2857. DOI: 10.1166/jnn.2008.15348.
- [46] H. Gengnagel and U. Hofmann. “Temperature Dependence of the Magnetocrystalline Energy Constants K_1, K_2 , and K_3 of Iron”. In: *Phys. Status Solidi* 29.1 (1968), pp. 91–97. DOI: 10.1002/pssb.19680290109.
- [47] M. Balanda. “AC susceptibility studies of phase transitions and magnetic relaxation: conventional, molecular and low-dimensional magnets”. In: *Acta Phys. Pol. A* 124.6 (2013), pp. 964–976. DOI: 10.12693/APhysPolA.124.964.

- [48] F. Zeb et al. “Surface spin-glass in cobalt ferrite nanoparticles dispersed in silica matrix”. In: *J. Magn. Magn. Mater.* 407 (2016), pp. 241–246. DOI: 10.1016/j.jmmm.2016.01.084.
- [49] A. Arauzo et al. “Spin-glass behavior in single crystals of hetero-metallic magnetic warwickites MgFeBO₄, Mg_{0.5}Co_{0.5}FeBO₄, and CoFeBO₄”. In: *J. Magn. Magn. Mater.* 392 (2015), pp. 114–125. DOI: 10.1016/j.jmmm.2015.05.006.
- [50] K. Binder and A.P. Young. “Spin glasses: Experimental facts, theoretical concepts, and open questions”. In: *Rev. Mod. Phys.* 58.4 (1986), p. 801. DOI: 10.1103/RevModPhys.58.801.
- [51] J.M. Franz and D.J. Sellmyer. “Magnetic Interactions and High-Field Magnetization in Dilute Magnetic Alloys”. In: *Phys. Rev. B* 8.5 (1973). DOI: 10.1103/PhysRevB.8.2083.

D. On the magnetic nanostructure of a Co-Cu alloy processed by high-pressure torsion

Martin Stücker¹, Christian Teichert², Aleksandar Matković², Heinz Krenn³, Lukas Weissitsch¹, Stefan Wurster¹, Reinhard Pippan¹ and Andrea Bachmaier¹

¹ *Erich Schmid Institute of Materials Science, Austrian Academy of Sciences, Jahnstraße 12, 8700 Leoben, Austria*

² *Institute of Physics, Montanuniversität Leoben, Franz-Josef-Straße 18, 8700 Leoben, Austria*

³ *Institute of Physics, University of Graz, Universitätsplatz 5, 8010 Graz, Austria*

Abstract

In this study, a preparation route of Co-Cu alloys with soft magnetic properties by high-pressure torsion deformation is introduced. Nanocrystalline, supersaturated single-phase microstructures are obtained after deformation of Co-Cu alloys, which are prepared from an initial powder mixture with Co-contents above 70 wt.%. Isochronal annealing treatments up to 400°C further reveal a remarkable microstructural stability. Only at 600°C, the supersaturated phase decomposes into two fcc-phases. The coercivity, measured by SQUID as a function of annealing temperature, remains significantly below the value for bulk-Co in all states investigated. In order to understand the measured magnetic properties in detail, a quantitative analysis of the magnetic microstructure is carried out by magnetic force microscopy and correlated to the observed changes in coercivity. Our results show that the rising coercivity can be explained by a magnetic hardening effect occurring in context with spinodal decomposition.

Keywords: severe plastic deformation (SPD), high-pressure torsion, supersaturation, magnetic force microscopy (MFM), nanocrystalline

D.1. Introduction

Desirable magnetic properties have frequently been attributed to the nanocrystalline regime [1, 2]. Nanocrystalline soft magnetic materials are already commercially produced, in particular by melt spinning, yielding amorphous sheets. In additional processing steps, these sheets are stacked and exposed to annealing treatments to adjust the grain size, further tuning the magnetic properties such as saturation magnetization, coercivity, and permeability [3, 4]. In contrast to this type of material synthesis, also known as bottom-up approach, the production of such nanocrystalline magnetic materials starting with coarse grained materials (top-down approach) has gained attraction recently [5, 6]. The advantage is obvious: additional processing steps, such as stacking of sheets can be omitted. Furthermore, (expensive) rare-earth elements, necessary for metallic glass formation, can be neglected. For the top-down approach, high-pressure torsion (HPT) is an attractive technique, as the prepared samples are already present in bulk form. Moreover, with this technique the microstructure can be tuned while the sample retains its shape during preparation. Being a technique of severe plastic deformation (SPD), HPT exhibits the advantage that the applied shear deformation can act continuously, i.e., any desirable amount of deformation can be applied [7]. This deformation can cause grain refinement with the possibility of attaining the regime of nanocrystallinity [8]. Metastable phases can form during HPT-deformation, and may be retained even after pressure release [9]. Starting with conventional powders, any chemical composition can be investigated by HPT. In particular, Co-based materials have raised interest due to their low magnetostriction, favoring soft magnetic properties [1, 10]. Studies dealing with the immiscible Co-Cu system have demonstrated that single phase supersaturated solid solutions can be prepared by HPT [11], whereas higher Co-contents yield better soft magnetic properties [12]. As recent studies reported on failing synthesis by HPT for Co-contents above 67 wt.% [12], the scope of the current study is to establish a promising sample preparation route for high Co-contents yielding a single phase supersaturated solid solution. The magnetic properties of supersaturated solid solutions are highly sensitive to temperature [13]. Therefore, in this study an in-depth characterization of the temperature stability and its influence on the magnetic properties is carried out.

D.2. Experimental

Conventional powders (Co: Alfa Aesar, -22 mesh, Puratronic[®], 99.998%; Cu: Alfa Aesar, -170+400 mesh, 99.9%) were mixed to a desired composition and hydrostatically consolidated in

Ar-atmosphere. The resulting coin-shaped specimen (diameter: 8 mm; thickness: 1 mm) was exposed to SPD by HPT at temperatures between ambient conditions and 500°C (facilitated by inductive heating of the anvils) [8]. During HPT, a pressure of 5 GPa was applied, while using a rotational speed of 1.28 min⁻¹. To ensure a microstructural steady state, 50-150 numbers of turns were chosen, corresponding to a shear strain of about 1000-3000 at a radius of 3 mm. Subsequently, isochronal annealing treatments were performed in a conventional furnace for 1 h each, followed by a quick cooling in air. Vickers microhardness was measured with a used load of 500 g (HV0.5; Buehler Micromet 5100). The microstructure was investigated using scanning electron microscopy (SEM; Zeiss LEO1525). An attached energy dispersive X-ray spectrometer (EDS; Bruker e⁻-Flash) was used to measure the samples' chemical compositions, which are given in weight percent (wt.%) herein. The crystallographic states were characterized using X-ray diffraction (Bruker D2 Phaser) using Co-K_α radiation. DC-hysteresis measurements were performed with a SQUID-magnetometer (Quantum Design MPMS-XL 7) at 300 K and 8 K. Magnetic force microscopy (MFM) measurements were carried out using a Horiba France SmartSPM in two-pass mode at lift-heights between 10 nm and 20 nm using hard magnetically coated tips (coercivity 15 Oe) exhibiting tip radii of ≤15 nm (NANOSENSORSTM SSS-MFMR). For MFM measurements, sample and tip were put on the same potential, eliminating electrostatic interaction. Topographic as well as MFM scans are visualized and processed with the software Gwyddion 2.53. Topographic scans are corrected by mean plane subtraction as well as by aligning rows. In case of MFM scans, data are analyzed as measured.

D.3. Results and Discussion

D.3.1. Sample synthesis with high Co-content

As has recently been reported in [12], single-phase Co-Cu samples can be prepared for intermediate Co-contents (28 wt.% - 67 wt.%) by HPT at room temperature, yielding bulk samples with grain sizes in the nanocrystalline regime (77 nm-100 nm [12]). Using the same processing parameters, sample preparation with higher Co-contents (> 67 wt.%) fails due to crack formation. To obtain the desired single phase nanocrystalline microstructure at higher Co-contents, the sample synthesis is improved as presented in the following method.

The initial powders used in this study are shown in Fig. D.1(a),(b). The morphology of the Cu-powder (Fig. D.1(a)) appears globular, whereas the Co-powder (Fig. D.1(b)) shows

D. On the magnetic nanostructure of a Co-Cu alloy processed by high-pressure torsion

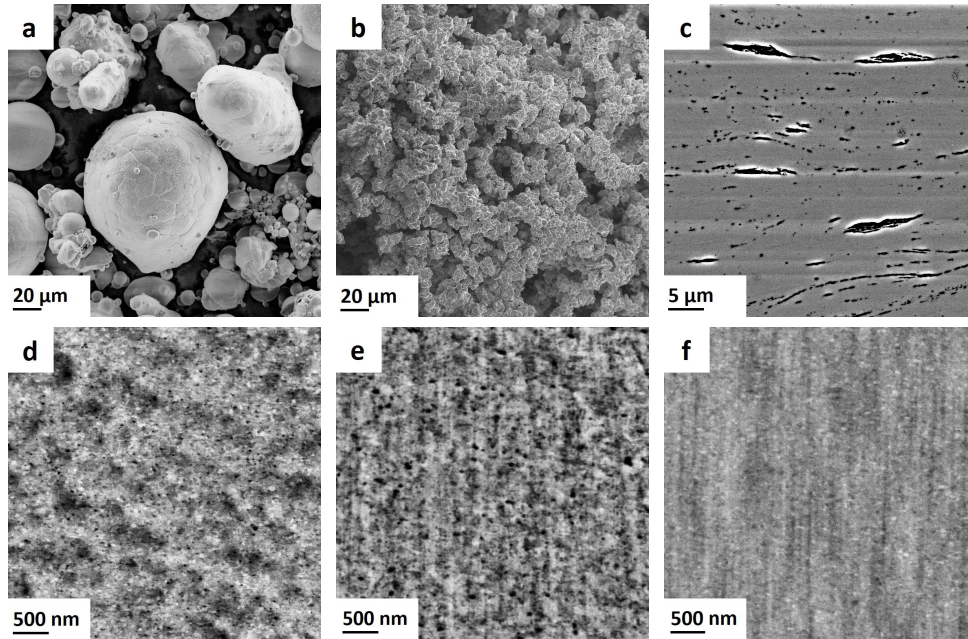


Figure D.1.: SEM micrographs: (a) and (b) show the initial Cu and Co powders, respectively. (c) shows a HPT-sample deformed at RT (100 turns) consisting of Co78-Cu22 (wt.%). (d) and (e) show Co78-Cu22 deformed at 300°C (100 turns) and Co93-Cu7 deformed at 500°C (50 turns) respectively. (f) shows a sample consisting of Co88-Cu12, which was exposed to a two-step deformation process at 500°C (50 turns) and RT (50 turns). Micrographs of HPT samples are taken in tangential direction at a radius of 3 mm. Please note the different scale bars.

many tiny particles agglomerating to structures with large surfaces. Room temperature deformation of Cu mixed with Co-powder shows abrasion of the harder (dark) Co particles (Fig. D.1(c)) which is considered as an intermediate stage in the formation of supersaturated solid solutions [14], but the formation of cracks impedes further deformation. To overcome the crack formation limiting the development of a homogeneous microstructure, the idea is to generate the desired microstructure by two consecutive steps of HPT deformation: in the first step, HPT deformation is performed at elevated temperatures, avoiding crack formation, and generating an ultra-fine grained structure at enhanced homogeneity. In the second step, the same sample is exposed to HPT-deformation at room temperature, yielding the desired, nanocrystalline microstructure.

Fig. D.1(d) shows an SEM micrograph of Co78-Cu22 deformed at 300°C for 100 turns yielding a homogeneous deformation with a complete absence of cracks. Homogeneous deformation is also reached for even higher Co-concentrations: Fig. D.1(e) shows Co93-Cu7 deformed at 500°C (50 turns). Although the deformation at elevated temperatures yields homogenization of strain distribution darker and brighter regions in the sub- μm regime are

observed in the micrographs fig. D.1(d) and (e). Therefore, a homogeneous supersaturation is not yet reached. As the scope of this study is to reach nanocrystalline grain sizes while maintaining a high chemical homogeneity, a subsequent HPT-deformation step at lower temperatures (e.g., room temperature) is expected to yield the desired microstructure. Fig. D.1(f) shows a micrograph of a sample consisting of Co₈₈-Cu₁₂ deformed at 500°C (50 turns), which was subsequently exposed to an additional deformation step at room temperature (50 turns). The resulting microstructure exhibits enhanced chemical homogeneity and furthermore a smaller grain size, in comparison to Fig. D.1(e). As has been reported in the literature, the steady state grain size is a function of temperature [15], which has been recently attributed to the deformation temperature dependent mobility of triple junctions [16].

D.3.2. Investigations on the thermal stability

Nanocrystalline materials are often prone to grain growth at low homologous temperatures [1], causing the loss of the initial superior magnetic properties [3, 4]. The thermal stability can be reduced further by a positive heat of mixing, as it is the case for the presented Co-Cu samples [11]. Therefore, a detailed investigation of the thermal stability of a Co₇₂-Cu₂₈ (wt.%) alloy is carried out in the following, serving as an example of the Co-Cu alloys described above. The presented sample was prepared by a two-step HPT deformation process, where the first step is performed at 300°C (100 turns) and the second step is performed at room temperature (50 turns).

Microstructural characterization

Figure D.2(a) shows the micrograph of a sample consisting of Co₇₂-Cu₂₈ in the as-deformed state. In comparison to the sample, which has been exposed only to deformation at 300°C (c.f. Fig. D.1(d)), the microstructure reveals an enhanced chemical homogeneity, as well as reduced grain size. The micrographs in Fig. D.2(b)-(e) show the sample annealed at temperatures of 150°C, 300°C, 400°C and 600°, for 1 h each. From these images, no grain growth can be observed, but chemical contrast forms slightly, indicating separation of the chemical phases for annealing treatments up to 400°C (Fig. D.2(b)-(d)). A considerable phase contrast as well as significant larger grain sizes can be observed for an annealing treatment at 600°C (Fig. D.2(e)). Mechanical properties are very sensitive to the microstructure. Therefore, Vickers-hardness is measured as a function of annealing temperature. The mean values of several measurements

D. On the magnetic nanostructure of a Co-Cu alloy processed by high-pressure torsion

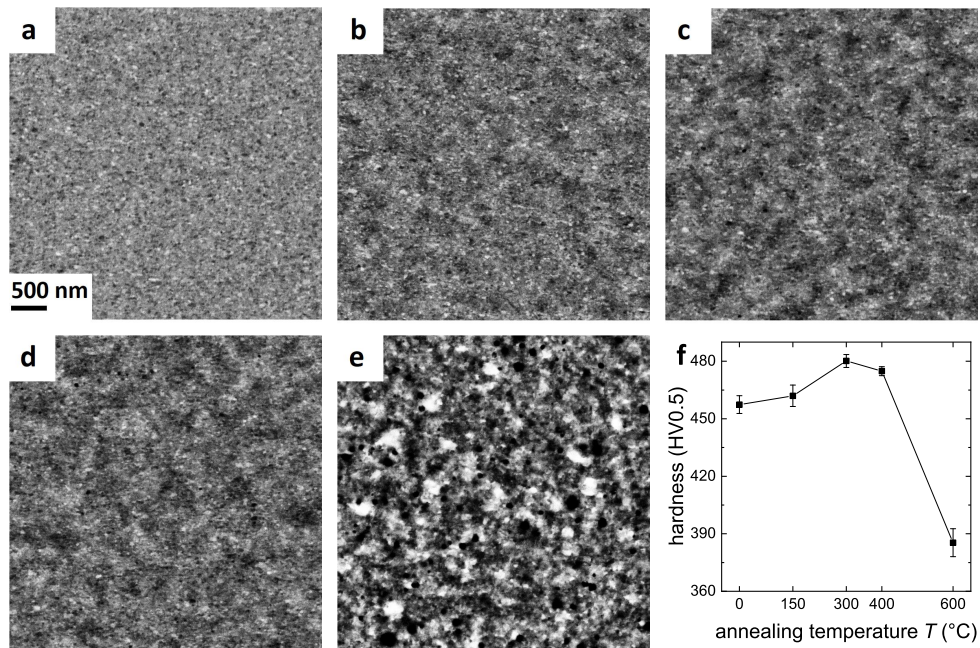


Figure D.2.: SEM micrographs of (a) Co72-Cu28 (wt.%) processed by a two-step deformation process at 300°C (100 turns) and subsequently at RT (50 turns). The sample in (a) has been exposed to subsequent annealing treatments at 150°C (b), 300°C (c), 400°C (d) and 600°C (e). The scale bar in (a) applies to all micrographs. Images are taken in BSE-mode in the tangential direction. (f) shows the hardness as a function of annealing temperature.

between radii r , of 2 mm and 3.5 mm (according to an average of the HPT strain status) are plotted in Fig. D.2(f). Due to the nanocrystalline grain size as well as solid solution hardening, the hardness in the as-deformed state is enhanced with respect to the coarse grained and pure phase materials. An increasing hardness is observed for annealing treatments up to 400°C, which is a common behavior for nanocrystalline materials, for details see [17]. The 600°C-annealed state shows the lowest hardness among all measured values, which can be explained by the largest grain size as well as by the reduction or absence of solid solution hardening.

XRD-measurements are presented in Fig. D.3. In the as-deformed state, only one set of fcc-peaks is visible, showing a single-phase solid solution. Apart from slightly diminishing FWHM, no significant change in the XRD spectra can be observed for annealing treatments up to 400°C. A splitting into two sets of fcc-peaks is found for annealing at 600°C coinciding with the microstructure obtained by SEM (c.f. Fig. D.2(e)). From the XRD-pattern, the lattice constants are evaluated. To compensate for experimental errors, the Nelson-Riley

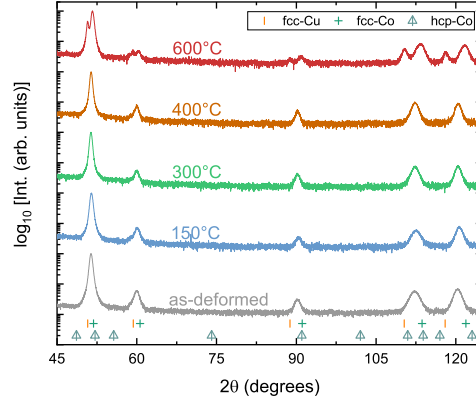


Figure D.3.: XRD-pattern (Co- K_{α} radiation) of Co72-Cu28 (wt.%) exposed to different subsequent annealing treatments (c.f. Fig. D.2). Peak positions of fcc-Cu, fcc-Co and hcp-Co are indicated below the spectra.

function is used for a precise evaluation of the lattice constants [18].

$$\frac{\Delta a}{a} \propto \frac{\cos^2 \theta}{\sin \theta} + \frac{\cos^2 \theta}{\theta} \quad (\text{D.1})$$

[Eq. (D.1)] is used for evaluating the lattice constant a , with θ being the diffraction angle of the maxima. The y-intercept of a linear regression represents $\Delta a = 0$ and leads to a precise determination in a . The resulting lattice constants are displayed in Fig. D.4, showing slight changes for annealing treatments up to 400°C, arising most likely from compositional fluctuations in powder metallurgical sample preparation. At 600°C, two different fcc-phases are identified, with the lattice constants being very close to the pure elements. However, it can not be concluded that both phases are chemically pure, i.e, some small amounts of Co might persist in the Cu-phase and vice versa. Furthermore, the Co-contents x_{Co} (at.%) are calculated for each a according to Vegard's law [19].

$$a = x_{Co} \cdot a_{Co} + (1 - x_{Co}) \cdot a_{Cu} \quad (\text{D.2})$$

For the above estimation of Co-contents, the lattice constant are taken as in the following: $a_{Cu} = 3.615 \text{ \AA}$, $a_{Co} = 3.544 \text{ \AA}$. In Fig. D.4, the Co-contents according to Vegard's law are indicated.

Although the single-phase nanocrystalline microstructure was determined to be stable up to 400°C, it should be stated, that this value might not be achieved for different Co-Cu ratios.

D. On the magnetic nanostructure of a Co-Cu alloy processed by high-pressure torsion

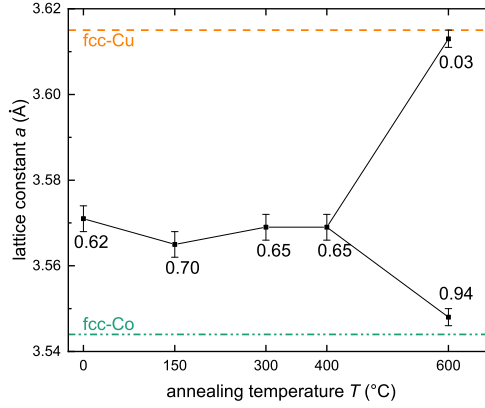


Figure D.4: Lattice constants as evaluated with the Nelson-Riley function [eq. (D.1)] from XRD-patterns. The Co-content (at.%) is calculated using Vegard's law for each lattice constant (orange dashed line: $a_{Cu} = 3.615 \text{ \AA}$, green dashed line: $a_{Co} = 3.544 \text{ \AA}$).

Actually, in several studies dealing with SPD-processed materials the temperature limit for single phase supersaturated microstructures was reported to be extremely sensitive to the particular composition investigated [9, 20].

DC-magnetic properties

In [12], it has been proposed that an increasing Co-content yields higher saturation magnetization as well as lower coercivity. To examine this presumption, hysteresis measurements using SQUID are performed at 300 K and 8 K between -7 T and $+7 \text{ T}$. DC-hysteresis curves are shown in Fig. S.2. The approach to saturation magnetization is monitored by plotting the mass magnetization σ versus the inverse external field H^{-1} between 2 T and 7 T, whereas the y-intercept of a linear regression yields σ_{SAT} at $H = \infty$, i.e., the saturation mass magnetization, which is plotted in Fig. D.5. The positive as well as the negative saturation magnetization is evaluated. Fig. D.5 shows changes in σ_{SAT} upon annealing. It is known that the magnetic moment of fcc-Co ($166.1 \text{ emu}\cdot\text{g}^{-1}$) deviates from the magnetic moment of hcp-Co ($162.5 \text{ emu}\cdot\text{g}^{-1}$). As revealed in the XRD-pattern (c.f. Fig. D.3), Co is present in an fcc configuration in all investigated states. It is therefore more likely that the observed changes in σ_{SAT} up to an annealing temperature of $400 \text{ }^\circ\text{C}$ arise from compositional fluctuations, which can be also seen in the XRD-pattern to some extent and are a common problem in powder metallurgy. A change in σ_{SAT} between 400°C and 600°C can be attributed to chemical demixing, as the supersaturated Co-Cu phase exhibits a suppressed magnetic

moment [21]. Assuming the magnetic moment for fcc-Co to be $166.1 \text{ emu}\cdot\text{g}^{-1}$ an evaluation of the mean Co-content from σ_{SAT} yields $71 \pm 1 \text{ wt.}\%$. This is in good accordance with the results from XRD-measurements, taking into account the completely different approaches for these quantification methods.

For an enhanced resolution in the determination of the coercivity H_C , hysteresis loops are measured at 8 K. It should be stated that errors in the applied H -field lead to a deviation in the determination of H_C . But as this is a reversible artifact [22], the relative evolution of H_C is unaffected. H_C as determined from hysteresis measurements is also plotted in Fig. D.5 for all measured states. H_C increases with increasing annealing temperature, in contrast to the classical assumption that large grain sizes (possessing multidomain structure) favor soft magnetic properties. The observed behavior of H_C corresponds rather to random anisotropy [4, 23]. However, it should be noted that a prerequisite for random anisotropy is for the magnetic exchange length to exceed the grain size, which seems not to be the case when referring to micromagnetic constants of bulk-Co. Another important aspect is the huge change in coercivity between the initial powder and the as-deformed state. H_C of the initial powder is also not reached for annealing treatments at 600°C , revealing the strong influence of the microstructure on the coercivity. Furthermore, a reduced magnetocrystalline anisotropy is assumed for fcc-Co in comparison to hcp-Co, which is present in the initial powder [24]. Yet the mentioned points do not suffice to quantitatively describe the observed changes in H_C . A similar temperature behavior of the coercivity has also been reported for SPD-processed Co26-Cu74 (at.%) [13], but in contrast, in the present study a significantly smaller coercivity is measured and no indications of dilute ferromagnetic phase nor superparamagnetism were found. This is most likely due to the enhanced Co-content in our study forming percolating ferromagnetic structures rather than isolated clusters.

Magnetic force microscopy

For an in-depth understanding of the observed DC-magnetic properties, a quantitative analysis of the magnetic microstructure is carried out. MFM measurements are performed in two-pass intermittent-contact (tapping) mode, i.e., in the first pass the topography is measured, whereas in the second pass the magnetic stray field is measured by keeping the tip-to-sample distance constant at an increased lift-height to minimize short-range interactions contribution in the phase lag of the cantilever oscillations in the second pass, i.e., to measure mainly magnetic force contribution to the phase lag of the cantilever in the second pass. The magnetic microstructure is measured in axial sample direction. Fig.

D. On the magnetic nanostructure of a Co-Cu alloy processed by high-pressure torsion

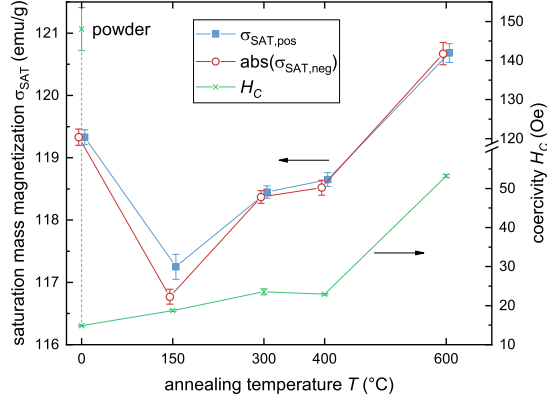


Figure D.5.: Saturation mass magnetization σ_{SAT} (at 300 K) and coercivity H_C (at 8 K) evaluated as a function of annealing temperature. The data are slightly shifted in x for better visibility. The saturation magnetization of fcc-Co is $166.1 \text{ emu} \cdot \text{g}^{-1}$. The coercivity of the initial Co-powder is also indicated. Note the break in the right y-axis.

D.6 shows representative topography and MFM measurements of the as-deformed and the 300°C annealed state. The topography (Fig. D.6(a),(c)) appears very smooth in both states and does not show any correlation to its respective MFM scan (Fig. D.6(b),(d)). An irregular appearance of the domains is visible in both MFM measurements, most likely arising from sample synthesis by SPD causing residual stresses [25]. The domain sizes are in the range of 100 nm corresponding to the grain size in the as-deformed state [12], indicating single-domain behavior. To qualitatively characterize the morphology and magnetic domain sizes for each annealing temperature, we employ the following procedure which has been introduced for a comprehensive surface roughness characterization [26, 27] but can also be applied to the MFM signal [28]. This procedure considers so-called auto-correlation and height-height correlation functions [26]. For isotropic samples as in our case it is sufficient to perform a one-dimensional analysis. The auto-correlation function $C(x)$ is calculated for each scan line of the image [26].

$$C(x) = \langle [z(x_0 + x) - \langle z \rangle][z(x_0) - \langle z \rangle] \rangle \quad (\text{D.3})$$

where z stands either for the height in nm or the phase signal of the MFM image in degrees. For a self-affine surface with a cut-off [26, 27] $C(x)$ can be described by

$$C(x) = \sigma^2 \cdot \exp[-(|x|/\xi)^{2\alpha}] \quad (\text{D.4})$$

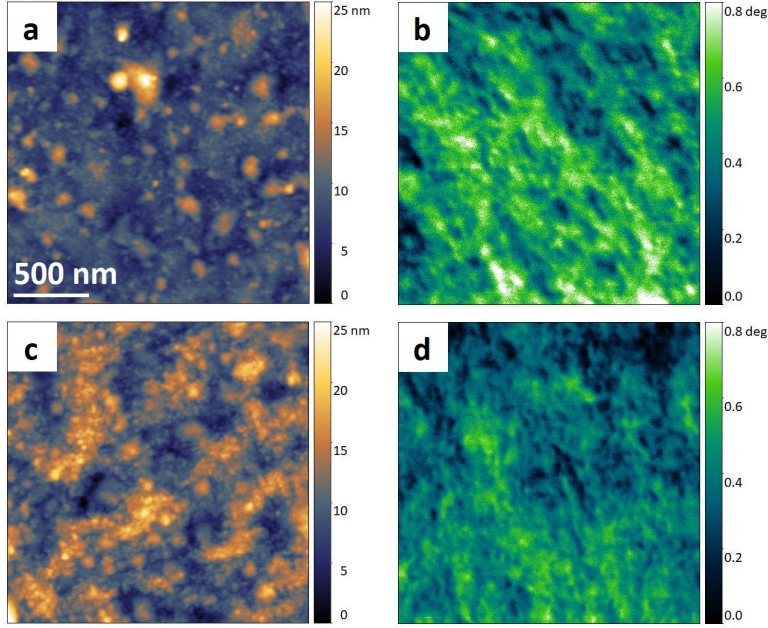


Figure D.6.: $2\mu\text{m} \times 2\mu\text{m}$ AFM scans of (a) as-deformed state and (c) 300°C annealed state. The corresponding MFM scans of the as-deformed and 300°C annealed state are shown in (b) and (d) respectively. The axial direction of the HPT specimen points out of the plane, the shear direction is in horizontal direction. The lateral scale bar in (a) applies to all scans. The minimum height and phase signal values are shifted to zero for visualization purposes.

with σ being the root mean square roughness (for MFM σ represents the standard deviation of the average magnetic signal which is related to the out-of-plane magnetization contrast). ξ represents the lateral correlation length, i.e., the length scale within the height or the MFM signal of two points correlate. The Hurst parameter α represents the “jaggedness” of the surface or the magnetic signal and ranges from 0 to 1, where small values in α represent sudden fluctuations in height. Another function describing surface statistics is the height-height correlation function $H(x)$ [26].

$$H(x) = \langle [z(x_0 + x) - z(x_0)]^2 \rangle \quad (\text{D.5})$$

with the asymptotic behavior

$$H(x) = x^{2\alpha} \text{ for } x \ll \xi \quad (\text{D.6})$$

In the following, both the auto-correlation function and the height-height correlation function are calculated for the MFM scans [28]. To disentangle the magnetic information from topography, these functions are also evaluated for the topographic (first-pass) scans. At least 6 individual scans are evaluated for each state to enhance statistical significance.

D. On the magnetic nanostructure of a Co-Cu alloy processed by high-pressure torsion

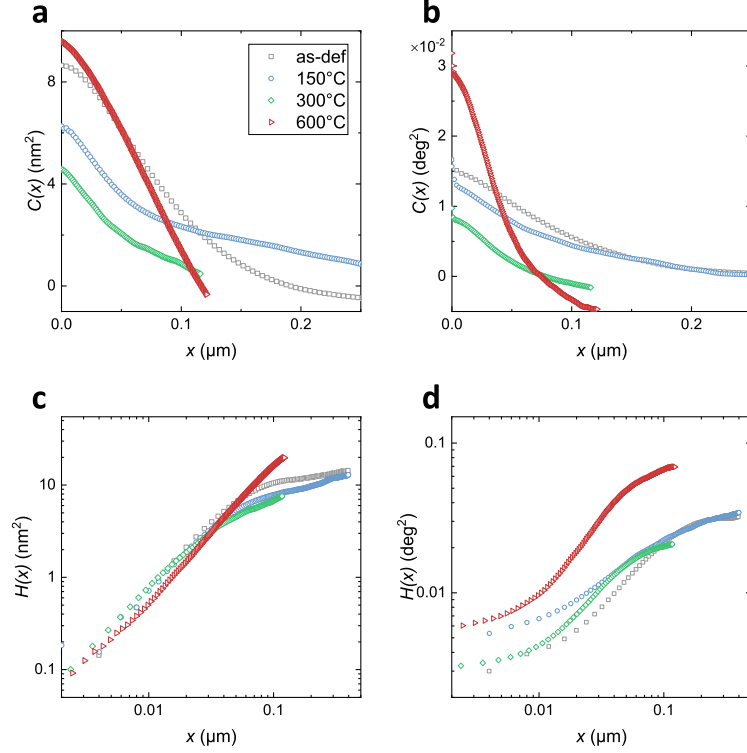


Figure D.7.: Quantitative analysis of AFM and MFM-scans. (a) and (b) shows auto-correlation functions $C(x)$ [eq. D.3] of topographic scans and MFM scans respectively. (c) and (d) shows height-height correlation functions $H(x)$ [eq. D.5] of topographic scans and MFM scans respectively.

Fig. D.7 shows representative $C(x)$ and the $H(x)$ curves evaluated for the the topographic signal and MFM signal. Note that the data are plotted in the statistically significant range for small values in x . Different shapes can be identified in the presented $C(x)$. In contrast to the topographic $H(x)$ (Fig. D.7(c)), two slopes can be identified in magnetic $H(x)$ (Fig. D.7(d)), representing a multi-fractal behavior [28]. Therefore, a superposition of two self-affine fits [29] yields a better description of the magnetic $C(x)$:

$$C(x) = \sigma^2(c \cdot \exp[-(|x|/\xi_1)^{2\alpha_1}] + (1 - c) \cdot \exp[-(|x|/\xi_2)^{2\alpha_2}]) \quad (\text{D.7})$$

with c being a proportionality constant ($0 \leq c \leq 1$). In tab. S.1, the mean values of the fit parameters of $C(x)$ and $H(x)$ are listed. The proportionality constant c weights the second term (ξ_2 and α_2) in [eq. D.7] stronger. The analysis of the magnetic microstructure focuses therefore on the second term in [eq. D.7]. Fig. D.8(a) presents the magnetic correlation lengths (ξ_1 , ξ_2) and the topographic correlation length (ξ_{TOPO}) as a function of annealing temperature. Magnetic ξ_2 shows a correlation with annealing temperature, whereas for the

topographic lateral correlation length ξ_{TOPO} such a correlation cannot be observed. We can therefore conclude that ξ_2 is uniquely attributed to the magnetic microstructure. In particular ξ_2 is (75 ± 34) nm in the as-deformed state, corresponding to the grain size, as obtained for similar materials [12] and therefore showing single-domain behavior. ξ_2 decreases as a function of annealing temperature, i.e., upon annealing the domain size decreases causing a magnetic hardening.

In the following, the coercivity measured by SQUID-magnetometry is put into relation with ξ_2 . It is important to keep in mind that the magnetic ξ_2 decreases with increasing annealing temperature, meaning that in Fig. D.8(b) rising annealing temperature shifts from the right to the left. When referring to annealing treatments it seems unreasonable that higher annealing temperatures cause smaller magnetic feature sizes, but as it was shown in Fig. D.2 the microstructure does not show any change in grain size up to 400°C. As the as-deformed state is very far from thermodynamical equilibrium, it is more likely that the change in ξ_2 arises from a demixing process causing the magnetic Co-phase to agglomerate. Similar phase separation processes have already been observed in the Co-Cu system and have been attributed to spinodal decomposition [30]. The same separation process could be responsible for the improved magnetoresistive behavior of annealed Cu-Co HPT-materials [31]. In the 600°C annealed sample, a demixed state is present with the highest coercivity and the smallest magnetic ξ_2 .

It is important to mention that, although the magnetic hardening can be attributed to single-domain behavior, the critical diameter for single-domain particle size is in the range of 50 nm [23]. However, this value refers to bulk hcp-Co and one has to keep in mind that Co neither is present in its hcp-phase nor chemically pure, i.e., further investigations on the micromagnetic properties of such supersaturated fcc-Co phases need to be carried out.

D.4. Conclusion

In this study, Co-Cu samples with high Co-fractions are prepared using SPD by HPT. The thermal stability of Co72-Cu28 (wt.%) is investigated in detail, with the main focus being on microstructural and magnetic properties. By using a two-step HPT deformation at different temperatures a homogenization of strain distribution, and as a consequence an improved chemical homogeneity, is obtained. The resulting sample is nanocrystalline and exhibits a supersaturated, fcc single-phase microstructure. The microstructure exhibits a remarkable thermal stability, since no changes can be observed in SEM and XRD for annealing treatments

D. On the magnetic nanostructure of a Co-Cu alloy processed by high-pressure torsion

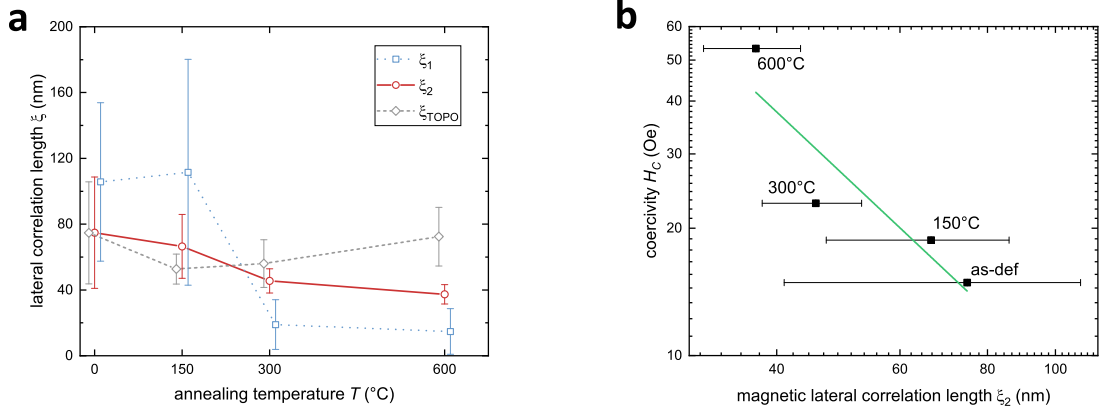


Figure D.8.: (a) Magnetic lateral correlation lengths ξ_1 , ξ_2 in comparison to topographic ξ_{TOPO} as a function of annealing temperature (c.f. tab. S.1). The data are slightly shifted in x for better visibility. (b) Coercivity H_C determined by SQUID-magnetometry versus magnetic ξ_2 obtained from correlating analysis of the MFM images. Note the log-axes.

up to 400°C. For annealing at 600°C, a demixed state, consisting of two fcc-phases, is present. Magnetometric measurements showed an increasing coercivity as a function of annealing temperature, meaning the observed changes in coercivity cannot be explained by formation of multidomain structures. Correlating MFM measurements with DC-SQUID magnetometry reveals domain sizes close to single-domain, whereas the demixed phases (with a magnetic correlation length smaller than the grain size) yield a magnetic hardening effect, which is able to explain the observed increase in coercivity – an indicator of demixing of the phases in context with spinodal decomposition.

Acknowledgments

This project has received funding from the European Research Council (ERC) under the European Union’s Horizon 2020 research and innovation programme (Grant No. 757333). A. M. acknowledges the support from the Lise Meitner fellowship by Austrian Science Fund (FWF): M 2323-N36.

Table D.1.: Roughness σ , lateral correlation length ξ , and Hurst parameter α as evaluated from auto-correlation function $C(x)$ and height-height correlation function $H(x)$ for the topographic (top) and magnetic signal (bottom). The data represent the mean values from at least 6 individual scans. As the magnetic signal exhibits two different Hurst parameters, the magnetic $C(x)$ is fitted by [eq. D.7] with c being a proportionality constant.

fit-parameters	as-deformed	150°C	300°C	600°C
topo σ_{TOPO} (nm)	3.2 \pm 0.7	3.0 \pm 0.2	2.6 \pm 0.5	2.8 \pm 0.2
ξ_{TOPO} (nm)	75 \pm 30	55 \pm 10	55 \pm 15	70 \pm 20
α_{TOPO}	0.55 \pm 0.05	0.35 \pm 0.05	0.60 \pm 0.05	0.65 \pm 0.10
magn σ (deg)	0.15 \pm 0.03	0.12 \pm 0.02	0.11 \pm 0.01	0.17 \pm 0.01
ξ_1 (nm)	110 \pm 50	110 \pm 70	20 \pm 15	20 \pm 10
ξ_2 (nm)	80 \pm 30	70 \pm 20	50 \pm 10	40 \pm 10
α_1	0.40 \pm 0.10	0.30 \pm 0.10	0.15 \pm 0.05	0.25 \pm 0.05
α_2	0.25 \pm 0.10	0.30 \pm 0.10	0.35 \pm 0.10	0.60 \pm 0.05
c	0.2 \pm 0.1	0.2 \pm 0.2	0.1 \pm 0.2	0.2 \pm 0.1

Supplementary

M-H curves

Figure. D.9 shows the hysteresis of the as-deformed and the annealed states in comparison to the pure Co-powder, measured at 8 K. The as-deformed and the annealed samples are measured in hard axis configuration and exhibit therefore a smaller susceptibility than the powder, which morphological shape appears more uniform. The evolution of coercivity and saturation magnetization have already been discussed in detail in fig. D.5.

D.5. References

- [1] H. Gleiter. “Nanocrystalline materials”. In: *Prog. Mater. Sci.* 33.4 (1989), pp. 223–315. DOI: 10.1016/0079-6425(89)90001-7.
- [2] G. Herzer et al. “Round table discussion: Present and future applications of nanocrystalline magnetic materials”. In: *J. Magn. Magn. Mater.* 294.2 (2005), pp. 252–266. DOI: 10.1016/j.jmmm.2005.03.042.
- [3] K. Suzuki et al. “Soft magnetic properties of nanocrystalline bcc Fe-Zr-B and Fe-M-B-Cu (M = transition metal) alloys with high saturation magnetization”. In: *J. Appl. Phys.* 70.10 (1991), pp. 6232–6237. DOI: 10.1063/1.350006.

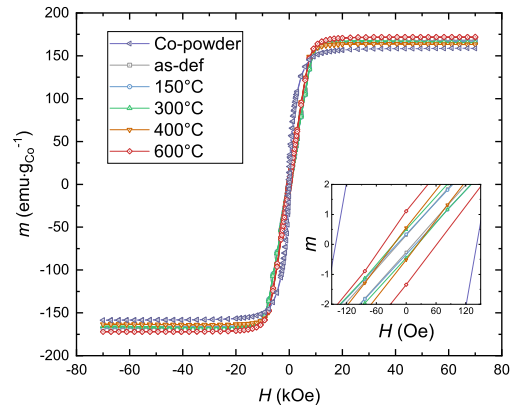


Figure D.9.: Hysteresis loops measured by SQUID-magnetometry at 8 K. The inset shows parts of the hysteresis loops at small fields.

- [4] G. Herzer. “Modern soft magnets: Amorphous and nanocrystalline materials”. In: *Acta Mater.* 61.3 (2013). The Diamond Jubilee Issue, pp. 718–734. DOI: 10.1016/j.actamat.2012.10.040.
- [5] T. Ambrose, A. Gavrin, and C.L. Chien. “Magnetic properties of metastable fcc Fe-Cu alloys prepared by high energy ball milling”. In: *J. Magn. Magn. Mater.* 124 (1993), pp. 15–19. DOI: 10.1016/0304-8853(93)90063-8.
- [6] T.D. Shen, R.B. Schwarz, and J.D. Thompson. “Soft magnetism in mechanically alloyed nanocrystalline materials”. In: *Phys. Rev. B* 72.1 (2005), p. 014431. DOI: 10.1103/PhysRevB.72.014431.
- [7] R.Z. Valiev, R.K. Islamgaliev, and I.V. Alexandrov. “Bulk nanostructured materials from severe plastic deformation”. In: *Prog. Mater. Sci.* 45.2 (2000), pp. 103–189. DOI: 10.1016/S0079-6425(99)00007-9.
- [8] R. Pippan et al. “The limits of refinement by severe plastic deformation”. In: *Adv. Eng. Mater.* 8.11 (2006), pp. 1046–1056. DOI: 10.1002/adem.200600133.
- [9] A.R. Kilmametov et al. “The $\alpha \rightarrow \omega$ and $\beta \rightarrow \omega$ phase transformations in Ti-Fe alloys under high-pressure torsion”. In: *Acta Mater.* 144 (2018), pp. 337–351. DOI: 10.1016/j.actamat.2017.10.051.
- [10] R.C. O’Handley. “Opportunities in magnetic anisotropy and magnetostriction”. In: *Mater. Sci. Eng. B* 3.4 (1989), pp. 365–369. DOI: 10.1016/0921-5107(89)90142-6.
- [11] K.S. Kormout, R. Pippan, and A. Bachmaier. “Deformation-induced supersaturation in immiscible material systems during high-pressure torsion”. In: *Adv. Eng. Mater.* 19.4 (2017), p. 1600675. DOI: 10.1002/adem.201600675.

- [12] M. Stücker et al. “Magnetic Binary Supersaturated Solid Solutions Processed by Severe Plastic Deformation”. In: *Nanomaterials* 9.1 (2018), p. 6. DOI: 10.3390/nano9010006.
- [13] A. Bachmaier et al. “Tailoring the magnetic properties of nanocrystalline Cu-Co alloys prepared by high-pressure torsion and isothermal annealing”. In: *J. Alloys Compds.* 725 (2017), pp. 744–749. DOI: 10.1016/j.jallcom.2017.07.200.
- [14] A. Bachmaier et al. “On the process of co-deformation and phase dissolution in a hard-soft immiscible CuCo alloy system during high-pressure torsion deformation”. In: *Acta Mater.* 115 (2016), pp. 333–346. DOI: 10.1016/j.actamat.2016.06.010.
- [15] R. Pippin et al. “Saturation of fragmentation during severe plastic deformation”. In: *Annu. Rev. Mater. Sci.* 40 (2010), pp. 319–343. DOI: 10.1146/annurev-matsci-070909-104445.
- [16] O. Renk and R. Pippin. “Saturation of Grain Refinement during Severe Plastic Deformation of Single Phase Materials: Reconsiderations, Current Status and Open Questions”. In: *Mater. Trans.* 60.7 (2019), pp. 1270–1282. DOI: 10.2320/matertrans.MF201918.
- [17] O. Renk et al. “Increasing the strength of nanocrystalline steels by annealing: Is segregation necessary?” In: *Scr. Mater.* 95 (2015), pp. 27–30. DOI: 10.1016/j.scriptamat.2014.09.023.
- [18] J.B. Nelson and D.P. Riley. “An experimental investigation of extrapolation methods in the derivation of accurate unit-cell dimensions of crystals”. In: *Proc. Phys. Soc.* 57.3 (1945), p. 160. DOI: 10.1088/0959-5309/57/3/302.
- [19] L. Vegard. “Die Konstitution der Mischkristalle und die Raumfüllung der Atome”. In: *Z. Phys.* 5.1 (1921), pp. 17–26. DOI: 10.1007/BF01349680.
- [20] M.J. Kriegel et al. “Thermal Stability of athermal ω -Ti (Fe) Produced upon Quenching of β -Ti (Fe)”. In: *Adv. Eng. Mater.* 21.1 (2019), p. 1800158. DOI: 10.1002/adem.201800158.
- [21] J.R. Childress and C.L. Chien. “Reentrant magnetic behavior in fcc Co-Cu alloys”. In: *Phys. Rev. B* 43.10 (1991), p. 8089. DOI: 10.1103/PhysRevB.43.8089.
- [22] *Application Note 1500-011*. Rev. A0. Quantum Design, San Diego, California. 2010.
- [23] H. Kronmüller and M. Fähnle. *Micromagnetism and the microstructure of ferromagnetic solids*. Cambridge University Press, 2003.
- [24] M. Jamet et al. “Magnetic anisotropy of a single cobalt nanocluster”. In: *Phys. Rev. Lett.* 86.20 (2001), p. 4676. DOI: 10.1103/PhysRevLett.86.4676.
- [25] N.V. Andreeva et al. “A study of nanostructure magnetosolid Nd-Ho-Fe-Co-B materials via atomic force microscopy and magnetic force microscopy”. In: *Phys. Solid State* 58.9 (2016), pp. 1862–1869. DOI: 10.1134/S1063783416090079.
- [26] Y. Zhao, G.-C. Wang, and T.-M. Lu. *Characterization of Amorphous and Crystalline Rough Surface—Principles and Applications*. Elsevier, 2000.

- [27] C. Teichert. “Self-organization of nanostructures in semiconductor heteroepitaxy”. In: *Phys. Rep.* 365.5 (2002), pp. 335–432. DOI: 10.1016/S0370-1573(02)00009-1.
- [28] C. Teichert, J.J. De Miguel, and T. Bobek. “Ion beam sputtered nanostructured semiconductor surfaces as templates for nanomagnet arrays”. In: *J. Phys. Condens. Matter* 21.22 (2009), p. 224025. DOI: 10.1088/0953-8984/21/22/224025.
- [29] M. Tolan et al. “Evidence for capillary waves on dewetted polymer film surfaces: A combined X-ray and atomic force microscopy study”. In: *Phys. Rev. Lett.* 81.13 (1998), p. 2731. DOI: 10.1103/PhysRevLett.81.2731.
- [30] A. Bachmaier et al. “Phase separation of a supersaturated nanocrystalline Cu-Co alloy and its influence on thermal stability”. In: *Acta Mater.* 96 (2015), pp. 269–283. DOI: 10.1016/j.actamat.2015.05.0530.
- [31] S. Wurster et al. “Microstructural Changes Influencing the Magnetoresistive Behavior of Bulk Nanocrystalline Materials”. In: *Appl. Sci.* 10.15 (2020), p. 5094. DOI: 10.3390/app10155094.

E. Formation of supersaturated solid solutions of Cu-Fe-Co by severe plastic deformation

Martin Stückler¹, Lukas Weissitsch¹, Stefan Wurster¹, Heinz Krenn², Reinhard Pippan¹ and Andrea Bachmaier¹

¹ *Erich Schmid Institute of Materials Science, Austrian Academy of Sciences, Jahnstraße 12, 8700 Leoben, Austria*

² *Institute of Physics, University of Graz, Universitätsplatz 5, 8010 Graz, Austria*

Abstract

Initial powder mixtures of Cu, Fe and Co are exposed to severe plastic deformation by high-pressure torsion to prepare solid solutions. A broad range of compositions is investigated, whereas this study aims at the synthesis of soft magnetic materials and therefore at the formation of a homogeneous and nanocrystalline microstructure. For intermediate Cu-contents, high-pressure torsion at room temperature yields single-phase supersaturated solid solutions. For smaller Cu-contents two consecutive steps of high-pressure torsion deformation at different temperatures yield the desired nanocrystalline microstructure. Depending on the Co-to-Fe-ratio, either a single-phase supersaturated solid solution or a nanocomposite forms. The nanocomposite exhibits an enhanced magnetic moment, indicating the formation of an (Fe,Co)-alloy upon severe plastic deformation. Soft magnetic properties are verified for large Co-to-Fe-ratios and this microstructure is found to remain stable up to 400°C.

Keywords: severe plastic deformation, high-pressure torsion, supersaturation, nanocrystalline

E.1. Introduction

Nanocrystallinity is a prerequisite to form high performance soft magnetic materials [1]. With high-pressure torsion (HPT), a technique of severe plastic deformation (SPD), nanocrystalline materials can be processed in bulk form [2]. Furthermore, it has been shown, that HPT is capable to tune the coercivity even by orders of magnitude with respect to the initial state, whereas larger effects have been observed for multi-phase materials [3–6]. To achieve low coercivities, the formation of a homogeneous microstructure, exhibiting nanocrystalline grains with low magnetocrystalline anisotropy, is desirable.

In Ref. [7], it was shown that such microstructures can be processed from binary powder mixtures of Cu-Fe and Cu-Co, whereas Cu-Co samples exhibit soft magnetic properties. The processing limits of HPT at room temperature have been examined as well: in case of Cu-Fe, it was shown that homogeneous deformation was achieved for Fe contents below 25 wt.%. Higher Fe-contents yield localization of strain resulting in a multi phase microstructure. In case of Co-Cu, supersaturated solid solutions have been processed for Co contents between 28 wt.% and 67 wt.%. Lower Co-contents yield residual particles, i.e., no complete supersaturation could be obtained. Higher Co-contents result in brittle specimens with cracks forming during deformation. By performing two consecutive steps of HPT-deformation at different temperatures it was possible to push the limits of processability towards very high Co-contents [8].

In the present work, different Fe-Co ratios are mixed with Cu. This study aims at superior soft magnetic properties, since the addition of Fe can lead to decreasing magnetocrystalline anisotropy and increasing saturation magnetization. The focus is on the processability of Cu-Fe-Co alloys by HPT and the formation of homogeneous microstructures. Furthermore, the thermal stability of the metastable supersaturated solid solutions is investigated.

E.2. Experimental

Samples were processed from conventional powders (Fe: MaTeck 99.9% -100+200 mesh; Co: GoodFellow 99.9% 50-150 μm ; Cu: Alfa Aesar -170+400 mesh 99.9%). Powder mixtures were prepared and consolidated under hydrostatic pressure in Ar-atmosphere. The consolidated powders were exposed to SPD by HPT, resulting in cylindrical specimens (diameter: 8 mm; thickness: 1 mm). For deformation at higher temperatures (up to 500°C), the anvils were inductively heated. HPT was performed under a pressure of 5 GPa at 1.28 min^{-1} rotational

speed of the anvils. To ensure a microstructural steady state, 50-150 numbers of turns were applied in total, resulting in a maximum achieved shear strain γ of 1000-3000 at a radius of 3 mm. Microstructural investigations were performed by scanning electron microscopy (SEM; Zeiss LEO1525) in backscattered electron (BSE) mode. The local composition of the samples was determined by an energy dispersive X-ray spectroscopy (EDS; Bruker XFlash 6|60) system and is given in weight percent (wt.%) herein. Quantitative grain size evaluation is carried out by Transmission Kikuchi Diffraction (TKD) using a Bruker e⁻-Flash^{FS}. Vickers hardness measurements were performed with a Buehler Micromet 5100 under a load of 0.5 kg (HV0.5). The crystallographic structure was measured by X-ray diffraction using a Bruker D2 Phaser (Co-K_α radiation) and by synchrotron XRD (DESY; Petra III: P07) in transmission mode at an energy of 100 keV. DC-magnetometric measurements were performed with a Quantum Design MPMS-XL7 SQUID-magnetometer at 8 K.

E.3. Results and Discussion

E.3.1. Supersaturated solid solutions by HPT

In fig. E.1 the ternary phase diagram for compositions, which are investigated in this study are shown. The compositions are determined by EDS. Compositions which have been processed by HPT-deformation at room temperature (RT; 50 turns) are marked by red dots and are referred to as RT-HPT in the following. The corresponding SEM micrographs are shown in fig. E.1(a)-(c) and reveal grain sizes in the nanocrystalline regime. Furthermore low phase contrast is apparent, indicating also a chemical homogeneity. The RT-HPT deformed samples exhibit compositions close to the binary Co-Cu samples in Ref. [7]. Since the homogeneity of deformation has been reported to be sensitive to hardness and crystal lattices of the initial phases [9], successful processing of the ternary materials can be expected for compositions close to the binary samples, which deform homogeneously. Indeed, ternary samples exhibiting Fe-contents higher than 20 wt.% and/or Co contents above 70wt.%, show residual particles and the formation of shear bands or cracks.

To access also different compositions, the 2-step HPT-deformation technique is employed to compositions with low Cu-contents, as described in Ref. [8]. These samples are referred to as 2-step HPT samples in the following. At first, the deformation is performed at elevated temperatures (300°C or 500°C; 100 turns or 50 turns). After, the sample is exposed to a second deformation step at RT (additional 50 turns). The 2-step HPT samples are indicated

E. Formation of supersaturated solid solutions of Cu-Fe-Co by severe plastic deformation

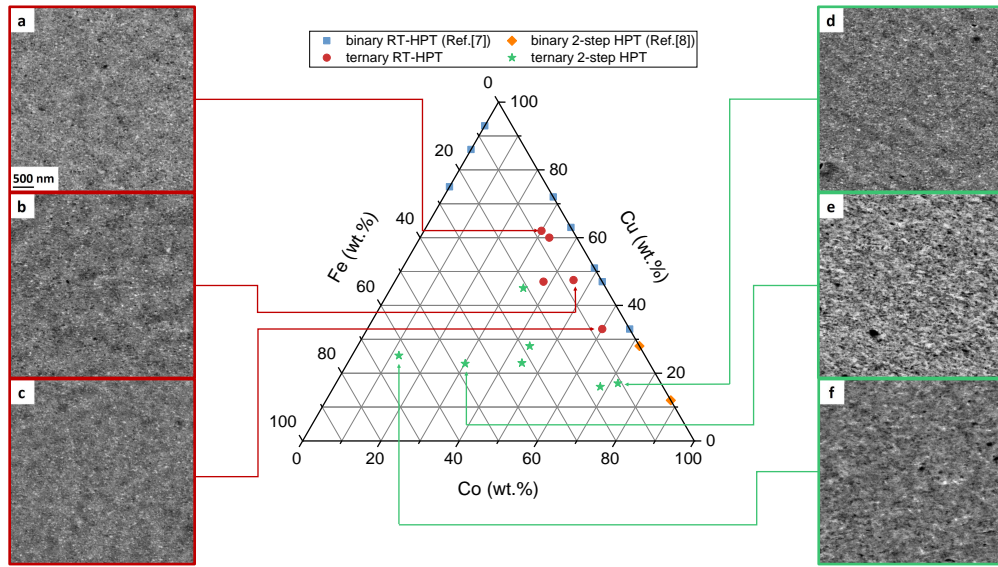


Figure E.1.: SEM micrographs of as-deformed samples. The ternary phase diagram shows the samples investigated in this study with the compositions determined from EDS-measurements. Images on the left (a)-(c) shows samples, which are processed by RT-HPT. Images on the right (d)-(f) shows samples processed by 2-steps of HPT as described in the text. Micrographs were taken on HPT-discs cut in half at $r=3$ mm with the radial direction parallel to the horizontal axis. The scale bar in (a) applies to all micrographs.

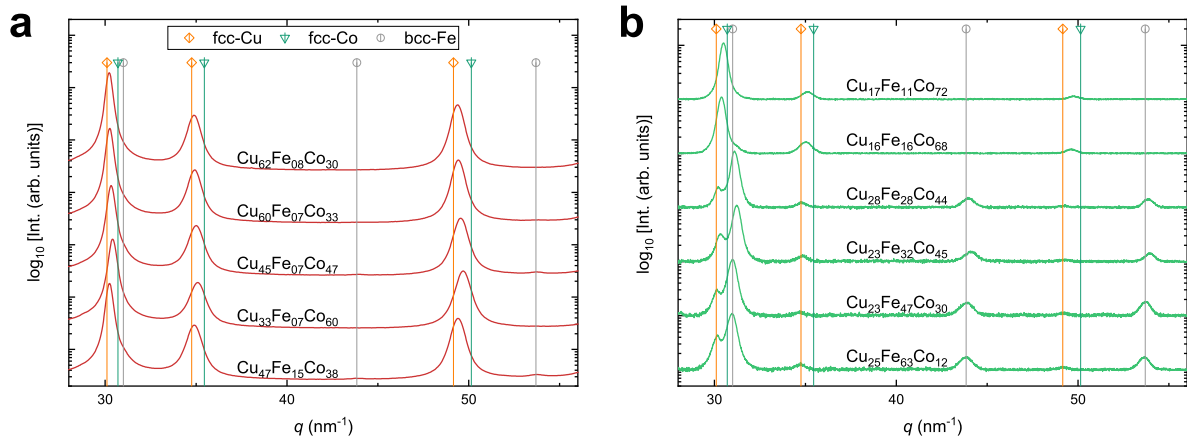


Figure E.2.: In (a), synchrotron XRD patterns are shown for RT-HPT processed samples. In (b), XRD patterns for 2-step HPT-processed samples are shown (c.f. fig. E.1), measured with $\text{Co-K}\alpha$ radiation. An increasing Fe/Co-ratio is shown from top to bottom (b). The legend in (a) applies also to (b).

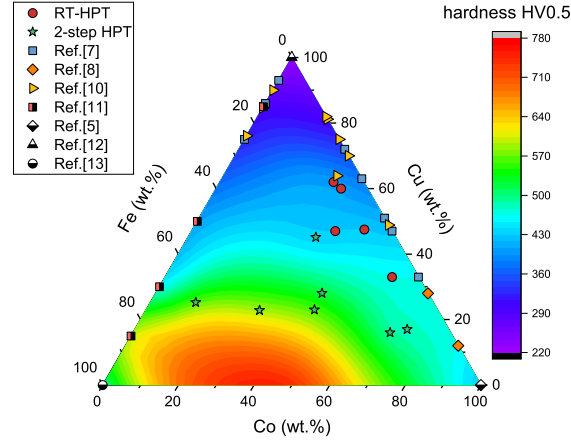


Figure E.3.: Hardness as a function of composition for HPT-processed solid solutions of Cu-Fe-Co.

by green stars in fig. E.1. Apparent phase contrast is visible in the SEM micrographs in fig. E.1(e) and (f), indicating chemically different phases. Furthermore a larger grain size can be noticed in comparison to the specimen exhibiting the lowest Fe-content (fig. E.1(d)).

Fig. E.2(a) shows results from synchrotron-XRD experiments for RT-HPT processed samples. All samples exhibit a major fcc pattern. Beside a very shallow bcc-Fe peak for $\text{Cu}_{47}\text{Fe}_{15}\text{Co}_{38}$ at $q=53.6 \text{ nm}^{-1}$, only single-phase crystallographic structures are present as has been reported for binary Cu-Co [7]. In fig. E.2(b), XRD patterns (Co- K_{α} radiation) of the 2-step HPT deformed samples are shown. For an increasing Fe/Co-ratio (from top to bottom), a crossover from single phase to dual phase crystallographic structures can be observed in accordance to SEM micrographs fig. E.1(e),(f). For Co-contents $\geq 30 \text{ wt.}\%$, the fcc-peaks shift from the Cu-peak position, indicating the formation of supersaturated solid solutions. In contrast, for lower Co-contents this peak shift cannot be observed, indicating the presence of a rather pure fcc-Cu phase. We assume that $\alpha\text{-(Fe,Co)}$ forms as a second phase. In all XRD-patterns, a huge peak width can be observed, arising from the large amount of crystal defects, but also from the grain refinement. To quantify the grain size, a RT-HPT processed sample ($\text{Cu}_{60}\text{Fe}_{07}\text{Co}_{33}$) is measured with TKD. Five scans are jointly analyzed, revealing a median grain size of 66 nm, which is a somewhat smaller grain size as has been obtained for binary Cu-Co (76 nm-100 nm [7]).

In fig. E.3, the Vickers hardness is plotted as a function of composition. The data from this study are compared with hardness values for binary HPT-deformed samples from other studies. In all studies, initial powder mixtures are used [7, 8, 10, 11]. Pure elements have

E. Formation of supersaturated solid solutions of Cu-Fe-Co by severe plastic deformation

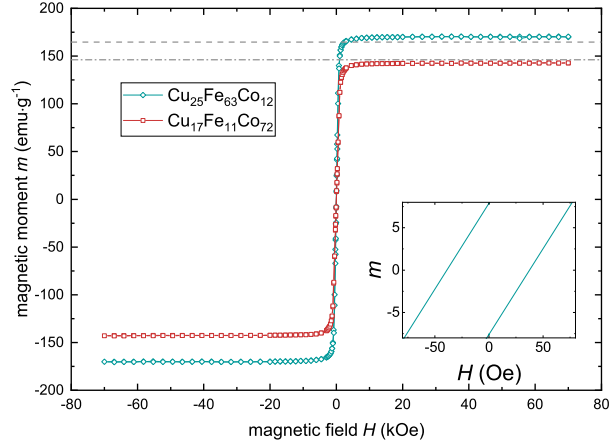


Figure E.4.: Hysteresis curves measured by SQUID-magnetometry at 8 K of two samples, processed by 2-step HPT deformation process. The dashed lines give literature values for isolated Fe and Co phases for the compositions investigated. The inset shows $\text{Cu}_{25}\text{Fe}_{63}\text{Co}_{12}$ at small fields, whereas for $\text{Cu}_{17}\text{Fe}_{11}\text{Co}_{72}$ the coercivity collapses to such a small value which cannot be resolved due to residual fields in the superconducting magnet.

been HPT-deformed from powders as well [5, 12] or from bulky ARMCO Fe [13]. In all mentioned studies, at least the last processing step has been carried out at RT, yielding the RT saturation grain size for every composition [14]. A higher hardness, with respect to the coarse grained materials, is expected mainly due to Hall-Petch hardening [15, 16]. A linearly increasing hardness can be observed for Cu-Co up to about 80 wt.% of Co. Larger Co-contents exhibit smaller hardness values which is expected to arise from a diminishing contribution of solid solution hardening. A similar trend is visible for binary Cu-Fe. In comparison to binary Cu-Co, the hardness is increased in the ternary alloys. As has been shown in the XRD-patterns (c.f. fig. E.2), two crystallographic phases start to form, when exceeding a certain Fe-content. For dual phase materials a rapid increase in hardness can be observed, arising from a complex hardening behavior of the involving phase and grain boundaries [17].

The magnetic moments m of one Fe-rich and one Co-rich specimen, containing about 20 wt% of Cu, namely $\text{Cu}_{17}\text{Fe}_{11}\text{Co}_{72}$ and $\text{Cu}_{25}\text{Fe}_{63}\text{Co}_{12}$, are measured by SQUID-magnetometry at 8 K. Since intermetallic alloys of (Fe,Co) exhibit an overproportional high magnetic moment, the alloying behavior on an atomic scale can be observed in this manner. In fig. E.4, the magnetic moments m are plotted for both compositions. For the Fe-rich composition $\text{Cu}_{25}\text{Fe}_{63}\text{Co}_{12}$, m is larger than the reference value for isolated Fe and Co, showing the formation of an (Fe,Co)-phase in accordance with XRD-data (c.f. fig. E.2). For the Co-

rich composition $\text{Cu}_{17}\text{Fe}_{11}\text{Co}_{72}$, the saturation magnetization coincides within the errors after a linear superposition of reference values for Fe and Co (plotted as horizontal lines in fig. E.4). Therefore, no formation of an (Fe,Co)-phase is apparent in this case, coinciding with the microstructural investigations, which show a single-phase microstructure being present (c.f. fig. E.1,E.2). The Fe-rich composition $\text{Cu}_{25}\text{Fe}_{63}\text{Co}_{12}$ exhibits a large coercivity of $H_C=39\pm 1$ Oe, whereas the coercivity of Co-rich $\text{Cu}_{17}\text{Fe}_{11}\text{Co}_{72}$ cannot be properly resolved due to the remanent field of the superconducting magnet [18] but it is expected to be smaller than 10 Oe. An exhaustive determination of the coercivity for $\text{Cu}_{17}\text{Fe}_{11}\text{Co}_{72}$ is instead performed by means of AC-hysteresis measurements and can be found in Ref. [19] revealing a H_C of about 2 Oe. The high H_C for $\text{Cu}_{25}\text{Fe}_{63}\text{Co}_{12}$ is due to the larger grain size as well as the larger magnetocrystalline anisotropy for this intermetallic alloy of (Fe,Co), whereas in the Co-rich $\text{Cu}_{25}\text{Fe}_{63}\text{Co}_{12}$, the supersaturation and concomitant grain refinement causes a break down in magnetocrystalline anisotropy. The results show that, although being similarly processed, the magnetic behavior of both compositions differs extremely, arising from different microstructural states after HPT-deformation.

E.3.2. Evolution of the supersaturated state upon annealing

The 2-step HPT-processed sample with composition $\text{Cu}_{17}\text{Fe}_{11}\text{Co}_{72}$ forms a single-phase supersaturated solid solution. The temperature stability of this sample is investigated in the following.

The sample is exposed to conventional annealing treatments for 150°C, 300°C, 400°C, 600°C and 800°C for 1 hour each. In fig. E.5, SEM micrographs of 300°C (a), 600°C (b) and 800°C (c) annealed states are shown. The 300°C annealed state shows a slightly enhanced grain size with respect to the as-deformed state and some dark particles are visible, indicating the presence of a second phase. For the 600°C annealed state, the size of both, the grain size and the second phase particles increases. The 800°C shows a completely different microstructure with high phase contrast, indicating a complete demixing of phases, but the grain size is still in the ultrafine-grained regime. In fig. E.5(d), Vickers hardness is plotted as a function of annealing temperature. An enhanced hardness can be observed for 150°C-, 300°C- and 400°C-annealed states, which is a typical behavior of nanocrystalline materials [20–22]. The hardness decreases in the 600°C-annealed state due to grain coarsening. Further grain coarsening as well as demixing, i.e., the reduction in solution hardening, lead to an even smaller hardness in the 800°C annealed state.

To investigate the evolution of crystallographic phases upon annealing in more detail,

E. Formation of supersaturated solid solutions of Cu-Fe-Co by severe plastic deformation

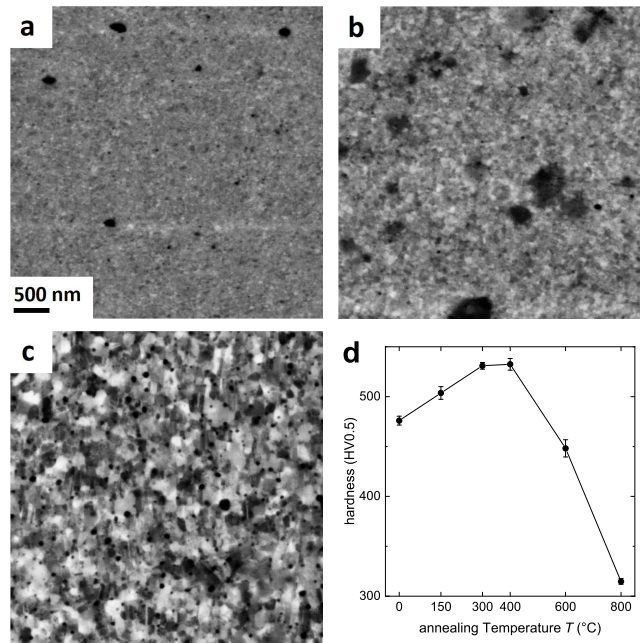


Figure E.5.: SEM micrographs of $\text{Cu}_{17}\text{Fe}_{11}\text{Co}_{72}$ (c.f. fig. E.1(d)) exposed to annealing temperatures at 300°C (a), 600°C (b) and 800°C (c). The scale bar in (a) applies also to (b) and (c). In (d), Vickers hardness is plotted as a function of annealing temperature.

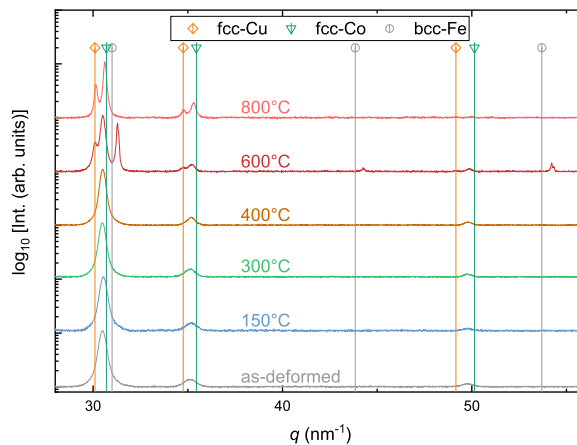


Figure E.6.: XRD-patterns of annealed $\text{Cu}_{17}\text{Fe}_{11}\text{Co}_{72}$ measured with $\text{Co-K}\alpha$ radiation.

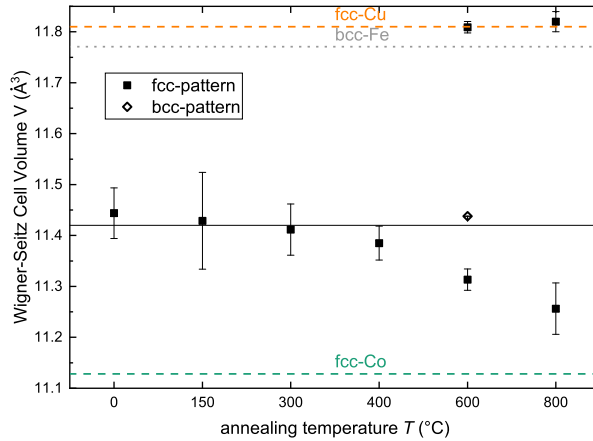


Figure E.7.: Wigner-Seitz cell volume of $\text{Cu}_{17}\text{Fe}_{11}\text{Co}_{72}$, as determined from XRD-patterns (c.f. fig. E.6). The solid line represents the Wigner-Seitz cell volume for the composition measured with EDS.

XRD-measurements are carried out (fig. E.6). Starting with the as-deformed state, where only one phase is present, the single-phase fcc-microstructure retains even upon annealing at 400°C. At 600°C, the microstructure decomposes into two fcc-patterns as well as a bcc-pattern forms out. At 800°C the bcc-pattern vanishes and two fcc-patterns are visible. For a detailed analysis of the formation and decomposition of solid solutions during heat treatment, the lattice constants are evaluated for every pattern by examining the Nelson-Riley function [23]. Vegard's law [24] for solid solutions is extended to oppose different crystal structures by comparing the Wigner-Seitz cell volume, instead of the lattice constant. The Wigner-Seitz cell volume is plotted as a function of annealing temperature T in fig. E.7. The solid line represents the Wigner-Seitz cell volume for the composition as measured with EDS, coinciding with the value measured by XRD up to 300°C. The Wigner-Seitz cell volume decreases slightly with increasing temperature which is due to stress relief. At 600°C three patterns have been observed, whereas one value coincides very well with fcc-Cu. We therefore conclude that two solid solutions of (Fe,Co) are present. Assuming the Wigner-Seitz cell volumes of fcc-Co and bcc-Fe, the compositions can be calculated to $\text{Fe}_{47}\text{Co}_{53}$ in the bcc-phase and $\text{Fe}_{28}\text{Co}_{72}$ in the fcc-phase. For annealing at 800°C, the Wigner-Seitz cell volume for Cu remains constant, whereas the bcc-phase vanishes and the value of the second fcc-phase shifts, showing the formation of the thermodynamically stable γ -(Fe,Co) phase [25].

E.4. Conclusion

In this study, the processability of ternary CuFeCo alloys by HPT is investigated starting from initial powder mixtures. Taking results from binary compositions as a basis, which have been successfully processed in recent studies, a region in the ternary phase diagram has been detected, where homogeneous nanocrystalline supersaturated solid solutions can be processed by HPT at RT. For processing of compositions with higher ferromagnetic content, two consecutive steps of HPT-deformation at different temperatures have to be used. The Co-rich specimens form a supersaturated solid solution upon HPT-deformation. For the Fe-rich samples a nanocompound, exhibiting bcc- and fcc-phases, is observed. The nanocompound exhibits semi-hard behavior and the formation of α -(Fe,Co) with enhanced magnetic moment, which can be observed even in the as-deformed state. For the single-phase supersaturated solid solution, an enhanced magnetic moment cannot be observed but soft magnetic behavior is observed. The temperature stability of a high Co-containing composition shows a persisting nanocrystallinity up to 400°C, but decomposition at 600°C into the stable phases according to thermodynamical equilibrium.

Acknowledgments

This project has received funding from the European Research Council (ERC) under the European Union's Horizon 2020 research and innovation programme (Grant No. 757333). The measurements leading to these results have been performed at PETRA III: P07 at DESY Hamburg (Germany), a member of the Helmholtz Association (HGF). We gratefully acknowledge the assistance by Norbert Schell and further thank F. Spieckermann and C. Gammer for their help with data processing. The authors thank M. Kasalo for sample preparation preparation and A. Paulischin for hardness measurements.

E.5. References

- [1] G. Herzer. "Modern soft magnets: Amorphous and nanocrystalline materials". In: *Acta Mater.* 61.3 (2013). The Diamond Jubilee Issue, pp. 718–734. DOI: 10.1016/j.actamat.2012.10.040.
- [2] R.Z. Valiev, R.K. Islamgaliev, and I.V. Alexandrov. "Bulk nanostructured materials from severe plastic deformation". In: *Prog. Mater. Sci.* 45.2 (2000), pp. 103–189. DOI: 10.1016/S0079-6425(99)00007-9.

- [3] B.B. Straumal et al. “Effect of severe plastic deformation on the coercivity of Co–Cu alloys”. In: *Philos. Mag. Lett.* 89.10 (2009), pp. 649–654. DOI: 10.1080/09500830903246268.
- [4] S. Scheriau et al. “Magnetic characteristics of HPT deformed soft-magnetic materials”. In: *J. Magn. Magn. Mater.* 322.20 (2010), pp. 2984–2988. DOI: 10.1016/j.jmmm.2010.04.032.
- [5] K. Edalati et al. “High-pressure torsion of pure cobalt: hcp-fcc phase transformations and twinning during severe plastic deformation”. In: *Appl. Phys. Lett.* 102.18 (2013), p. 181902. DOI: 10.1063/1.4804273.
- [6] A. Bachmaier et al. “Tailoring the magnetic properties of nanocrystalline Cu-Co alloys prepared by high-pressure torsion and isothermal annealing”. In: *J. Alloys Compds.* 725 (2017), pp. 744–749. DOI: 10.1016/j.jallcom.2017.07.200.
- [7] M. Stücker et al. “Magnetic Binary Supersaturated Solid Solutions Processed by Severe Plastic Deformation”. In: *Nanomaterials* 9.1 (2018), p. 6. DOI: 10.3390/nano9010006.
- [8] M. Stücker et al. “On the magnetic nanostructure of a Co-Cu alloy processed by high-pressure torsion”. In: *J. Sci. Adv. Mater. Dev.* (2020). in press. DOI: 10.1016/j.jsamd.2020.09.013.
- [9] K.S. Kormout, R. Pippan, and A. Bachmaier. “Deformation-induced supersaturation in immiscible material systems during high-pressure torsion”. In: *Adv. Eng. Mater.* 19.4 (2017), p. 1600675. DOI: 10.1002/adem.201600675.
- [10] S. Wurster et al. “Tunable Magneto-Resistance by Severe Plastic Deformation”. In: *Metals* 9.11 (2019). DOI: 10.3390/met9111188.
- [11] A. Bachmaier et al. “The formation of supersaturated solid solutions in Fe-Cu alloys deformed by high-pressure torsion”. In: *Acta Mater.* 60.3 (2012), pp. 860–871. DOI: 10.1016/j.actamat.2011.10.044.
- [12] K.S. Kormout et al. “Deformation mechanisms during severe plastic deformation of a CuAg composite”. In: *J. Alloys Compd.* 695 (2017), pp. 2285–2294. DOI: 10.1016/j.jallcom.2016.11.085.
- [13] R.Z. Valiev et al. “Structure and deformation behaviour of Armco iron subjected to severe plastic deformation”. In: *Acta Mater.* 44.12 (1996), pp. 4705–4712. DOI: 10.1016/S1359-6454(96)00156-5.
- [14] O. Renk and R. Pippan. “Saturation of Grain Refinement during Severe Plastic Deformation of Single Phase Materials: Reconsiderations, Current Status and Open Questions”. In: *Mater. Trans.* 60.7 (2019), pp. 1270–1282. DOI: 10.2320/matertrans.MF201918.
- [15] E.O. Hall. “The deformation and ageing of mild steel: III discussion of results”. In: *Proc. Ph. Soc. London Sect. B* 64.9 (1951), p. 747. DOI: 10.1088/0370-1301/64/9/303.

- [16] N.J. Petch. “The cleavage strength of polycrystals”. In: *J. Iron Steel Inst.* 174 (1953), pp. 25–28.
- [17] E. Werner and H.P. Stüwe. “Phase boundaries as obstacle to dislocations motion”. In: *Materials Science and Engineering* 68.2 (1985), pp. 175–182. DOI: 10.1016/0025-5416(85)90406-9.
- [18] M. Buchner et al. “Tutorial: Basic principles, limits of detection, and pitfalls of highly sensitive SQUID magnetometry for nanomagnetism and spintronics”. In: *J. Appl. Phys.* 124.16 (2018), p. 161101. DOI: 10.1063/1.5045299.
- [19] M. Stückler et al. “In-situ AC-hysteresis measurements of SPD-processed $\text{Cu}_{20}(\text{Fe}_{15}\text{Co}_{85})_{80}$ ”. In: *AIP Adv.* (2021). submitted.
- [20] T. Volpp et al. “Grain size determination and limits to Hall-Petch behavior in nanocrystalline NiAl powders”. In: *Nanostruct. Mater.* 8.7 (1997), pp. 855–865. DOI: 10.1016/S0965-9773(98)00019-1.
- [21] Y.M. Wang et al. “Effects of annealing and impurities on tensile properties of electrodeposited nanocrystalline Ni”. In: *Scr. Mater.* 51.11 (2004), pp. 1023–1028. DOI: 10.1016/j.scriptamat.2004.08.015.
- [22] O. Renk et al. “Increasing the strength of nanocrystalline steels by annealing: Is segregation necessary?” In: *Scr. Mater.* 95 (2015), pp. 27–30. DOI: 10.1016/j.scriptamat.2014.09.023.
- [23] J.B. Nelson and D.P. Riley. “An experimental investigation of extrapolation methods in the derivation of accurate unit-cell dimensions of crystals”. In: *Proc. Phys. Soc.* 57.3 (1945), p. 160. DOI: 10.1088/0959-5309/57/3/302.
- [24] L. Vegard. “Die Konstitution der Mischkristalle und die Raumbfüllung der Atome”. In: *Z. Phys.* 5.1 (1921), pp. 17–26. DOI: 10.1007/BF01349680.
- [25] I. Ohnuma et al. “Phase equilibria in the Fe–Co binary system”. In: *Acta Mater.* 50.2 (2002), pp. 379–393. DOI: 10.1016/S1359-6454(01)00337-8.

F. In-situ AC-hysteresis measurements of SPD-processed $\text{Cu}_{20}(\text{Fe}_{15}\text{Co}_{85})_{80}$

Martin Stückler, Stefan Wurster, Reinhard Pippan and Andrea Bachmaier

Erich Schmid Institute of Materials Science, Austrian Academy of Sciences, Jahnstraße 12, 8700 Leoben, Austria

Abstract

The changes of magnetic properties upon heat treatment of a metastable supersaturated solid solution processed by severe plastic deformation are investigated by in-situ AC-hysteresis measurements. Data are analyzed in the framework of dynamic loss theory, with correlative investigations of the microstructural properties. The evolution of hysteresis upon annealing points out that the single-phase supersaturated solid solution remains stable up to 400°C, then hindering of domain wall motion sets in at this temperature. At 600°C, a multi phase microstructure is present, causing a significant increase in coercivity.

F.1. Introduction

With high-pressure torsion (HPT), a technique of severe plastic deformation (SPD), it is possible to form bulk supersaturated solid solutions with grain sizes in the nanocrystalline regime [1, 2]. It has been shown, that with different ratios of Co to Cu, huge reductions in the coercivity can be achieved by means of SPD, resulting in soft magnetic materials [3, 4]. In the present study, Fe is added to lower the magnetocrystalline anisotropy to further reduce the coercivity [5]. To study the evolution of magnetic properties as a function of temperature, the hysteresis is recorded during in-situ annealing treatments with a concomitant investigation of

the dynamic magnetic behavior for certain temperatures. The resulting data are discussed in the framework of dynamic loss theory and correlated to the evolving microstructure.

F.2. Experimental

Powders (Fe: MaTeck 99.9% -100+200 mesh; Co: GoodFellow 99.9% 50-150 μm ; Cu: Alfa Aesar -170+400 mesh 99.9%) were mixed and hydrostatically consolidated in Ar-atmosphere. A coin-shaped specimen (diameter: 8 mm; thickness: 1 mm) was processed by two subsequent steps of HPT deformation (100 turns at 300°C; 50 turns at room temperature (RT)), as described elsewhere[4]. The sample was further processed into a ring shaped specimen and equipped with 68 primary windings and 61 secondary windings (Cu-wire; diameter: 0.315 mm and 0.200 mm, respectively). Electrical isolation between the sample and the windings was maintained with a high temperature adhesive (Minco FortaFix Autostic FC8). To apply the magnetic field, a sinusoidal current (4 A; 5-1000 Hz) was applied to the primary winding with a KEPCO BOP 100-4M power supply, according to [eq. F.1a]. The voltage induced in the secondary windings [eq. F.2] was measured with a National Instruments BNC-2110 terminal block. Data processing was carried out with LabView (version 14.0.1f3). The hysteresis measurement is described in more detail in Ref. [6]. For in-situ measurements, the sample was clamped between two Cu-blocks and heated by cartridge heaters (hotset hotrod HHP HT4030504). The temperature was measured by a K-type thermocouple, close to the samples' position to ensure the hysteresis measurements take place at $\pm 5^\circ\text{C}$ of the target temperature. To maintain a homogeneously heated sample, measurements were started 15 min after stabilization of the target temperature. In-situ measurements were performed in a customized vacuum chamber to prevent oxidation, maintaining a pressure below 10^{-2} mbar during the whole experiment.

Microstructural investigations were performed by X-ray diffraction using Co-K_α radiation (XRD; Bruker D2-Phaser) and scanning electron microscopy (SEM; Zeiss LEO1525) in backscattered electron (BSE) mode. The composition was determined by an energy dispersive X-ray spectroscopy (EDS; Bruker XFlash 6|60) system.

F.3. Results and Discussion

The magnetic field H is controlled by the number of primary windings N_p , the applied current I and the mean diameter d_m [eq. F.1a], resulting in the present case in a maximum magnetic

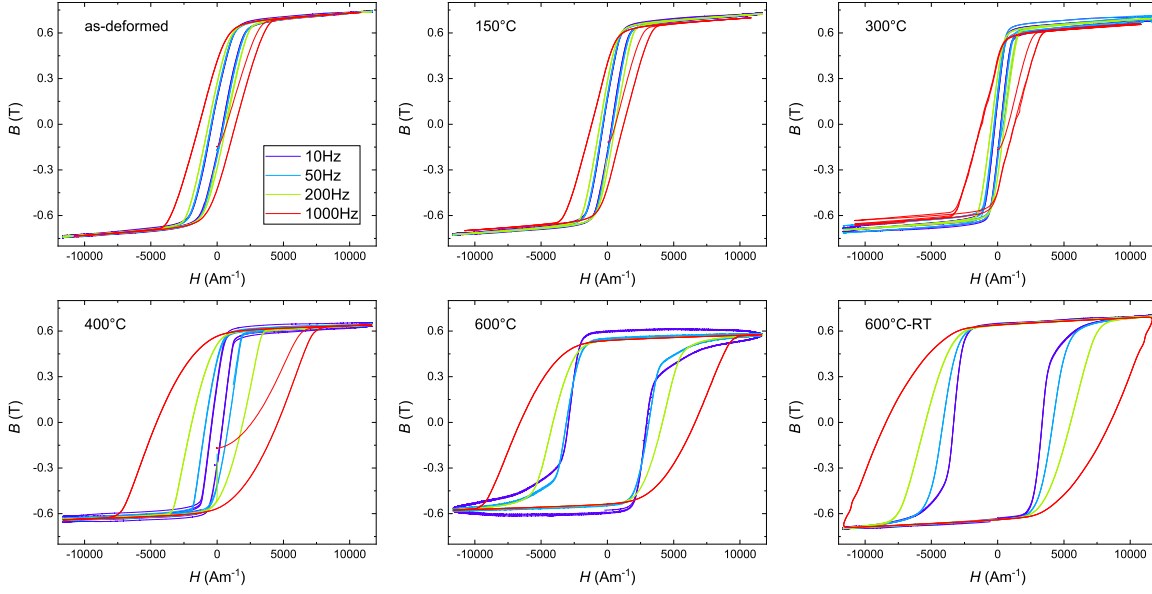


Figure F.1.: Evolution of in-situ AC-hysteresis curves according to the temperature treatment in fig. F.2. The as-deformed state is measured at RT. After in-situ temperature treatment at 150°C, 300°C, 400°C and 600°C, the specimen is measured again after cooling down to room temperature (600°C-RT). The legend applies to all diagrams.

field of 11.9 kAm^{-1} ($d_{outer}=8.76 \text{ mm}$; $d_{inner}=5.76 \text{ mm}$).

$$H = \frac{N_p \cdot I}{\pi \cdot d_m} \quad (\text{F.1a})$$

$$d_m = \frac{d_{outer} + d_{inner}}{2} \quad (\text{F.1b})$$

Eq. F.2 gives the magnetic induction B as a function of the time dependent induced voltage $U_{ind}(t)$, the number of secondary windings N_s and the cross-sectional area A of the ring-core (here: $A=0.707 \text{ mm}^2$).

$$B = \frac{\int U_{ind}(t) dt}{N_s \cdot A} \quad (\text{F.2})$$

The specimen is measured in the as-deformed state at RT, shown in fig. F.1. It can be seen, that saturation is achieved and the area of the hysteresis loop rises slightly with increasing frequency, indicating low eddy-current losses. The in-situ temperature treatment was performed according to the thermal profile shown in fig. F.2. Measurements were started after settling the target temperature for 15 min, since similarly processed Co-Cu samples showed the majority of microstructural changes happening only during a short time

F. In-situ AC-hysteresis measurements of SPD-processed $\text{Cu}_{20}(\text{Fe}_{15}\text{Co}_{85})_{80}$

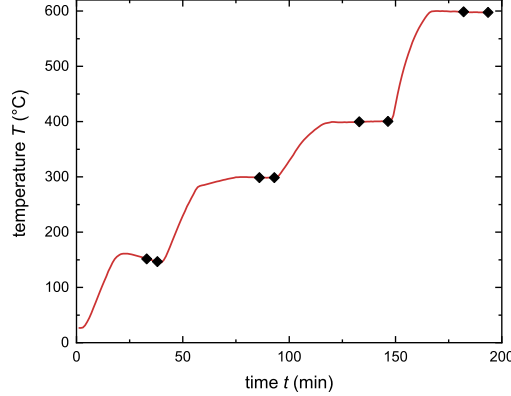


Figure F.2.: Temperature T during the in-situ experiment as a function of time t . Black diamonds mark the periods, in which hysteresis measurements are performed.

period after reaching the target temperature [7]. The time stamps of the measurements are represented by the black diamonds in fig. F.2. Hysteresis are measured at 150°C, 300°C, 400°C and 600°C. For the 150°C measurement, the temperature exceeded 160°C for a short period of time, but it was shown that the microstructure does not change in this temperature range since only relief of internal stresses takes place to a small extend [8]. The hysteresis exhibits similar shapes up to 300°C, but at 400°C the frequency behavior changes significantly, which is clearly visible in the 1000 Hz measurement. The area of the 1000 Hz hysteresis increases again in the 600°C-state. The measurement of the in-situ treated specimen is repeated after cooling down to RT (fig. F.1; 600°C-RT). For the 600°C-RT state saturation is not achieved in the 1000 Hz measurement. This means, the measured hysteresis represents a minor loop and the coercivity cannot be evaluated for this frequency. Lower frequencies reveal a larger area of the hysteresis loop with respect to the 600°C-state, arising most likely from the temperature dependence of the magnetocrystalline anisotropy according to Brukhatov-Kirensky [9].

In the following, a quantitative analysis on the evolution of the coercivity is carried out. Fig. F.3 shows the measured coercivities as a function of frequency. To disentangle the (static) intrinsic magnetic properties from the dynamic losses, [eq. F.3] is fitted to the data[10–12].

$$H_C(f) = H_C(0) + b \cdot \sqrt{f} + c \cdot f \quad (\text{F.3})$$

In [eq. F.3], the dynamic loss is separated into anomalous-loss b , caused by domain wall

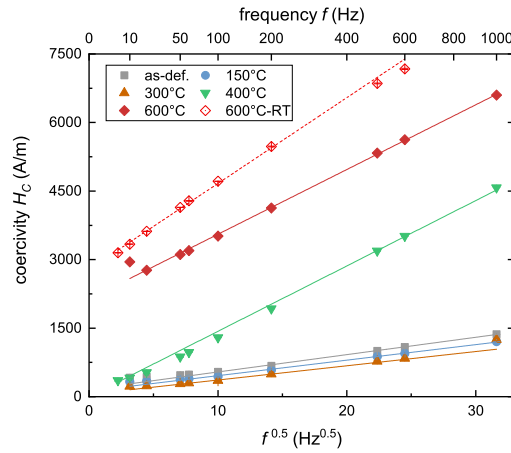


Figure F.3.: Coercivity plotted versus the square-root of frequency as recorded during temperature treatment. The lines represent the fits to [eq. F.3], taking only anomalous dynamic losses into account.

motion, and eddy current loss c , which is mainly controlled by the conductivity[13]. Since the conductivity of SPD-processed materials is significantly lowered with respect to coarse-grained materials[14], we assume the dynamic losses being mainly controlled by anomalous losses and therefore neglect the third term in [eq. F.3]. In fig. F.3, the measured coercivities are plotted versus the square-root of frequency, showing a linear scaling with \sqrt{f} , confirming the aforementioned statement. The results from linearly fitting the data are shown in fig. F.4. Diminishing static coercivity, as well as anomalous loss, can be identified between the as-deformed, 150°C- and 300°C-annealed state. For SPD-processed Cu-Co and Cu-Fe-Co, a diminishing defect density was reported in this temperature window, but no apparent changes in the grain size have been determined [4, 8]. The decreasing coercivity between RT and 400°C might therefore originate from a decrease in the magnetoelastic anisotropy constant[15] $K_{el} \propto \sigma \cdot \lambda$, with the residual stress σ and the magnetostriction λ . It should be stated, that the coercivity is further lowered by the temperature dependence of the magnetocrystalline anisotropy, as already mentioned [9]. A huge jump in $H_C(0)$ can be noticed at 600°C, indicating a large microstructural variation, such as grain growth. Large microstructural variations have been determined in similar materials at this temperature [4, 8]. A further increase in coercivity is visible for the 600°C-RT state, which is again traced back to temperature dependence.

The anomalous loss parameter b is closely related to the microstructure, and takes into account the energy needed for domain wall motion, which can be increased due to pinning at

F. In-situ AC-hysteresis measurements of SPD-processed $\text{Cu}_{20}(\text{Fe}_{15}\text{Co}_{85})_{80}$

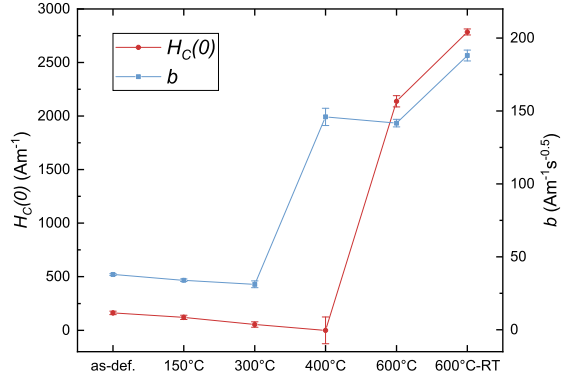


Figure F.4.: Static coercivity $H_C(0)$ and anomalous loss parameter b , determined according to [eq. F.3].

lattice defects or grain / phase boundaries. The increase in b at 400°C, therefore indicates the formation of pinning centres, rushing ahead the demixing of the microstructure at 600°C. For the 600°C-state, the anomalous loss parameter stays rather constant.

The microstructure of the in-situ heat-treated sample is investigated by SEM and XRD and compared to the initial (as-deformed) state. For this purpose a second sample is fabricated, representing the as-deformed state. Fig F.5 shows SEM images of both samples. The as-deformed state shows a highly homogeneous, nanocrystalline microstructure. In the 600°C-RT state, a significantly larger grain size in the ultra-fine grained regime is visible. Furthermore, phase contrast indicates a chemical inhomogeneity, showing demixing tendencies. Bright areas indicate high Z and therefore Cu-rich regions, whereas dark-grey or black areas point at the presence of low Z Fe-Co-rich alloy intermetallic phases. EDS-measurements at 20 different spots reveal the composition of the in-situ treated sample to $\text{Cu}_{23}(\text{Fe}_{12}\text{Co}_{88})_{77}$ (wt.%; ± 1 wt.%).

In fig. F.6, the XRD pattern of the in-situ treated sample is shown in comparison to the as-deformed state. In the as-deformed state, only one fcc-pattern is visible, revealing the single-phase crystallographic structure, whereas in the 600°C-RT state, three different patterns evolve: the fcc-Cu pattern coincides with the theoretical values, indicating the presence of pure Cu. In contrast, the fcc-Co, as well as the bcc-Fe pattern, show deviations with respect to the theoretical values, suggesting the presence of γ -(Fe,Co) and α -(Fe,Co), in line with the SEM investigations above.

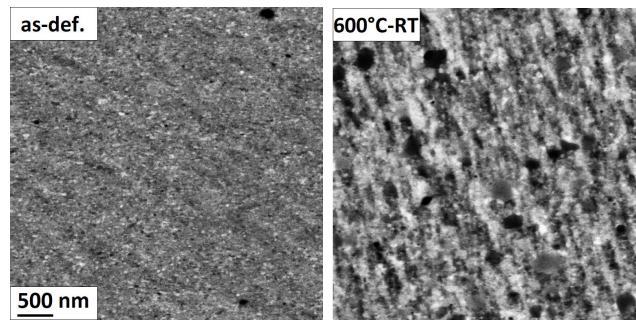


Figure F.5.: SEM-BSE images of a second specimen in as-deformed state and the sample after in-situ heat-treatment (600°C-RT) in tangential sample direction. The scale bar applies to both images.

F.4. Conclusion

In-situ AC-hysteresis measurements of SPD-processed $\text{Cu}_{20}(\text{Fe}_{15}\text{Co}_{85})_{80}$ reveal a persisting soft magnetic behavior up to 400°C. The amount of eddy current losses is low by comparison, owing to the high resistivity of SPD-processed materials. At 400°C, pinning centres start to form, hindering domain wall motion and causing an increase in dynamic loss. At 600°C, the microstructure has changed from the initial single-phase supersaturated solid solution into a multi phase microstructure according to the thermodynamical equilibrium. The formation of pinning centres rushes ahead this phase change. The results demonstrate the capability of magnetic measurements capturing smallest microstructural changes before they become evident with other techniques.

Acknowledgments

This project has received funding from the European Research Council (ERC) under the European Union’s Horizon 2020 research and innovation programme (Grant No. 757333). The authors thank R. Neubauer, M. Reiter and M. Kasalo for preparing the sample and the respective holder for in-situ experiment.

Data Availability Statement

The data that support the findings of this study are available from the corresponding author upon reasonable request.

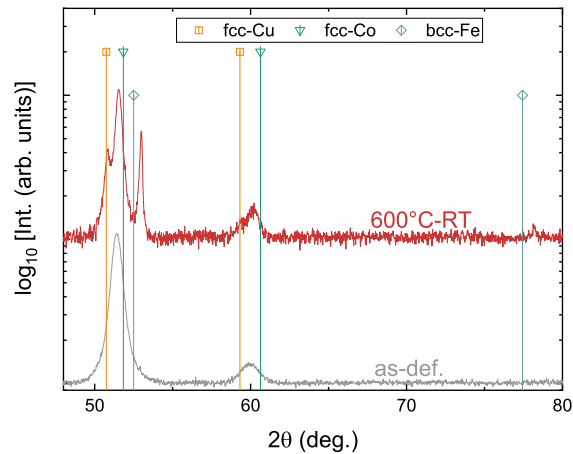


Figure F.6.: XRD pattern of the sample after in-situ heat treatment (600°C-RT) in comparison with a second specimen in as-deformed state, measured with Co- K_{α} radiation.

F.5. References

- [1] R.Z. Valiev, R.K. Islamgaliev, and I.V. Alexandrov. “Bulk nanostructured materials from severe plastic deformation”. In: *Prog. Mater. Sci.* 45.2 (2000), pp. 103–189. DOI: 10.1016/S0079-6425(99)00007-9.
- [2] K.S. Kormout, R. Pippan, and A. Bachmaier. “Deformation-induced supersaturation in immiscible material systems during high-pressure torsion”. In: *Adv. Eng. Mater.* 19.4 (2017), p. 1600675. DOI: 10.1002/adem.201600675.
- [3] M. Stückler et al. “Magnetic Binary Supersaturated Solid Solutions Processed by Severe Plastic Deformation”. In: *Nanomaterials* 9.1 (2018), p. 6. DOI: 10.3390/nano9010006.
- [4] M. Stückler et al. “On the magnetic nanostructure of a Co-Cu alloy processed by high-pressure torsion”. In: *J. Sci. Adv. Mater. Dev.* (2020). in press. DOI: 10.1016/j.jsamd.2020.09.013.
- [5] C. Kuhrt and L. Schultz. “Formation and magnetic properties of nanocrystalline mechanically alloyed Fe-Co”. In: *J. Appl. Phys.* 71.4 (1992), pp. 1896–1900. DOI: 10.1063/1.351177.
- [6] R.S. Turtelli et al. “Hysteresis and Loss Measurements on the Plastically Deformed Fe-(3 wt%) Si Under Sinusoidal and Triangular External Field”. In: *IEEE Trans. Magn.* 52.5 (2016), pp. 1–7. DOI: 10.1109/TMAG.2016.2530683.
- [7] S. Wurster et al. “Microstructural Changes Influencing the Magnetoresistive Behavior of Bulk Nanocrystalline Materials”. In: *Appl. Sci.* 10.15 (2020), p. 5094. DOI: 10.3390/app10155094.
- [8] M. Stückler et al. “Formation of solid solutions of Cu-Fe-Co by severe plastic deformation”. In: (2020).

- [9] N.L. Brukhatov and L.V. Kirensky. “The anisotropy of the magnetic energy in single crystals of Nickel as a function of temperature”. In: *Phys. Z. Sowjetunion* 12.5 (1937), p. 601.
- [10] G. Bertotti, F. Fiorillo, and G.P. Soardo. “The prediction of power losses in soft magnetic materials”. In: *J. Phys. Colloq.* 49.C8 (1988), pp. C8–1915. DOI: 10.1051/jphyscol:19888867.
- [11] F. Fiorillo. *Measurement and characterization of magnetic materials*. North-Holland, 2004.
- [12] R. Hilzinger and W. Rodewald. *Magnetic materials: fundamentals, products, properties, applications*. Vacuumschmelze, 2013.
- [13] F. Fiorillo et al. *Soft Magnetic Materials*. Webster, J.G., 2016. DOI: 10.1002/047134608X.W4504.pub2.
- [14] J.M. Cubero-Sesin, M. Arita, and Z. Horita. “High Strength and Electrical Conductivity of Al-Fe Alloys Produced by Synergistic Combination of High-Pressure Torsion and Aging”. In: *Adv. Eng. Mater.* 17.12 (2015), pp. 1792–1803. DOI: 10.1002/adem.201500103.
- [15] T.D. Shen, R.B. Schwarz, and J.D. Thompson. “Soft magnetism in mechanically alloyed nanocrystalline materials”. In: *Phys. Rev. B* 72.1 (2005), p. 014431. DOI: 10.1103/PhysRevB.72.014431.